CHEMICAL ENGINEERING SCIENCE
GENIE CHIMIQUE

VOL. 12 1960 No. 1

A generalized method for estimating heats of vaporization

M. V. KUNTE and L. K. DORAISWAMY

National Chemical Laboratory, Poona, India

(*Received* 10 *May* 1959)

Abstract—Starting from CLAPEYRON's vapour pressure equation, separate generalized correlations are developed for the gas and liquid phase contributions appearing in this equation. The final equation obtained by combining these correlations is:

$$\frac{L}{T_c} = \frac{4{\cdot}58 \log p_r}{\int_1^{T_r} (1/zT_r^2)\, dT_r} = \frac{0{\cdot}0244\,(p_r - 1)}{\int_1^{T_r} (\omega/T_r)\, dT_r}$$

A rigorous graphical solution of this equation is presented which enables estimations of the heat of vaporization of a substance from a knowledge of its critical temperature, critical pressure and vapour pressure data. The correlation has been tested for a variety of substances up to the critical point and found to be very accurate, particularly for organic compounds and elementary (or simple) molecules for which the average error in the use of this correlation is less than 2 per cent.

Résumé—Partant de l'équation de CLAPEYRON, les auteurs développent et généralisent des relations individuelles relatives à la contribution des phases gaz et liquide que cette équation met en jeu. L'équation finale obtenue à partir de ces relations est:

$$\frac{L}{T_c} = \frac{4{,}58 \log p_r}{\int_1^{T_r} (1/zT_r^2)\, dT_r} = \frac{0{,}0244\,(p_r - 1)}{\int_1^{T_r} (\omega/T_r)\, dT_r}$$

Une solution graphique rigoureuse de cette équation permet d'estimer la chaleur de vaporisation d'une substance à partir de sa température critique, de sa pression critique et de sa pression de vapeur.

La relation a été vérifiée pour plusieurs substances au dessus du point critique, et elle s'est révélée très précise, en particulier pour les corps organiques et les molécules simples, pour lesquels l'erreur moyenne est inférieure à 2 pour cent.

Zusammenfassung—Ausgehend von der Dampfdruckgleichung nach *Clapeyron* werden getrennte verallgemeinerte Beziehungen für die Anteile der Gas- und Flüssigkeitsphase in dieser Gleichung entwickelt. Diese Beziehungen werden zu folgender Schlussgleichung zusammengesetzt:

$$\frac{L}{T_c} = \frac{4{,}58 \log p_r}{\int_1^{T_r} (1/zT_r^2)\, dT_r} = \frac{0{,}0244\,(p_r - 1)}{\int_1^{T_r} (\omega/T_r)\, dT_r}$$

Eine genaue graphische Lösung dieser Gleichung wird mitgeteilt, welche die Abschätzung der Verdampfungswärme einer Substanz aus der Kenntnis ihrer kritischen Temperatur, ihres

kritischen Druckes und der Dampfdruckdaten gestattet. Die Beziehung wurde an zahlreichen Substanzen bis zum kritischen Punkt geprüft und für sehr genau befunden, insbesondere für organische Verbindungen und elementare (oder einfache) Moleküle, für welche der mittlere Fehler kleiner als 2 Prozent ist.

SURVEY AND OBJECTIVE

MANY empirical methods have been proposed in the past for the estimation of latent heats of vaporization at different temperatures and pressures. The familiar TROUTON's rule and its earlier modifications [1, 2] are of limited use in process calculations; the HILDEBRAND modification [3] of the TROUTON rule has merited some attention [4, 5] but has not yielded any generalized relationship. A simple equation was proposed by KISTIAKOWSKY [6], but it is applicable to non-polar liquids at their normal boiling points only. Another noteworthy relationship is the Antoine equation of O'HARA and FAHIEN [7]; this equation involves two constants and, in addition requires vapour pressure and critical point data for its use.

The most useful, if not the most accurate, method available is perhaps that of WATSON [8, 9]. Based on the observation that, when the TROUTON ratio is plotted against reduced temperature, curves of the same shape are obtained for all substances, whether polar or non-polar, WATSON obtained the general empirical equation,

$$\frac{L}{L'} = \left(\frac{1 - T_r}{1 - T_r'}\right)^{0.38} \tag{1}$$

which can be used to obtain the heat of vaporization at any given temperature and pressure provided the value at any one temperature and pressure (usually the normal boiling point) is known together with that of critical temperature. This method has the advantage that vapour pressure data are not required, but large errors may be encountered in the vicinity of the critical point.

The well known method of reference substance plots proposed by OTHMER [10] was later improved by GORDON [11] who replaced the equal-temperature basis of these plots by the more general equal-reduced temperature basis. Recently CHIEN CHI LI and CANJAR [12], utilizing the observation of LYDERSEN *et al.* [13] that the difference between gas and liquid phase compressibilities is a unique function of reduced pressure only, proposed a reference substance method based on equal reduced pressures and reported good agreement between calculated and observed heats of vaporization.

A generalized procedure, employing reduced co-ordinates, was developed by MEISSNER [2, 14]. On the assumption that the relationship,

$$\log p = -\frac{A}{T} + B \tag{2}$$

is rigidly valid up to the critical point, MEISSNER derived the equation,

$$\log p_r = \frac{L}{RT_c(z - z_l)}\left(1 - \frac{1}{T_r}\right) \tag{3}$$

As pointed out by WATSON [9], the use of equation (3) becomes somewhat unsound at low values of T_r.

The object of the present paper is to offer a rigorous, alternative procedure using generalized co-ordinates for an accurate estimation of heats of vaporization up to the critical point, and to present graphical solutions of the equations developed.

THEORETICAL DEVELOPMENT

The Clapeyron equation in its original form is written as:

$$L = (v - v_l)\, T \frac{dp}{dT} \tag{4}$$

or

$$L = vT\frac{dp}{dT} - v_l T \frac{dp}{dT} \tag{5}$$

The latent heat may therefore be visualized as consisting of two contributions, one from the gas phase and the other from the liquid phase. Denoting these contributions by L_1 and L_2, respectively, we obtain

$$L = L_1 - L_2 \tag{6}$$

L_1 and L_2 may now be separately evaluated and combined to obtain L.

Evaluation of L_1

From the following two equations,

$$L_1 = vT\frac{dp}{dT} \tag{7}$$

and

$$pv = z\,RT \tag{8}$$

equation (9) below may be obtained by substituting reduced temperature and pressure (T_r and p_r) for T and p and separating the variables:

$$\frac{L_1}{RT_c\,zT_r^2}\,dT_r = \frac{1}{p_r}\,dp \tag{9}$$

Equation (9) can be integrated if the limits of integration are fixed. This is easily done if it is remembered that the latent heat of vaporization of a liquid is zero at the critical point; the limits may therefore be written as $p_r = 1$, $p_r = p_r$ and $T_r = 1$, $T_r = T_r$. Thus, assuming as a first approximation, an average constant value of L_1 over a given range of T_r values,

$$\frac{L_1}{T_c} = \frac{2{\cdot}303\;R\log p_r}{\int_1^{T_r} 1/zT_r^2\,dT_r} \tag{10}$$

When the term $\int_1^{T_r}(dT_r/zT_r^2)$ is integrated on the further assumption that z is constant at an average value over a particular range of temperatures and pressures, we obtain

$$\frac{L_1}{T_c} = \frac{2{\cdot}303\,zR\log p_r}{(1 - 1/T_r)} \tag{11}$$

which is similar to the MEISSNER equation for L. But it is evident from the assumptions made that equation (11) is unsound. Therefore, in order to arrive at fairly accurate values of L_1, it is necessary to evaluate the term $\int_1^{T_r} dT_r/zT_r^2$ by graphical integration. This procedure is elaborated in a later section.

Evaluation of L_2

The liquid phase contribution is given by

$$L_2 = v_l\,T\frac{dp}{dT} \tag{12}$$

If v_l can be expressed in terms of T_r and p_r, equation (12) can be generalized. For this purpose, WATSON's postulation of the liquid expansion factor [9], defined by equation (13), may be used:

$$\omega = \frac{T_c}{p_c\,M}\,\frac{1}{v_l} \tag{13}$$

WATSON constructed a chart for ω as a function of T_r and p_r using the experimental values of *iso*-pentane, normal pentane and propane. BREBACH and THODOS [15] have recently constructed another chart based on the experimental values of nitrogen. The two charts show deviations of the order of 10–15 per cent. This deviation is explained by the fact that the values of the critical ratio,

$$z_c = \frac{p_c\,v_c}{RT_c} \tag{14}$$

are different for the liquids used in the construction of these charts; the average value of the three liquids employed by WATSON is 0·271 and that of nitrogen is 0·291. It has been suggested by BREBACH and THODOS [15], LYDERSEN *et al.* [13] and others [16, 17] that in addition to T_r and p_r, z_c should also be employed as a correlating parameter. Consequently, neither of the two available ω-charts can be considered as truly general. This may now be examined with respect to the present study. The errors introduced by neglecting variations in z_c may be obviated by the observation that the product $(\omega\,v_l)$ is constant for a given liquid:

$$\omega\,v_l = k \tag{15}$$

This may be combined with the further observation that if v_l at a reference state is known then v_l at any other state may be calculated with accuracy by the equation,

$$v_l = \frac{(v_l\,\omega)_{ref}}{\omega} \tag{16}$$

using a chart of ω as a function of T_r and p_r prepared for any liquid. This is done by first

calculating $(\omega v_l)_{ref}$ by use of the ω-chart and then obtaining v_l by reading the value of ω at any desired temperature and pressure from the chart. In this way the errors resulting in the direct use of any available ω-chart for liquids having different values of z_c are reduced to less than 5 per cent.

As mentioned above, the ω of equation (16) is dependent on the value at a reference state being known. The choice of the critical point as the reference state generalizes this equation. At the critical point, the value of ω is very nearly constant at 0·044; substitution of this value in equation (15) gives

$$k = 0{\cdot}044\, v_c \tag{17}$$

Combination of equations (14), (15) and (17) and rearrangement results in equation (18):

$$v_l = 0{\cdot}044\, z_c\, R \left(\frac{T_c}{\omega\, p_c}\right) \tag{18}$$

The actual fixation of the value of z_c to be employed in equation (18) can be done by taking the best average for a variety of liquids. This value has been found [18] to be 0·276 which is very close to the average value for the liquids employed by WATSON. Substituting $z_c = 0{\cdot}276$ in equation (18), combining this with equation (12) and placing the limits of integration as before, one obtains by use of generalized co-ordinates:

$$\frac{1}{T_c}\int_1^{T_r} \frac{L_2\,\omega}{T_r}\, dT_r = 0{\cdot}0122\, R\,(p_r - 1) \tag{19}$$

The term $\int_1^{T_r} (L_2\,\omega/T_r)\, d\,T_r$ may now be integrated using the ω-chart by assuming L_2 to be constant as a first approximation. For values of $T_r < 0{\cdot}6$ and for low pressures, ω has been expressed as a straight line function of T_r:

$$\omega = 0{\cdot}1745 - 0{\cdot}0838\, T_r \tag{20}$$

Substituting this in equation (19) and integrating,

$$\frac{L_2}{T_c} = \frac{0{\cdot}0244\,(p_r - 1)}{0{\cdot}403 \log T_r - 0{\cdot}0838\,(T_r - 1)} \tag{21}$$

For higher values of T_r, equation (20) is no longer applicable and the term $\int_1^{T_r} (L_2\,\omega/T_r)\, dT_r$ should be graphically integrated as discussed in the following section.

GRAPHICAL SOLUTION

The generalized compressibility factor chart constructed by HOUGEN and WATSON [19] may be used for the graphical integration of $\int_1^{T_r} (1/zT_r^2)\, dT_r$ of equation (10). For a series of assumed T_r values up to unity, graphical integrations were performed for p_r values from 0·03 to 0·975. For $p_r < 0{\cdot}03$, the values of z being approximately between 0·98 and 1·0, z was assigned an average constant value for a given p_r, and L_1/T_c was calculated directly. The chart for L_1/T_c, showing only the main values of p_r, is presented in Fig. 1. It may be pointed out that graphical integrations performed as above would actually give a mean value $\overline{L_1}$ and not L_1, $\overline{L_1}$ being defined by

$$\overline{L_1} = \int \frac{L_1\, dT_r}{zT_r^2} \Big/ \int \frac{dT_r}{zT_r^2} \tag{22}$$

A few integrations over different temperature ranges at chosen constant values of p_r have shown that L_1 is practically independent of T_r, so that $\overline{L_1} \sim L_1$. Thus Fig. 1 may be considered quite accurate.

For evaluating L_2/T_c, the analytical solution of equation (19) presented in equation (21) was combined with graphical integration of the term $\int_1^{T_r} (L_2\,\omega/T_r)\, dT_r$ using WATSON's chart in order to obtain values of L_2/T_c up to the critical point; these are presented in Fig. 2. It has been observed, as in the case of L_1, that the mean values, $\overline{L_2}$, are equal to L_2. Fig. 2 shows the values of L_2/T_c over the entire range of interest; the nature of the curves suggests that two different graphs are required for accurate reading of the values, but in the figure these are combined by a break of scale and only the main parameters

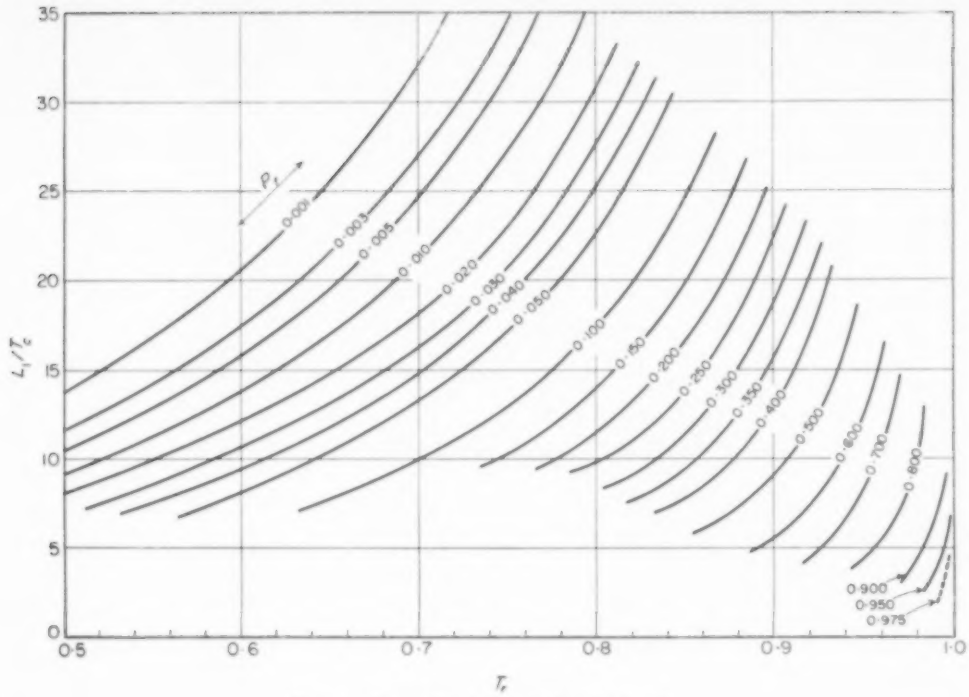

FIG. 1. Generalized correlation for L_1/T_c.

are drawn. For values of $T_r > 0{\cdot}7$ the constribution due to the liquid phase is seen to be sizeable, while for values less than 0·7 this contribution is very small.

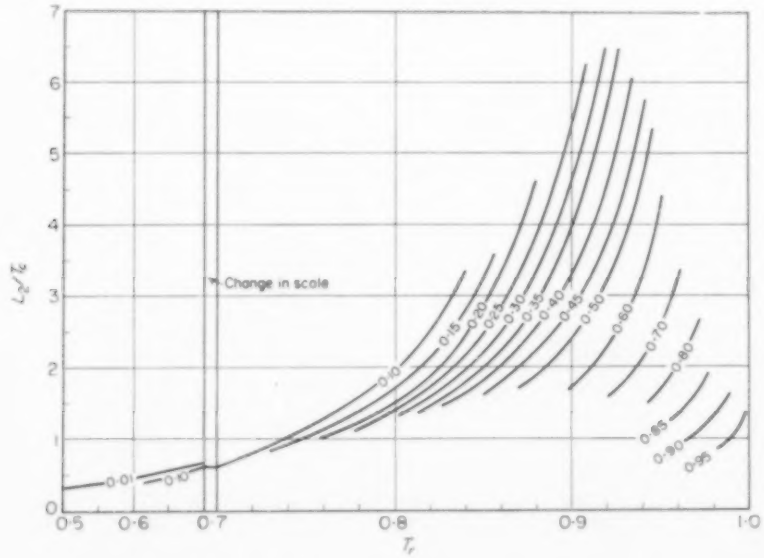

FIG. 2. Generalized correlation for L_2/T_c.

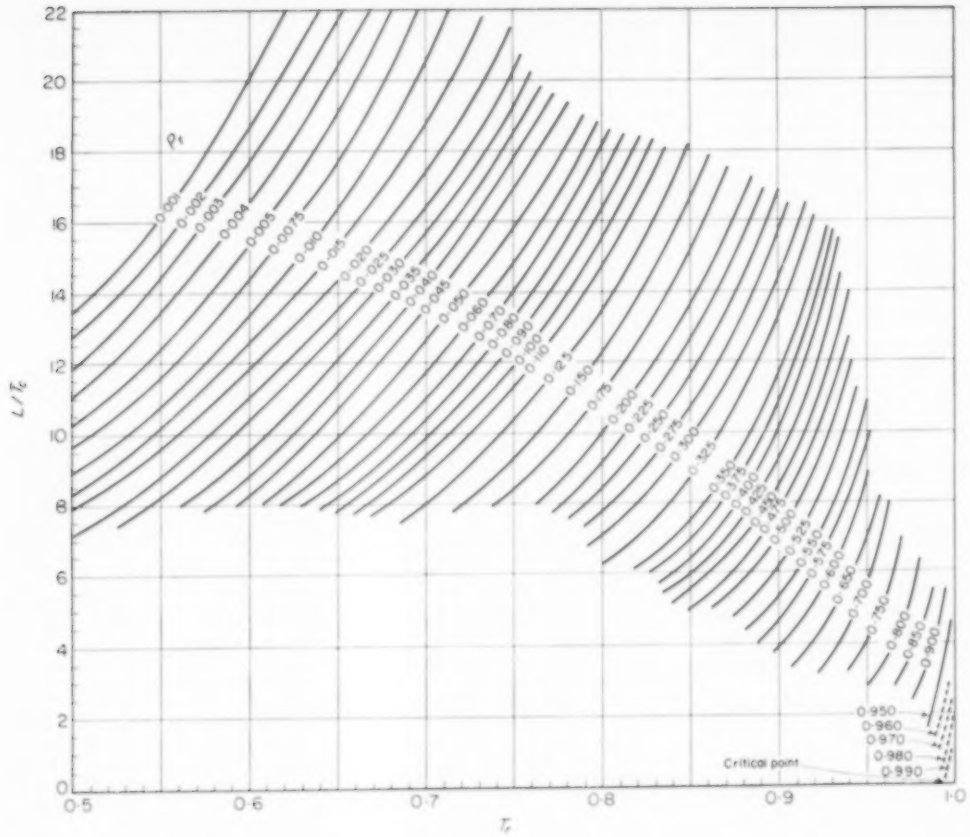

FIG. 3. Generalized correlation for heat of vaporization T °K L cal/g mole.

The final chart for estimating L/T_c is presented in Fig. 3. This was constructed by enlarging various sections of Figs. 2 and 3 and combining the values read from them according to equation (6). Curves have been drawn for a large number of p_r values to enable accurate interpolation. While the limits of the parameters in Fig. 1 have been arbitrarily fixed, those in Figs. 2 and 3 have been fixed on the basis of the expansion factor chart and available liquid compressibility data.

Accuracy of correlation

The correlation developed in this paper has been subjected to an exhaustive test. Values read from Fig. 3 were compared with experimental results for a variety of substances which included hydrocarbons, organic acids, bases, esters, ethers,

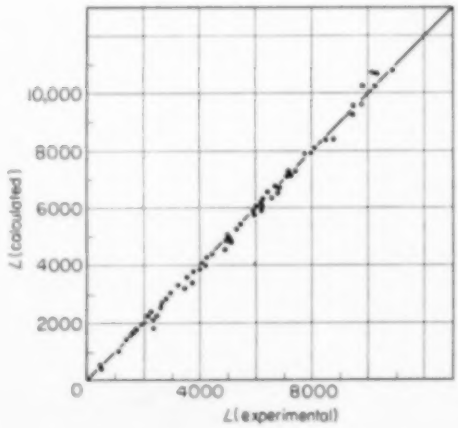

FIG. 4. Comparison of experimental and calculated heats of vaporization

P_r 0·009–0·990 T_r 0·500–0·990

halides, elementary molecules and a few inorganic compounds. A total of about 100 comparisons (up to the critical point) were made and the correlation was found to be good to within about 2 per cent on an average. Maximum deviations were encountered in the case of a few inorganic substances which gave errors of the order of 10–15 per cent. In these cases the other available correlations gave errors of a higher magnitude. Fig. 4 shows a plot of calculated and experimental results; to avoid heavy clustering of points, only about sixty sets of data are plotted covering the entire range up to the critical point.

On the basis of a survey of all available methods for estimating heats of vaporization, it is concluded that where vapour pressure data are not available WATSON's correlation [9] appears to be the best known empirical procedure, but where vapour pressure data are available the rigorous development presented in this paper should give very accurate results, particularly for organic compounds and elementary (or simple) molecules.

NOTATION

A, B = constants of vapour pressure equation
k = constant of equation (15)
L = heat of vaporization cals/g mole
L' = heat of vaporization at a reference condition of temperature
$\bar{L}$ = mean value of L defined by equation (22)
M = molecular weight
p = vapour pressure
R = gas constant
T = absolute temperature °K
T' = reference temperature
z = compressibility factor
v = molar volume
ω = liquid expansion factor

Subscripts

1 = gas phase contribution to heat of vaporization
2 = liquid phase contribution to heat of vaporization
c = critical state
l = liquid state
r = reduced state

REFERENCES

[1] BINGHAM J. *Amer. Chem. Soc.* 1906 **28** 723.
[2] MEISSNER H. P. and PADDISON O. H., Jr. *Industr. Engng. Chem.* 1941 **33** 1189.
[3] HILDEBRAND J. H. *J. Amer. Chem. Soc.* 1915 **37** 970.
[4] LEWIS W. K. and WEBER H. C. *Industr. Engng. Chem.* 1922 **14** 485.
[5] MCADAMS W. H. and MORRELL J. C. *Industr. Engng. Chem.* 1924 **16** 375.
[6] KISTIAKOWSKY *Z. phys. Chem.* 1923 **107** 65.
[7] O'HARA J. B. and FAHIEN R. W. *Industr. Engng. Chem.* 1951 **43** 2924.
[8] WATSON K. M. *Industr. Engng. Chem.* 1931 **23** 360.
[9] WATSON K. M. *Industr. Engng. Chem.* 1943 **35** 398.
[10] OTHMER D. F. *Industr. Engng. Chem.* 1940 **32** 841.
[11] GORDON D. H., Ph.D. Thesis, University of Wisconsin 1942.
[12] CHIEN CHI LI and CANJAR L. N. *Petrol. Refin.* 1959 **83** 233.
[13] LYDERSEN A. L., GREENKORN R. A. and HOUGEN O. A. Report No. 4 Engineering Experimental Station, Wisconsin University, October, 1955.
[14] MEISSNER H. P. *Industr. Engng. Chem.* 1941 **33** 1440.
[15] BREBACH W. J. and THODOS G. *Industr. Engng. Chem.* (Chem. Engng. Data Series) 1958 **3** 338.
[16] BROCK J. R. and BIRD R. B. *Amer. Inst. Chem. Engrs. J.* 1955 **1** 174.
[17] HOBSON M. and WEBER J. H. *Amer. Inst. Chem. Engrs. J.* 1956 **2** 355.
[18] KUNTE M. V. and DORAISWAMY L. K. *Chem. Process Engng.* 1958 **39** 157.
[19] HOUGEN O. A. and WATSON K. M. *Chemical Process Principles Charts.* p. 103. John Wiley, New York 1947.

Chemical Engineering Science, 1960, Vol. 12, pp. 8 to 19. Pergamon Press Ltd., London. Printed in Great Britain

An investigation of the viscous and inertial coefficients for the flow of gases through porous sintered metals with high pressure gradients

D. B. Greenberg* and E. Weger

Department of Chemical Engineering, The Johns Hopkins University, Baltimore 18, Maryland

(*Received* 12 *May* 1959)

Abstract—This paper deals with the results of an investigation of the steady-state flow of gas through porous sintered metals under high pressure gradients. The purpose of the study was to determine the behaviour of the viscous and inertial flow coefficients in such media as a function of pressure and temperature. Pore size distributions of the various cores tested were obtained by means of mercury intrusion measurements. Mean cross-section diameters which were derived from this data correlated well with experimentally obtained permeabilities. The porosities of all six of the cores which were used were within the 30–40 per cent porosity range.

It is found that the permeability (the reciprocal of the viscous flow coefficient), while not a function of pressure, decreases significantly as the temperature of a sintered porous medium is increased. This is attributed to small changes in the surface structure of the particles which constitute the medium. The inertial coefficient for any given core is found to be a constant within the pressure and temperature ranges which were covered by the present experiments.

Résumé—Ce mémoire traite des résultats d'une étude sur l'écoulement permanent d'un gaz à travers les pores de métaux frittés sous de hauts gradients de pression. L'objet de cette étude était de déterminer le comportement des coefficients de viscosité et d'inertie de l'écoulement dans ce milieu en fonction de la pression et de la température. Les distributions de la dimension des pores des différents corps examinés étaient obtenus au moyen de mesures par injection de mercure. Les diamètres moyens des sections transversales qui sont obtenus de ces données se relient bien avec les perméabilités obtenues expérimentalement. Les porosités des six corps utilisés se situent dans l'intervalle de 30–40 pour cent de porosité.

Zusammenfassung—Die Arbeit beschäftigt sich mit Untersuchungsergebnissen der gleichförmigen Strömung von Gas durch poröse Sintermetalle unter hohen Druckgradienten. Zweck der Untersuchung war, das Verhalten von Viskositäts- und Trägheitskoeffizienten in derartigen Stoffn als Funktion von Druck und Temperatur zu ermitteln. Die Porengrössenvereteilungen der verschiedenen geprüften Kerne wurden durch Infiltrationsmessungen von Quecksilber ermittelt. Die so erhaltenen, mittleren Querschnittsdurchmesser stimmten gut mit den experimentell ermittelten Permeabilitäten überein. Die Porositäten aller sechs verwendeten Prüfkörper lagen innerhalb des 30 bis 40 prosent Porositätsbereiches.

Es wird festgestellt, dass die Permeabilität (reziproker Wert des Viskositätskoeffizienten), die nicht vom Druck abhängt, beträchtlich mit steigender Temperatur des porösen Sinterwerkstoffes abnimmt. Das wird den kleinen Änderungen der Oberflächenstruktur der Teilchen des Sinterkörpers zugeschrieben. Es wird gefunden, dass der Trägheitskoeffizient für jeden Prüfkörper innerhalb des Temperatur- und Druckbereiches, über den sichd ie Untersuchung erstreckte, konstant ist.

*Present Address: U.S. Naval Academy, Annapolis, Maryland.

Introduction

The need for study of the flow of fluids through porous media has become apparent in many fields of engineering and science in recent years. An understanding of this phenomenon is important in the study of ground water hydrology, soil mechanics and natural gas reservoirs of the petroleum industry. Much of the early work has been compiled by Muskat, first in 1937 [1], and again in 1949 [2], and by Hubbert [3], in 1940. Related work in absorption, extraction, distillation and filtration has also yielded important results in this field. Current interest in the flow of fluids through porous materials is centered about applications in aerodynamic boundary layer control and transpiration cooling in the area of ballistics and rocketry [4, 5].

The steady-state flow of fluids through porous media has been studied extensively from both an experimental and analytical standpoint for relatively low pressure gradients. Grunberg and Nissan [6] investigated viscous effects in gases at low flow rates. The deviation of flow in consolidated media from the characterized by a purely viscous motion has been studied by Green and Duwez [7]. Correlations for both viscous and inertial effects in unconsolidated media were presented by Brownell *et al.* [8].

The conclusion to be drawn from these papers is that most experimental results for one dimensional flow through porous materials (both consolidated and unconsolidated) may be correlated by an equation of the type

$$-\frac{dp}{dx} = \alpha\mu V + \beta\rho V^n \qquad (1)$$

where α and β are so-called "constants," and n is some number between 1 and 2. The parameter α is the inverse of the famous Darcy constant, k, [9]. The first term on the right-hand side of equation (1) represents the portion of the pressure gradient due to viscous effects, while the second term represents the contribution by inertial effects. The exact nature of the inertial contribution is not well understood. It is unlikely that true turbulence exists in a fine-grained porous material. The majority of the inertial effects are probably due to expansion and contraction of the fluid, rapidly changing direction of the flow path, etc.

The "constant" β, as well as α, is, of course, dependent on the geometry of the medium. While it is impossible to describe this geometry in its microscopic detail, except for idealized media, quantities such as porosity, specific surface and pore size distributions – as well as the structure of the component particles – can give a gross indication of the structural variation among various porous materials. The structure may change to a certain extent as the ambient conditions are varied. Thus, changes in pressure or temperature might be expected to affect the values of α and/or β. Little mention has been made in the literature of these effects.

Cornell and Katz [10] have presented correlations of data on the flow of gases through consolidated porous material using equation (1). Their results indicate that $n = 2$ for these types of materials. Under steady-state conditions the mass velocity of gas (for one dimensional flow) through a porous material must be constant. If we let $\rho V = G$, equation (1) becomes

$$-\rho\frac{dp}{dx} = \alpha\mu G + \beta G^2 \qquad (2)$$

Using the perfect gas law with a compressibility coefficient, we obtain

$$-\frac{M}{zRT}p\frac{dp}{dx} = -\frac{M}{2zRT}\frac{d(p^2)}{dx} \qquad (3)$$

Integrating and rearranging equation (3), we obtain,

$$\frac{\Delta(p^2)\,Mg}{2L(zRT)\,\mu G} = \alpha + \beta\left(\frac{G}{\mu}\right) \qquad (4)$$

which is the relationship Cornell and Katz used in analysing their data. If the quantity on the left-hand side of the equation is plotted versus G/μ for a given run, the slope will yield β, while α will be obtained from the intercept.

The Reynolds number of a flow system is defined as the ratio of inertial to viscous forces. Since the ratio of β/α represents the ratio of the inertial to the viscous coefficient, a modified

Reynolds number for porous media may be defined as

$$N_{Re} = \left(\frac{\beta}{\alpha}\right)\left(\frac{G}{\mu}\right) \tag{5}$$

By inspection, equation (4) may be rearranged to yield:

$$\frac{\Delta(p^2)\,Mg}{(\beta L)(zRT)\,G^2} = \frac{2}{(\beta/\alpha)(G/\mu)} + 2 \tag{6}$$

The left-hand member of equation (6) is a ratio of dissipative to inertial forces and, therefore, represents a friction factor. Thus, equation (6) becomes:

$$f = \frac{2}{N_{Re}} + 2 \tag{7}$$

and has been suggested by Green and Duwez [7] to be a representative friction factor correlation for porous media. The friction factor is represented by $2/N_{Re}$ in the Darcy (or laminar) region and by 2 in the inertial region.

Due to lack of knowledge of the exact fine structure of most porous media and the inadequacy of present analytical methods for describing fluid flow through such complex structures it is necessary to re-determine the validity of expressions such as equation (4) when any of the parameters are changed drastically from those under which previous experimental data was obtained.

The unrigorous nature of the derivation of the flow equations for porous media leaves open the question whether the "constants" are really constant and vary only as the structure of the medium varies; or whether they themselves are dependent to an extent on the pressure and flow rate obtaining in the medium. Recent interest in the high pressure region, both for steady-state and transient flow in porous materials, has demonstrated a need for investigations of the applicability of the relationships for flow through porous media which have been developed mainly on the basis of low pressure data. The constancy of the "constants" especially must be checked.

It was the purpose of the present study to obtain experimental evidence on this point over a pressure range up to 2000 p.s.i.

Experimental

Six porous sintered metal cores, covering a wide range of metal particle size and permeability, were selected for this investigation. These samples were chosen after a series of preliminary tests had determined the characteristics of metallic media which were necessary for obtaining reproducible and reliable data. The powder size and sintering conditions for some of the cores were selected in order to obtain the high pressure gradients which were of primary interest in the present work. The cores which were used for the reported runs and their physical characteristics are listed in Table 1.

The particles (except for the brass core) were approximately spherical in shape. Pore size distribution measurements were performed on samples cut from the cores by means of a mercury intrusion porosimeter [13]. Fig. 1

Table 1. Physical properties of porous cores

Supplier	*Core no.*	*Core material*	*Particle size range* (μ)	*Mean pore diameter* (μ) (*from pore size measurements*)	*Porosity* (22 °C) *From density measurements*	*Porosity* (22 °C) *From pore size measurements*
Frankfort Arsenal	F–B2–12	Bronze	45*	15	0·357	0·307
	F–Br4–32	Brass	40*	4 +	0·437	0·360
Kulite Tungsten Co.	K–N1–2	Nickel	7–15	3·5	0·324	0·264
	K–C–1	Copper	5–40	18	0·377	0·318
Sylvania Electric Corp.	S–N–1	Nickel	3–16	2·5 +	0·330	0·310
	S–T–1	Tungsten	1–18	1·0	0·394	0·421

*Estimate

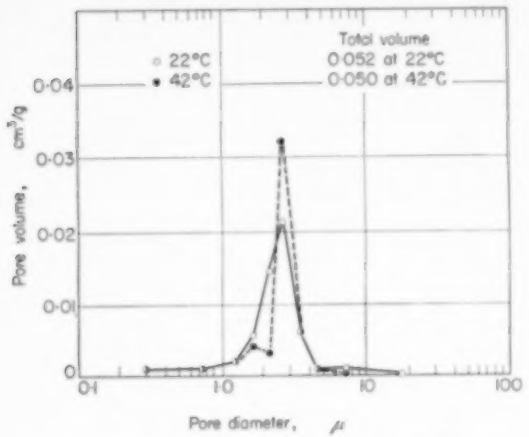

FIG. 1. Pore size distributions of the S–N–1 core.

	Total volume
○ 22 °C	0·052 at 22 °C
● 42 °C	0·050 at 42 °C

shows distributions of the S–N–1 core at two temperatures. Similar results were obtained for the other cores. The reason for measurements at two temperatures will become apparent later. The data were actually reported in terms of fraction of pore volume over a given size range. The points in Fig. 1 represent the midpoints of these ranges. Mean pore diameters were determined from these curves. The method, based upon the principle of capillary forces, yields an approximate picture of the internal structure of a porous material. However, it is important to understand the limitations of the method. In a material such as sintered metal there are many spaces or "cells" which are connected to the rest of the porous system only by passages which are of smaller average cross-section than the cells themselves. A method based upon the increase in pressure required to force a liquid, such as mercury, into smaller and smaller pores will include the volume of such cells with the pore size range which contains the diameter of the *largest* passage connecting the cell and the rest of the flow system. The results are, therefore, essentially measurements of the "constriction" diameter distributions rather than true average pore size diameter. The importance of these contributions will be touched upon further in the discussion.

The other limitation – one which is not important in the present work – is the fact that one can only measure the pore space which is connected by flow passage to the rest of the system. Completely enclosed cells will not be included. It can be seen in Table 1 that the void fractions obtained from the pore size distribution measurements are usually below the corresponding values determined from density measurements. It was determined that no appreciable structure of the cores used in the recent experiments lay outside the 200/0·1 μ limits of the measurements. The difference in densities must, therefore, be due to enclosed cell structure. An anomalous result was obtained with the S–T–1 core. At present, there is no satisfactory explanation for this case.

A potting method was developed for encasing the porous cores in steel sleeves using an epoxy resin formulation similar to those used by manufacturers of electrical components. Because of the extreme wettability of this resin, the cores (all except the S–T–1 core which was "sweated" into its sleeve) were sealed in an aluminium putty-like resin, to prevent the epoxy resin from seeping into the pore spaces of the sample.

After the samples were mounted in the sleeves, both core faces were given finish cuts on the lathe to make the ends flat and parallel. This operation tended to smear the porous metallic surface necessitating a metallographic treatment to restore the end grains as closely as possible to being representative of any cross-section within the sample.

This metallographic process included a wet sanding using 300 W and 600 W silicon carbide polishing papers followed by a final treatment on a series of alumina polishing wheels to bring out the grain boundaries, preparatory to opening the pore surfaces.

An electrylotic polishing method was used to remove the remaining smeared metal from the surface. It was found that the electrolytic technique was far superior to the more common chemical etching methods for this work. Fig. 2 is a photomicrograph ($\times$ 250) of the surface of core F–B2–12 (Bronze) after such treatment, while Fig. 3 shows the surface of Core F–Br4–32 after similar treatment. Details of the technique are reported in references [11, 12].

The experimental apparatus consisted of an hydraulic system designed to maintain a constant source of high pressure nitrogen gas for the flow studies, a gas reservoir and a suitable means for controlling and measuring pressure, temperature and gas flow rate. Fig. 4 is a flow diagram of the equipment.

The pump was a dual feed positive displacement pump, with a continuously varying stroke control to regulate the hydraulic fluid output up to a maximum of 4·9 gal/hr for each feed, at 2500 p.s.i. The hydraulic system functioned continuously during a run supplying oil to the gas reservoir at a rate slightly above that of gas withdrawal. The excess oil was bypassed back to the storage tank. This arrangement insured positive control while damping pressure surges inherent in positive displacement pumps. A solenoid-pneumatic piston type control valve metered excess fluid back to the storage tank. The solenoid was controlled by a pressure-sensitive electric contact gauge.

Adequate control over the gas flow system was obtained by a gas-loaded diaphgram valve. Fluctuations in gas flow were observed to be generally less than about 2 per cent. The sleeve containing the porous core was fixed between two end blocks which contained the connections for gas inlet and outlet and the taps for pressure measurements at both ends of the sample. A satisfactory pressure

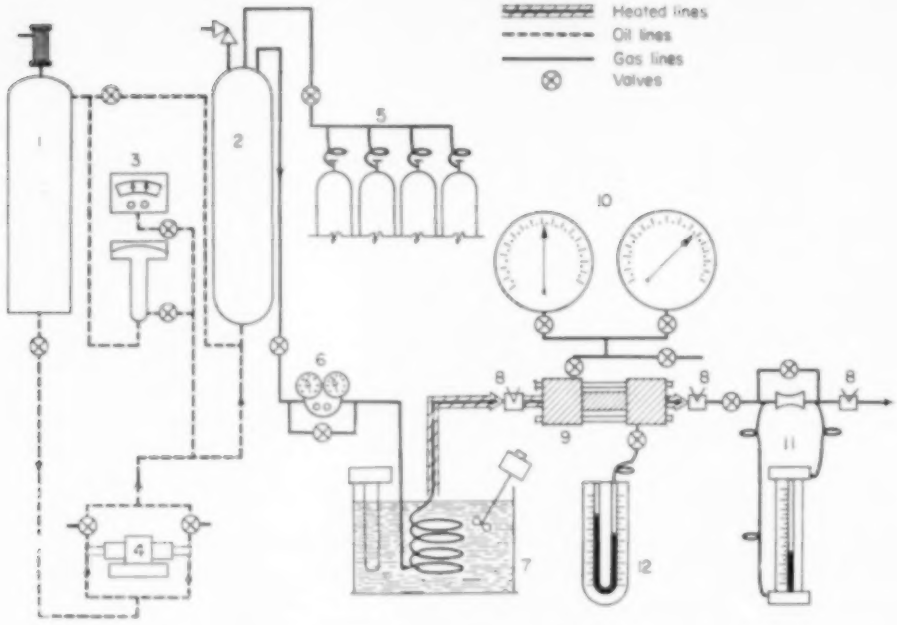

Fig. 4. Flow diagram of experimental equipment. Legend:

1 – oil reservoir	5 – gas manifold	9 – porous core assembly	≠≠≠≠ heated lines
2 – gas reservoir	6 – gas pressure control	10 – pressure gauges	———— gas lines
3 – oil pressure control	7 – temperature bath	11 – flow meter	— — — oil lines
4 – oil pump	8 – thermocouples	12 – manometer	⊗ valves

seal against 2500 p.s.i. was readily obtained by using teflon gaskets against 1/4 in. bearing surfaces and drawing the opposite blocks together against the ends of a sample with four 5/8 in. bronze marine bolts. The upstream and downstream pressure taps were located approximately 1/8 in., measured horizontally, from either end of the sample. Two Bourdon tube pressure gauges measured upstream pressures. These were accurate to 0·1 per cent of full scale deflection and frequent comparisons during operation indicated a deviation between them never exceeding 1 p.s.i. up to 1000 p.s.i. The downstream pressure was measured by a Merriam Gauge manometer.

It was found early in the test programme that it would be necessary to control the gas temperature closely, in order to obtain reproducible results. This was due to two effects. The first was an appreciable cooling effect due to the Joule–Thomson expansion in the porous cores. Temperature gradients of the order of 5 °C/in. were found for some samples at high pressures. The second effect was an appreciable change of permeability with changes of temperature of the porous core. It was felt that this second effect could also be adequately controlled by controlling the gas temperature. The discovery of the second effect led to a programme directed toward a systematic investigation of the temperature dependence of permeability.

Temperature control and regulation was maintained by means of a water bath and flexible heating tape. A pair of 200 w flexible heating tapes, one wrapped around the line from the bath to the porous core assembly and the other around the core itself, were employed to facilitate temperature control in the test device. The current in each tape was adjusted individually until the inlet and outlet temperatures agreed within 2 °C. Temperatures were measured by two iron–constantan thermocouples placed about 3 in. upstream and downstream from the ends of the sample.

Gas flow rate measurements were made with a dual element orifice meter. Accuracy obtained with this meter was better than 0·5 per cent of the full scale reading, since the orifice was designed to give a linear flow rate–pressure drop relationship. Calibrations were made at infrequent intervals with a wet test meter.

All high pressure equipment was housed behind a safety barricade of steel boiler plate. All valves, measuring instruments and controls were mounted on the outside so as to facilitate operation from the front of the shield. The high pressure gas reservoir was fed from a four-

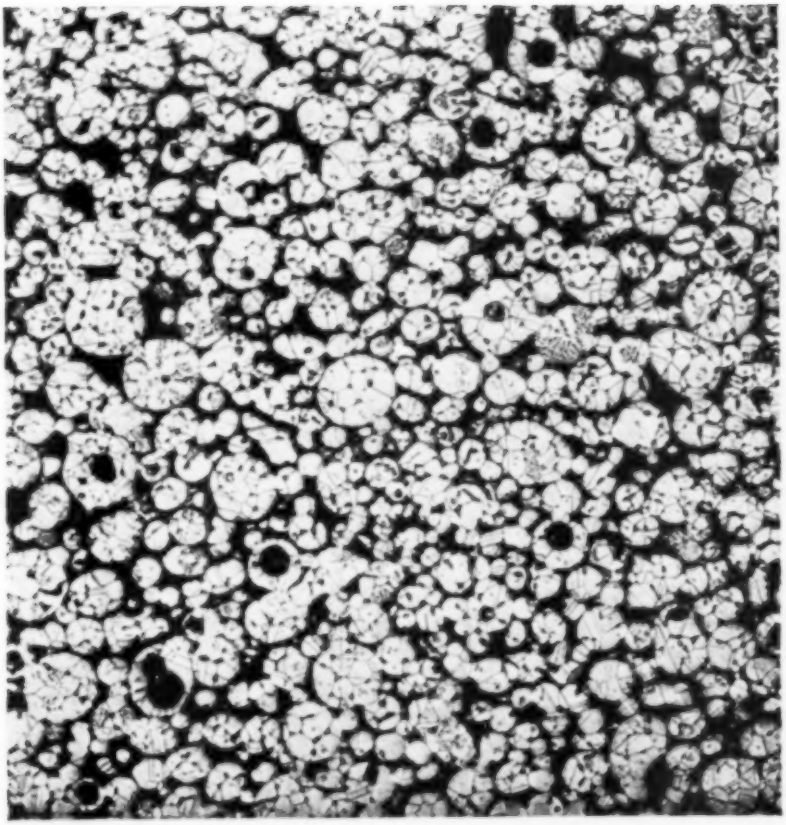

FIG. 2. Photomicrograph of F–B2–12 Core (× 250) after polishing.

FIG. 3. Photomicrograph of F–Br4–32 core after polishing.

cylinder gas manifold mounted outside of the barricade.

Some runs were attempted at lower temperatures by packing crushed ice around the sample and filling the water bath with an ice–brine mixture. At high flow rates, however, it was rather difficult to maintain a constant temperature by this method; consequently, data from only one sample has been reported at a temperature below ambient conditions.

Further details of the experimental apparatus and method are available in ref. [12].

Results

A series of four to six runs at different temperatures was made for each of the six porous cores. The temperature range was between 15 °C and 60 °C. Pressure gradients ranged from 790 p.s.i./in. for the S–T–1 core to about 25 p.s.i./in. for the K–C–1 core; these corresponded to a volumetric flow rate of approximately 100 ft³/hr, which represented the maximum obtainable with the flow measuring apparatus. Fig. 5 is presented as an example of the type of data obtained. This is the data for the K–C–1 core. The complete data is available in ref. [11, 12].

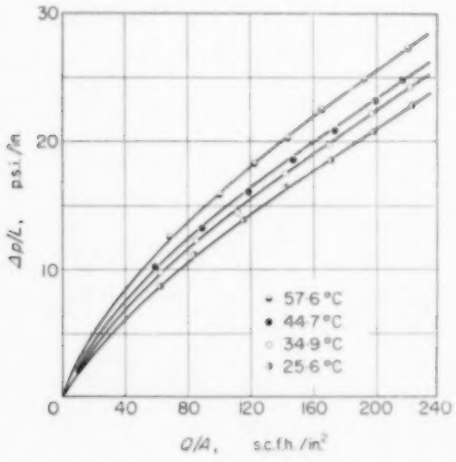

Fig. 5. Pressure drop vs. flow rate curve for K–C–1 core.

◒ 57·6 °C ● 44·7 °C
○ 34·9 °C ◑ 25·6 °C

Values of α and β were determined according to equation (4). As an example of the Cornell and Katz plots which were made, the plot corresponding to the data of Fig. 5 is given in Fig. 6.

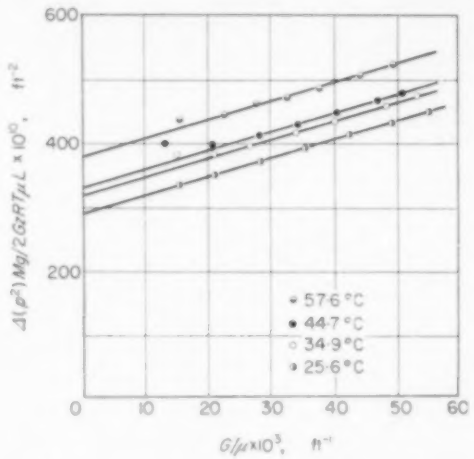

Fig. 6. Cornell and Katz plot for K–C–1 core.

◒ 57·6 °C ○ 34·9 °C
● 44·7 °C ◑ 25·6 °C

In the majority of cases, the data were easily fitted by eye to a straight line, as predicted by equation (4). However, for certain cores, there was an upward deviation of the points in the low flow rate region at elevated temperatures. For these cases, the higher flow data points were used to define the curves. The reasons for this are explained in the Discussion.

The values of α (and the corresponding permeability, k) and β obtained for the six cores are presented in Table 2 as functions of temperature.

Calculated permeabilities range from about 4 millidarcies (mdar) for core S–T–1, having the

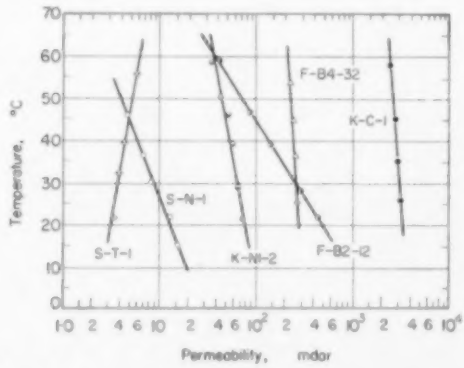

Fig. 7. Permeability vs. temperature for porous cores.

Table 2. Values of α, β and k

Core	*T* (°C)	α ($ft^{-2} \times 10^{-10}$)	β ($ft^{-1} \times 10^{-5}$)	*k* (mdar)*
K–N1–2	58·6	272	256	34·6
	50·2	215	256	43·8
	45·9	183	256	51·6
	38·9	164	256	57·6
	28·9	142	256	66·4
	21·5	128	256	73·9
K–C–1	57·6	3·94	2·79	2460
	44·7	3·33	2·79	2830
	34·9	3·24	2·79	2900
	25·6	2·99	2·79	3150
F–Br4–32	53·4	42·2	62·8	223
	44·4	39·3	62·8	240
	35·9	37·4	62·8	252
	25·4	35·8	62·8	263
S–T–1	21·4	2820	1860	3·34
	32·5	2480	1860	3·80
	39·4	2160	1860	4·35
	55·6	1620	1860	5·80
S–N–1	45·1	2050	2750	4·59
	35·4	1380	2750	6·82
	30·0	1180	2750	8·01
	21·7	835	2750	11·30
	15·1	618	2750	15·30
F–B2–12	58·8	226	203	41·7
	46·4	108	203	86·9
	38·7	66·1	203	143
	27·2	32·2	140	293
	21·6	21·8	140	434

*1 mdar = $1{\cdot}06 \times 10^{-14}$ ft^2

smallest mean pore dimension, to 3000 mdar for core K–C–1, which had the largest mean pore size value. Fig. 7 is a graph of permeability plotted against temperature for all of the samples studied. These curves were fitted to the data by the usual least squares technique, assuming that the relationship was linear over the range of temperatures investigated. In all cases except core S–T–1, permeability decreased with increasing temperature. The percentage change of permeability with temperature has also been tabulated from the graph in Table 3 as:

$$\frac{\Delta k/k}{\Delta T} = \text{per cent change in } k \text{ per } ^\circ\text{C}$$

where $\Delta k/k = k\,(60\ ^\circ\text{C}) - k\,(20\ ^\circ\text{C})/k\,(20\ ^\circ\text{C})$

and $\Delta T = 40\ ^\circ\text{C}$.

Fig. 8 is a representation of the data according to equation (7). The values of α and β presented in Table 2 were used for the calculation of the Reynolds numbers. The line is the C_f calculated from equation (7).

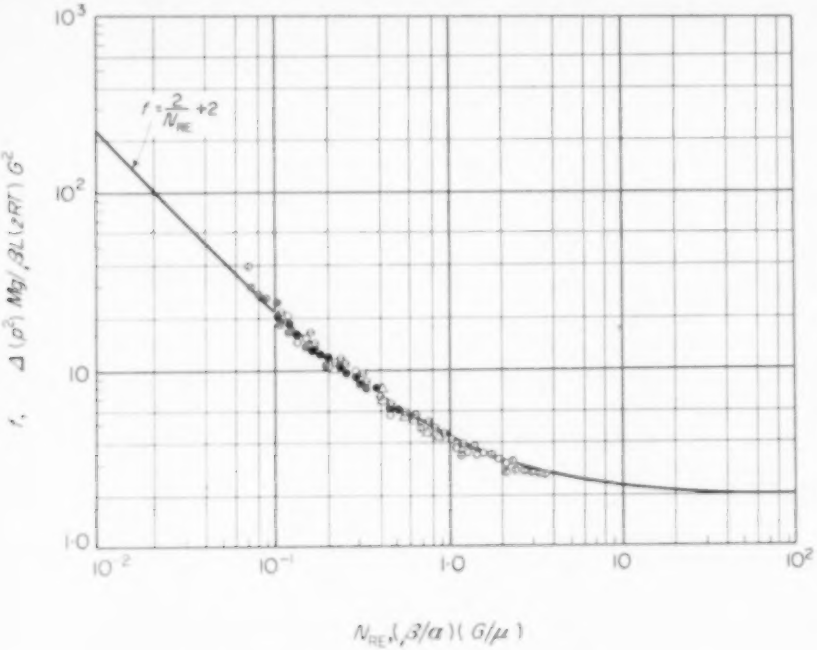

Fig. 8. Friction factors vs. Reynolds number.

⊖ S–T–1 ● K–C–1 △ F–B4–32
◒ K–N1–2 ◑ F–B2–12 ○ S–N–1

Table 3. Thermal coefficient of permeability

Core	*Porosity (From density measurements)* (%)	$\frac{\Delta k/k}{\Delta T}$ (°C^{-1})
S–T–1	39·4	1·28
S–N–1	32·9	2·62
K–N1–2	33·0	1·37
K–C–1	37·6	0·64
F–B2–12	35·7	2·62
F–Br4–32	43·7	0·52

Discussion

It was mentioned previously that in some cases the experimental data deviated from straight line behaviour when plotted according to the method of Cornell and Katz. This occurred especially for the S–N–1, K–N1–2 and K–C–1 cores in the low flow rate region at elevated temperatures. The effect can be attributed to the heat transfer which took place between the metal and the gas in the cores.

Because of the Joule–Thomson cooling effect, the gases were heated as they expanded in the cores so that the operation would remain essentially isothermal. This required that the temperature of the solid be somewhat higher than that of the gas. In the flow regions where the heat transfer was reasonable efficient, i.e., where appreciable inertial effects existed, the temperature gradient could be low and the required heat would still be transferred. At low flow rates, however, the major amount of heat is transferred to the bulk of the gas by conduction and this means that the temperature gradient must increase to maintain an adequate heat supply to the gas. The temperature of the porous medium in this case would then have to be considerably above the temperature of the gas (which was the temperature which was actually measured at the inlet and outlet to the core – since the actual core temperature would have been difficult to obtain). This conclusion is borne out by the fact that temperature control in this

region was considerably more difficult than in other regions.

The curves which would be obtained by drawing a line through the flow rate points in the higher temperature region for the S–N–1, K–N1–2 and K–C–1 cores would, therefore, not be expected to represent isothermal core conditions. Therefore, in these cores, in view of the lack of data on actual core temperature, it was considered more reliable to take the data at the higher flow rates as representative of the conditions of the cores at temperatures close to that of the gas. These data gave a straight line behaviour which was consistent with the data at lower temperatures. This linear behaviour indicates k and β are independent of flow rate or pressure for the materials under consideration.

Examination of Table 2 reveals the behaviour of k and β as a function of temperature. β is, in all except one case, independent of temperature within experimental error. The F–B2–12 data is anomalous in that above 27° there is an abrupt increase in β. This may have been due to a structural change with pressure, or the penetration of some unknown obstruction into the core. Despite these apparent discrepancies, however, the weight of the evidence seems to be that the inertial coefficient β does not vary appreciably with temperature for any given core.

In view of the invariance of β, the strong temperature dependence of the permeability is remarkable. This is an effect which had not been previously reported in the literature and may explain some of the "scatter" in permeability data for sintered metals which has been reported.

In all except one of the reported cases, k decreases with temperature. To arrive at a reasonable explanation for this effect, we must consider the physical significance of k and β. In some complicated fashion the permeability is a measure of the free cross-sectional area and length of flow path in the porous media. (These quantities, of course, consist of integrated averages for a macroscopic section of material). In other words, the reciprocal of k, α, is a viscous resistance coefficient. Let us restrict ourselves for the moment to one hypothetical "path" in the porous material. The fluid in the "path" (a quantity which varies, of course, because the passage is not enclosed) will encounter successively portions which have relatively large cross-sections followed by narrower passages near the points of contact of the spherical particles which constitute the porous sintered medium. Velocities will be higher at and near these "constrictions," and, therefore, the largest portions of the pressure drop along the path will occur there. The major contribution to the overall measured viscous resistance coefficient will, therefore, also originate at these constrictions.

As was mentioned previously, the pore size distribution measurements are primarily measurements of these constrictions. We can calculate an average pore size from these data by taking the midpoint of each size range, squaring it, and multiplying it by the appropriate volume. The square root of the sum, weighted by the appropriate total volume, represents an average pore diameter. It is a rather rough average, because of the approximations involved in taking the midpoint of each range as the representative diameter. Nevertheless, it should give some indication of the magnitude of the "constrictions" we are dealing with. It would be expected that the permeability coefficient is related to this average diameter – at least for similar types of media. That this is, indeed, so is evident from Table 4.

Table 4. *Comparison of permeabilities and mean pore diameter at approximately* 22°

Core	$\sqrt{D^2}$ (μ)	k (md.cm)
S–T–1	0·885	3·34
S–N1–1	2·800	11·3
K–N1–2	10·000	73·9
F–B2–12	17·000	370·0
K–C–1	35·000	3152·0
F–Br4–32	5·58	263

While it is not possible to derive a simple functional relationship between k and $\sqrt{D^2}$, it can be seen that the first five cores in the above table follow the same progression in k as in $\sqrt{D^2}$. The F–Br4–32 core, being composed of irregularly

shaped particles rather than spheres, would not be expected to fall in the same progression.

The factor β is a quantity related to the relative amount of resistance to flow existing in the porous medium due to inertial effects. In such a medium, these effects can arise due to several phenomena. The continuous expansion and contraction of the gas streams would certainly be one. Inertial resistance is also caused by the many curvatures in flow path as the gas wends its way through the material. Another important source of these effects is surface roughness, just as an increase in the roughness of a pipe wall causes increased pressure drop for flow through the pipe. The amount of roughness in a sintered porous medium is, of course, difficult to define. It is probable that a certain amount is present on the particles before sintering. The sintering process causes small blisters and other surface irregularities to arise in the surfaces, especially near the points of metal-to-metal contact. This is borne out by examination of photomicrographs of the media. Since the velocities are largest near these contact points, the amount of roughness in these locations will markedly affect the total pressure drop through the medium.

Since, as discussed previously, β remains constant as the temperature of a sintered porous element is varied, it is apparent that its general structure remains the same—at least for a moderate temperature range. That is, the configuration of the flow paths and the general character of the gas–solid interface is not altered.

Examination of the data reveals that the effect of the inertial and viscous terms on the pressure drop was of the same order of magnitude. The factor α is much larger than β, but, as can be seen in equation (1), it is multiplied by the viscosity of the gas—a small quantity.

The five porous cores used in the present investigation which were made from spherical powder particles all had porosities in the same range. It may, therefore, be assumed that, aside from surface irregularity effects, the internal structures of all five samples were very similar, even after sintering. Examination of the pore size distribution curves bears this out. The regular relationship between increasing $\sqrt{D^2}$ and increasing k, mentioned previously, is further proof. Excluding surface roughness effects, the β/α ratio should, therefore, be the same for all of the cores under discussion.

It is believed that the variation of k with temperature is mainly due to the presence of these surface irregularities where the flow passages are narrow. Let us first, however, examine the feasibility of another possible explanation of this effect. At first, it might be attributed to the normal thermal expansion of the metal particles which constitute the media. The thermal coefficients of expansion for the metals whose powders were used to fabricate the cores and sleeves used in the present study are tabulated in Table 5.

Table 5. Thermal coefficients of linear expansion for various metals

Metal	*Coefficient of linear expansion* $\times 10^6$/°C
Copper	16·5
Nickel	13·3
Brass	20·0
Bronze	18·3
Tungsten	4·3
Steel	12·0

It is evident that the total thermal expansion of the metal particles over the temperature range used in the present study is negligible. Furthermore, the coefficients (except for tungsten) are all of the same order of magnitude. Therefore, it is apparent that the cause for the large temperature coefficient of k, which varies much more widely between different samples than the thermal coefficient of expansion, must lie somewhere else.

As mentioned previously, it is believed that the root of the trouble can be traced to the surface irregularities existing at the points where the greatest viscous resistance effects occur. Any slight change in the position or size of the irregularities can greatly affect the already relatively small opening available for the passage of the gas there. A small change in temperature of the medium, while causing no appreciable overall expansion of the particle, can cause a small shift in position of, plus small expansion effects in,

the surface irregularities at the constrictions (also at other parts, of course), causing a sort of "pinch" effect. This would greatly change the viscous resistance at these points and, therefore, the overall k. Since the quantity β/α, or βk, is a measure of the relative inertial to viscous resistance effects in the media, it is of interest to look at the variation of this quantity with the thermal coefficient of k for some of the materials tested. This data is presented in Table 6.

Table 6. *Comparison of thermal coefficients of permeability with* β/α

Core	$\frac{\Delta k/k}{\Delta T}$ (%/°C)	$(\beta/\alpha)(\text{ft}^{-1} \times 10^{5})(25\ ^{\circ}\text{C})$
K–C–1	0·64	0·93
K–N1–2	1·37	1·90
S–N1–1	2·62	2·75
F–B2–12	2·62	4·80

While the relationship is not entirely consistent due to the fact that two different values of β/α are obtained for the S–N–1 and the F–B2–12 cores, while their thermal permeability coefficients are the same, the tendency for $(\Delta k/k)/\Delta T$ to increase as β/α increases can be seen. As mentioned previously, differences in β/α among the cores composed of spherical particles can be ascribed mainly to differences in surface effects. Apparently, minute changes in orientation and/or positions of blisters and other surface outcroppings due to temperature variations greatly affect the permeability of the sintered porous media. This effect would be expected to be greatest at positions in the cores which exercise the largest influence on k; i.e., the points at which the highest velocities occur. The greater the roughness effects, as measured by the β/α parameter, the greater will be the temperature coefficient of permeability. The overall change in porosity due to this effect is negligible. This was borne out by the pore size distribution measurements. No significant changes in porosity with temperature were noted for the four cores for which measurements were made at two temperatures. There is evidence of some change in pore size distribution with temperature (see Fig. 1), but at present it is not clear just how this change affects the phenomena which have been discussed. The mercury intrusion measurements, involving determination of broad ranges of pore sizes could not be expected to pick up the fine variations which have been discussed.

For the same reason as before, the F–Br4–32 core would not be expected to fit into this scheme because of the different nature of the powder used in its fabrication. But the explanation for its large thermal permeability coefficient is probably the same as set forth above.

The temperature coefficient of permeability of the S–T–1 core is opposite in sign to all the other coefficients. The reason for this is readily apparent. The tungsten core was "sweated" into its steel sleeve rather than being "potted," as were the other cores. As can be seen from Table 5 previously presented, the linear coefficient of thermal expansion of steel is approximately three times that of tungsten. Assuming that at 20 °C the tungsten was perfectly sealed in the sleeve, any rise in temperature would cause greater expansion of the inside surface of the sleeve than of the outside surface of the tungsten. The increase of permeability of the S–T–1 core was, therefore, apparently caused by the creation of additional free cross-sectional area at the tungsten–steel interface.

Conclusions

The present study has demonstrated that the inertial and viscous coefficients in the equation describing flow through porous media are independent of pressure at pressures up to 2000 p.s.i. for sintered metal compacts. It is, however, necessary to take into account variations of the permeability with temperature – even over narrow temperature ranges. A decrease in permeability as the temperature of the medium is raised may also occur in porous materials other than sintered metals. It is likely that the behaviour of porous surfaces such as are used in aerodynamic structures, and porous materials, such as solid propellants, are significantly affected by this phenomenon.

It is also clear that more attention and study must be devoted to the internal surface structure

of porous materials if some degree of control is to be exercised over the thermal coefficient of permeability. Since the degree of "roughness" of the internal surface apparently determines this coefficient, minimization of the variation of permeability with temperature might be achieved by controlled particle sizing, more gradual sintering, etc.

Pore size distribution measurements of sintered porous media are valuable for the determination of the existence of structural similarity among various porous materials. For different sintered compacts which are composed of particles of the same shape, e.g. spheres, the mean pore diameter calculated from these measurements gives an indication of the order of their permeabilities.

Acknowledgements—The authors wish to express their appreciation to the Office of Ordnance Research and the Ballistic Research Laboratories of Aberdeen Proving Ground of the Department of the Army for their sponsorship and support of the work presented in this paper.

Notations

A	= cross-sectional area of porous core in the direction of flow	(ft^2)
D	= average pore diameter	μ
G	= gas mass velocity (based on empty cross-section)	($lb/hr\ ft^2$)
g	= conversion factor	($32{\cdot}17\ lb_M\ ft/lb_F\ sec^2$)
k	= permeability	(mdar)
L	= length of porous sample	(in.)
M	= molecular weight	
N_{Re}	= Reynolds number	
N	= a constant	
p	= pressure	(p.s.i.a.)
Q	= volume flow rate at 20 °C and 14·7 p.s.i.a. (s.c.f.h.) (based on empty cross-section)	
R	= gas constant	
T	= gas temperature	(°C or °K)
V	= gas velocity	(ft/sec)
x	= linear distance co-ordinate	
z	= compressibility factor	
α	= viscous flow coefficient	(ft^{-2})
β	= inertial flow coefficient	(ft^{-1})
Δ	= a difference	
μ	= absolute viscosity of the gas	($lb/ft\ hr$)
ρ	= density of the gas	(lb/ft^3)

References

[1] Muskat M. *Flow of Homogeneous Fluids through Porous Media*. McGraw-Hill. New York 1937.

[2] Muskat M. *Physical Principles of Oil Production*. McGraw-Hill. New York 1949.

[3] Hubbert M. K. *J. Geol.* 1940 **48** 785.

[4] Duwez P. and Wheeler H. L. *J. Aero. Sci.* 1948 **15** 509.

[5] Mickley H. S. and Davis R. S. National Advisory Committee for Aeronautics. TN 4017 1957.

[6] Grunberg L. N. and Nissan A. H. *J. Inst. Petrol. Tech.* 1943 **29** 192 1943.

[7] Green L., Jr. and Duwez P. *J. Appl. Mech.* 1951 **18** 39.

[8] Brownell L. E., Dombrowski H. S. and Dickey C. A. *Chem. Engng. Progr.* 1950 **46** 415.

[9] Darcy H. P. G. *Les Fontaines Publiques de la Ville de Dijon*, Victor Dalmont, Paris 1856.

[10] Cornell D. and Katz D. L. *Industr. Engng. Chem.* 1955 **47** 1379.

[11] Greenberg D. B. M.Sc. Engineering Essay, Johns Hopkins University, Baltimore, Maryland 1959.

[12] Weger E. and Greenberg D. B. Interim Technical Report No. 1, Department of the Army Project No. 5B99-01-004, Contract Nos. DA-36-034-ORD-2353, DA-36-034-509-ORD-3rd.

[13] Winslow, N. M., Prado Laboratories, Cleveland, Ohio. Private communication.

Chemical Engineering Science, 1960, Vol. 12, pp. 20 to 34. Pergamon Press Ltd., London. Printed in Great Britain

Longitudinal mixing in packed beds

E. J. CAIRNS* and J. M. PRAUSNITZ

Department of Chemical Engineering, University of California, Berkeley, California

(*Received* 1 *June* 1959; *in revised form* 29 *July* 1959)

Abstract—Longitudinal mixing properties were investigated for a water stream flowing through 2 in. and 4 in. tubes packed with 1·3, 3·0 and 3·2 mm spheres over the Reynolds number range 3 to 4500. The method of injecting a step function of salt solution through a simulated plane source was used, coupled with electrical conductivity measurements with very small probes. This method is not limited by the assumption of a flat velocity profile.

The statistical model proposed by EINSTEIN is tested and found to be applicable over the entire range of all variables studied. The results are reported in terms of an eddy diffusivity as a function of hydraulic radius and line velocity which are proposed as the characteristic length and velocity terms.

The observed eddy diffusivities are somewhat lower than those of other investigators who used radially integrated rather than point measurements of the breakthrough curve. It is shown that the integrated results are too high due to a non-flat velocity profile.

Résumé—Les auteurs ont examiné les propriétés du mélange longitudinal dans un courant d'eau passant dans des tubes de 2 à 4 in. garnis de sphères de 1,3 – 3,0 et 3,2 mm pour un nombre de Reynolds compris entre 4 et 4 500. La méthode consiste à injecter par impulsion une solution saline au moyen d'une source plane. Cette méthode n'est pas limitée par l'hypothèse d'un profil plat de vitesse.

Le modèle statistique proposé par EINSTEIN est examiné et les auteurs ont trouvé qu'il s'appliquait à la série entière de toutes les variables étudiées. Les résultats sont donnés au moyen d'une diffusion turbulente fonction du rayon hydraulique et de la vitesse linéaire qui sont proposés comme termes caractéristiques de longueur et de vitesse.

Les valeurs de la diffusion turbulente observée sont un peu plus faibles que celles d'autres chercheurs. Ceux-ci utilisèrent des valeurs moyennes prises sur le rayon au lieu de valeurs measurées point par point sur la courbe.

Il semble que les valeurs moyennes sont trop élevées du fait d'un profil de vitesse non linéaire.

Zusammenfassung—Die Besonderheiten der Längsdurchmischung wurden für einen Wasserstrom untersucht, der durch ein 5 cm und 10 cm Rohr fliesst; das Rohr ist mit 1,3; 3,0 und 3,2 mm Kugeln gefüllt für einen Bereich der Reynoldszahl von 3 bis 4 500. Die Methode des schrittweisen Einspritzens einer Salzlösung durch eine simulierte, ebene (flächenförmige) Quelle wurde angewandt, zusammen mit elektrischen Leitfähigkeitsmessungen mit sehr kleinen Probemengen. Diese Methode wird nicht durch die Annahme eines ebenen Geschwindigkeitsprofils eingeschränkt.

Das von Einstein vorgeschlagene statistiche Modell wird geprüft und als anwendbar für den gesamten Untersuchungsbereich aller Variablen gefunden. Die Ergebnisse werden in Form eines turbulenten Diffusionskoeffizienten als Funktion des hydraulischen Radius und der linearen Geschwindigkeit dargestellt, die als charakteristische Länge und Geschwindigkeitsausdrücke vorgeschlagen werden.

Die beobachteten turbulenten Diffusionskoeffizienten sind etwas kleiner als die von anderen Autoren, die radial integrierte und keine Punkt-Messungen für die Durchbruchskurve verwandten. Es wird gezeigt, dass die integrierten Ergebnisse infolge eines unebenen Geschwindigkeitsprofils zu hoch sind.

*Present address: General Electric Research Laboratories, Schenectady, New York.

Introduction

During the last few years, increased attention has been focused on the problem of longitudinal mixing in packed bed systems, using both gases and liquids as the fluid media. This mixing phenomenon is important because of its influence on the performance of packed bed reactors, mixers, and extractors. In the case of reactors and extractors, this mixing process decreases the effectiveness of the apparatus. A study of the extent and variation of the longitudinal mixing properties of packed bed systems leads to a more thorough understanding of the fluid dynamics and tubulence properties of such flow systems.

Several investigators [1, 2, 3, 4, 5, 6, 7, 8, 15, 24] have studied longitudinal mixing in the liquid phase in packed beds, using various types and sizes of packing material. The most popular methods of tracer injection have been the pulse function [2, 5] and the sinusoidal concentration wave [4, 5, 6, 7, 8]. All of the experimental results have been analysed on the basis of the diffusion model. In the case of the diffusion model, the familiar type of differential equation is solved, usually assuming an infinitely long packed bed. Some investigators [2, 6, 7, 9] have solved equations representing the longitudinal mixing process as analagous to that of dispersion resulting from a fluid stream passing through a series of stirred tanks. When the results of the stirred tank model are made consistent with the diffusion model, it is possible to estimate a value for the longitudinal Peclet group.

The purpose of this investigation was to determine the longitudinal mixing characteristics of a packed bed, using experimental methods which allowed maximum possible freedom from previous assumptions limiting the validity of the results, and to test the applicability of a statistical model. This model does not require the diffusion assumption which is valid only in long beds nor the perfect cell mixer assumption which contains parameters difficult to evaluate; nor does it require the introduction of an additional parameter, such as mixing efficiency, or a bed capacitance term. The statistical theory was first introduced by Einstein [10] to describe the motion of pebbles under the influence of a water stream. It has the advantage of being applicable for any length of bed, however short.

Theory

The theory for longitudinal mixing in packed beds based on the Einstein statistical model has been derived and discussed in detail elsewhere [11, 15, 24]. For convenience in use for the present discussion, the essentials are summarized. The model considers the motion of corpuscles of tracer material in the mainstream fluid. The tracer corpuscles alternately experience rest phases and motion phases, whereby the motion phases require a small amount of time compared to the time interval required for the rest phases. The rest phases may be assumed to occur at stagnation points at each packing particle and the motion phases occur in the void spaces through which the fluid moves at high velocity.

The probability density function for the corpuscle in time and space (one dimensional, longitudinal) is given by:

$$p(z, \tau)\, dz d\tau = \exp(-z\ \tau)\, dz d\tau \qquad (1)$$

where $p(z, \tau)$ is the probability density for the tracer corpuscles at a longitudinal distance z from the point of introduction and time t after the introduction.

z is the dimensionless longitudinal distance from the tracer source.

τ is the dimensionless time since the corpuscle of tracer entered the system.

As described previously [11, 15], equation (1) is applied to a consecutive set of n motion phases and n rest phases after which the tracer corpuscle is found at the position $z = N$ at the time $\tau = T$. The considerations are treated in such a manner that all possible paths for arriving at N at time T are taken into account, finally arriving at the expression

$$F_{N(T)} = \int_0^T \exp(-N - T)\, I_0(2\sqrt{NT})\, dT \qquad (2)$$

where T = a dimensionless time.

N = a dimensionless longitudinal distance (from the tracer source).

I_0 = Bessel function of zero order and first kind of an imaginary argument.

The symbol $F_{N(T)}$ represents the probability of finding a tracer corpuscle at position $z = N$ at time T, where tracer corpuscles originate (at $z = 0$) continuously and at a steady rate starting at zero time. This definition of $F_{N(T)}$ corresponds to a step function tracer input.

The important assumptions in the development were:

1. Flat mainstream velocity profile over the small region of interest.
2. The probability of a tracer corpuscle coming to rest is independent of time and position.
3. The time required for a motion phase is small compared to that required for a rest phase.

Equation (2) is difficult to evaluate; therefore an approximate form [12], [13] may be used:

$$F_{N(T)} = \frac{1}{2}\left[1 + \operatorname{erf}\left(\sqrt{T} - \sqrt{N} - \frac{1}{8\sqrt{T}} - \frac{1}{8\sqrt{N}}\right)\right] \quad (3)$$

The relationships between T and N and the more familiar eddy diffusivity E and time t are given by

$$N = \frac{ZU}{E} \quad (4)$$

$$T = \frac{U^2 t}{E} \quad (5)$$

$$T/N = \frac{Ut}{Z} \equiv \theta \quad (6)$$

$$\therefore \mathrm{Pe} = N\frac{d_p}{Z} = \frac{Ud_p}{E} \quad (7)$$

Equation (4) is a definition of the eddy diffusivity in terms of the Einstein statistical equations. The numerical value of the eddy diffusivity is equal to that obtained from the same data analysed on the basis of the diffusion model when the beds are long enough ($N > 50$).

The familiar breakthrough curve for a step function input is obtained by plotting $F_{N(T)}$ as in equation (3) versus (T/N) for a given value of N. The most convenient method for evaluating the Peclet group from the F curve is to obtain the slope $(\partial F/\partial\theta)$ at the point $\theta = 1$, since from equation (2) one may obtain [11]:

$$\left(\frac{\partial F}{\partial \theta}\right)_{\theta=1} = N\frac{I_0(2N)}{\exp 2N} \quad (8)$$

For large N, it may be shown that

$$\mathrm{Pe} = N\frac{d_p}{Z} \simeq 4\pi\left(\frac{\partial F}{\partial\theta}\right)^2_{\theta=1}\frac{d_p}{Z} \quad (9)$$

Equation (8) indicates that this method of calculation of the Peclet group is very rapid and requires considerably less calculational procedures than other methods [2, 4, 5, 8, 9, 12, 13].

Experimental

The method employed for investigation of the axial mixing properties in packed beds was that of a step function injection of tracer solution. In this case, the tracer was a sodium nitrate solution and the detection method was that of electrical conductivity. The mainstream was tap water from a constant-head tank about 35 ft above the test section.

General flow apparatus

A schematic flow diagram of the apparatus is shown in Fig. 1. A 5 h.p. regenerative type turbine pump was used for the mainstream, since this type of pump is capable fo delivering medium flow rates at high pressures with negligible surges and fluctuations. Calibrated rotameters and globe or needle valves were used to regulate the flow. The flow distributor which was designed to give a flat velocity profile is discussed in detail elsewhere [11].

The test section for most of the data reported here was a two-feet high, 2 in. glass pipe section composed of four 6-inch lengths flanged together, allowing the conductivity cell leads to emerge from the test section between the gasketed flanges. Some data are included from a 4 in. test section and a different probe arrangement described elsewhere [11]. The overflow tank allows drainage of the fluid without influence on the test section.

The packing particles were spherical in all cases. The particle diameters studied were 1·3,

3·0 and 3·2 mm. Bed heights varied from 5·6 to 24 in.

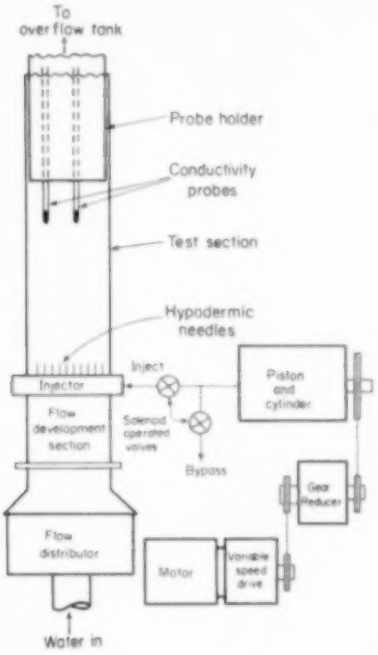

FIG. 1. Schematic flow diagram.

Injector system

The tracer injector system consisted of a piston and cylinder driven by a Graham variable speed drive and gear reducer unit. The speed of the piston was determined as a function of the drive speed regulator position.

The injector head for the packed bed was constructed from 18 gauge hypodermic needles arranged on a 9/32 in. square lattice. There were 37 needles in the 2 in. plane source, and 156 needles in the 4 in. plane source.

Calculations were performed in order to determine a reasonable needle spacing for the assumption of a plane source. KLINKENBERG *et al.* [12] solved the equations describing the spreading of a tracer from a point source into a moving fluid stream where axial and radial mixing rates are not assumed equal. KLINKENBERG's results were used for calculation of the lateral concentration profiles at various distances downstream from the source. The method of superposition was used for the construction of concentration maps for various needle spacings at various distances from the source. Details of the calculations are described elsewhere [11]. The results for these injectors show that a distance of about $\frac{1}{2}$ in. downstream from the injectors there is only 9 per cent " ripple " in the concentration map. This shows that the radial diffusion necessary to establish a plane concentration front occurs very rapidly with respect to the longitudinal diffusion which is detected at a distance of 18 in. downstream. Hence, the radial diffusion effects have a negligible effect on the longitudinal diffusion results.

Fig. 2 shows a photograph of the 4 in. plane source. The body of the source is hollow, allowing the tracer solution to flow into the ends of the $\frac{1}{8}$ in. cross tubes supporting the needles. Calculations showed that the pressure drop through each needle was about 100 times as large as the pressure drop through the $\frac{1}{8}$ in. cross tubes, and much larger compared to the pressure drop through the inside of the injector body. Therefore, an even distribution of injectant was to be expected. This was observed to be the case. The injector was mounted directly above the flow development section as shown in Fig. 1.

The solenoid valve arrangement allowed a very rapid action either for turning on or turning off the flow of the injectant into the test section. Two valve arrangements were used to test the effectiveness of the step function generation by the valves.

The first unit was constructed such that there was a General Controls Magnetic Valve type K21-F within 4 in. of the injector head, and another on the by-pass pipe as shown in Fig. 1. By throwing a single switch, one valve was opened and the other was simultaneously closed. The valves were installed such that the direction of fluid flow assisted the rapid closing action.

The second unit was composed of a General Controls type K21-F Magnetic Valve on the by-pass pipe, and a Jamesbury stainless steel rapid-action ball-type valve actuated by two large solenoids and an aluminium linkage system arranged to give a push-pull action for turning the valve stem which had a long aluminium

lever mounted on it. The Jamesbury valve was mounted about 4 in. from the injector head. Both valve units gave identical results for the Peclet group at identical flow rates. The initial testing of the valve units made use of a conductivity cell at a needle tip. The cell was connected through the electronics to a high-speed recorder having a chart speed of 25 in./sec. Both valve arrangements gave a very sharp step function response even down to very low injection rates (about 0·0006 gal/min).

Probes and electronics

The probe used for most of the packed-bed studies is shown in Fig. 3. This probe is constructed from packing units of a size identical to the rest of those used in the bed. The leads were strung with perforated beads so that they could be led out of the bed between the flanges with a minimum of disturbance to the rest of the packing. The electrode faces of the probe were parallel and the plane of the probe was perpendicular to the main direction of fluid flow in order that no hold-up be allowed within the conductivity cell. The cell was constructed in such a manner that only the fluid in the interstitial space formed by the probe contributed to the conductivity.

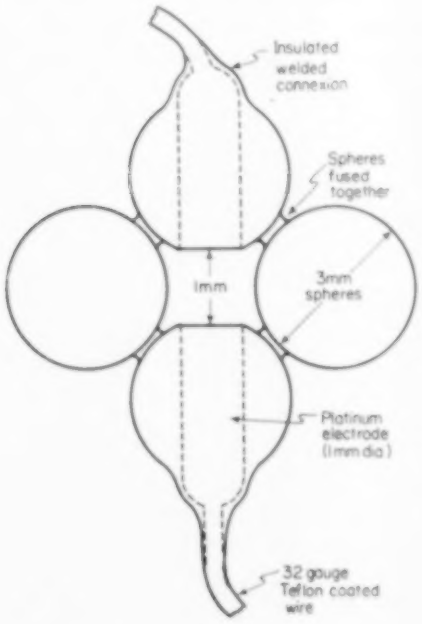

Fig. 3. Packed bed conductivity cell.

The basic circuit is shown in Fig. 4. A constant voltage 20 kc oscillator used as the voltage source was connected across the conductivity cell and the current detector resistance r. The voltage across r is proportional to the conductance of the solution in the cell, $1/R$, providing r is always small compared to R. Therefore, by amplifying and demodulating the signal V_r, a voltage directly proportional to the solution conductance may be recorded. Six parallel channels were used, in order that the conductance of up to six cells could be recorded simultaneously. The amplifier–demodulator channels had a linear gain of up to 250. The gain was variable continuously from 0 to 250. Capacitance effects for both types of cells were measured and found to be negligible. Careful shielding and grounding practices were utilized.

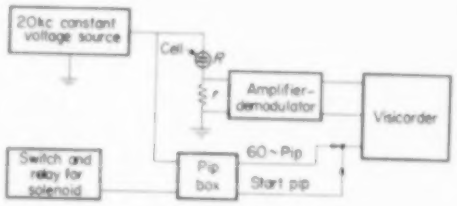

Fig. 4. Block diagram for one channel.

Fig. 4 shows a block diagram of the overall circuit for one channel. Six channels in parallel were used for most of the work. The pip box is a device which electronically placed a pip in the reference trace of the recorder every 1/60th of a second. The box was activated by a 20 kc signal so that the error in pip placement is negligible. The pip box also puts a separate additional pip on the chart at the moment when the injector solenoid valve switch was thrown. The accuracy of the start pip placement was within 0·01 sec. This slight error is due to the small but variable delay in the solenoid action due to the phasing of the 60 c voltage source for the solenoids at the moment that the switch was thrown. This error

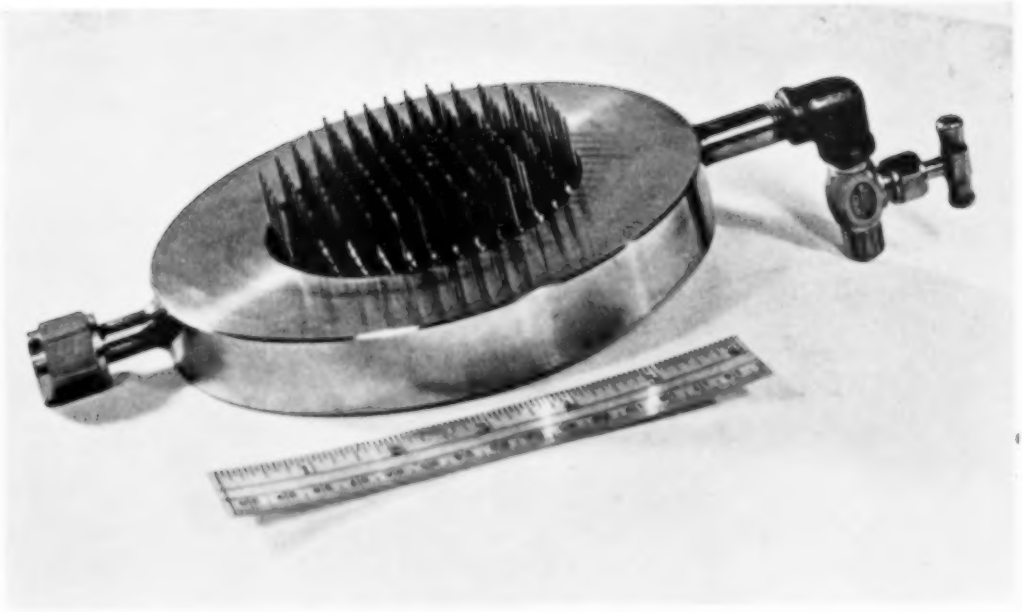

FIG. 2.

was negligible except at extremely high Reynolds numbers.

The high-speed multichannel recorder was a Minneapolis-Honeywell Visicorder model 906. The traces on the chart were the result of the motion of mercury vapour light spots reflected from the mirrors of the bank of galvanometers mounted in the instrument. The deflection of the light spots was very nearly proportional to the voltage across the galvanometer and damping resistor. The frequency response of the instrument is such that transients up to 300 c/s may be followed with an accuracy of about 2 per cent.

Detailed circuit diagrams and descriptions for all of the electronic equipment except power supplies are available elsewhere [11].

Procedure

The injector drive setting was determined such that the linear speed of the injectant leaving the needles was equal to the average linear speed of the mainstream as calculated from the flow rate and fraction voids.

When steady state injection had been attained the run was started by turning on the chart drive and then causing the injectant stream to be instantaneously diverted to the bypass tube. At the same instant the pip box automatically placed a sharp start pip in the reference trace on the recorder chart.

The response curves for the shutting off of the tracer were used because of the advantage in being able to pre-set the gains and knowing the relative positions of the traces. It was found to be easier, in general, to turn off the flow of the injectant stream very suddenly than to turn it on, due to volumetric capacitance and momentum effects in the injector body. With proper care, however, identical results could be obtained from both types of curve. Data were collected for flow rates corresponding to Reynolds numbers $U_0 d_p \rho/\epsilon\mu$ from about 3 to about 4500.

Reduction of Data

In order to develop a rapid, simple method of calculation, an exact expression having the form of approximate equation (9) is desired. However, it is not possible to determine directly the location of the point $(T/N) = 1$ from the data without resorting to trial and error. For this reason, the slope of the F curve is taken at a point which may be located directly and simply. Such a point is $F = 1/2$.

Knowing the slope at the point $F = 1/2$, the slope at the point $T/N = 1$ may be calculated, using the derivative of equation (2) with respect to (T/N). Assuming a value for N, the corresponding T for $F = 1/2$ may be calculated from equation (3), and these values of T and N are inserted into the derivative of equation (2). Then $\partial F/\partial\theta$ at $F = 1/2$ is calculated. The value for the slope at $T/N = 1$ is found from equation (8) for this same assumed N. The ratio of the two slopes is defined as the correction factor β.

$$\beta = \frac{(\partial F/\partial\theta)_{\theta=1}}{(\partial F/\partial\theta)_{F=1/2}} \tag{10}$$

Therefore $(\partial F/\partial\theta)_{\theta=1}$ may be obtained directly from $(\partial F/\partial\theta)_{F=1/2}$ from a plot of β versus $(\partial F/\partial\theta)_{F=1/2}$.

Since equation (9) is only approximate, it is desirable to have a relationship between an equation having the form of equation (9), and the exact solution. The relationship is expressed in the form:

$$N = 4\pi \left(\frac{\partial F}{\partial\theta}\right)^2_{\theta=1} \frac{1}{\alpha^2} = 4\pi \left(\frac{\partial F}{\partial\theta}\right)^2_{\theta=1} \left[\frac{\exp(2N)}{2\sqrt{(\pi N)}\, I_0(2N)}\right] \tag{11}$$

For a general definition of α, see the Appendix. Equation (11) defines α for use in the present calculations. The calculation of the Peclet group now follows the form of equation (9), but is exact, whereas equation (9) is approximate:

$$\mathrm{Pe} = N\frac{d_p}{Z} = 4\pi \left(\frac{\partial F}{\partial\theta}\right)^2_{F=1/2} \left(\frac{\beta^2}{\alpha^2}\right) \frac{d_p}{Z} \tag{12}$$

Since the electrical conductance of the sodium nitrate solution which was used as a tracer is not exactly proportional to the concentration of the sodium nitrate, additional correction is necessary in order to provide a means of direct calculation of the Peclet group from the slope at $F = 1/2$ on the recorder chart. The form of the empirical

equation relating the salt concentration C to the conductance L is:

$$C = aL^b \tag{13}$$

where a = constant (strong function of temperature),
b = constant (weak function of temperature).

Equation (13) was used over the range $10^{-3} < C < 2 \times 10^{-2}\,N$, with good precision. The correction factor (which is developed in the Appendix) takes the form:

$$\left[b\left(\frac{L}{L_\infty}\right)^{b-1}\right]_{F=1/2} = \left[b\left(\frac{1}{2}\right)\right]^{b-1/b} \tag{14}$$

which is a weak function of temperature.

It was found that even though (L/L_∞) was very nearly equal to (y/y_∞) (where y is the displacement of the trace on the recorder chart, and the subscript ∞ indicates the steady state value during injection of tracer material),

$$\left[\frac{d\,(y/y_\infty)}{d\,(L/L_\infty)}\right]_{y/y_\infty \,=\, 1/2} = 1{\cdot}02 \tag{15}$$

Introducing equation (14) and equation (15) to equation (12), the final working equation for the determination of the Peclet group becomes

$$\mathrm{Pe} = 4\pi \left\{\frac{d\,(y/y_\infty)}{dx}\left[\frac{b}{1{\cdot}02}\left(\frac{L}{L_\infty}\right)\right]^{b-1} \times \left(\frac{Z}{U_l}\right)\left(\frac{dx}{dt}\right)\right\}^2_{F=1/2}\left(\frac{d_p}{z}\right)\Delta^2 \tag{16}$$

where $\dfrac{d\,(y/y_\infty)}{dx}$ = slope of the breakthrough curve on the recorder chart taken at $F = 1/2$,

L_∞ = steady-state conductance value during injection,

U_l = line velocity of the fluid $= \dfrac{1}{Z}\displaystyle\int_0^Z U_p\,dz$ where U_p = point velocity,

dx/dt = chart speed,

$\Delta^2 = \beta^2/z^2$.

The term in the large brackets is $(dF/d\theta)_{F=1/2}$.

Equation (16) provides a rapid method for reducing data from the experimental step-function method. For a plot of $\Delta^2 - 1$ versus $(\partial F/\partial\theta)^2_{F=1/2}$, see Fig. 5. Details of the foregoing discussion are given in the Appendix.

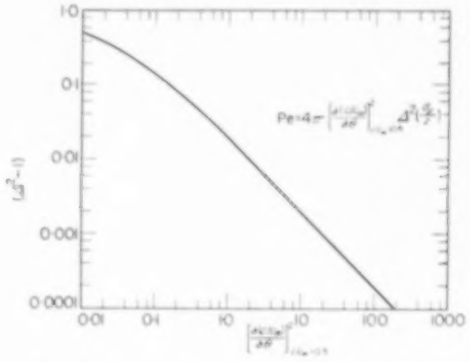

Fig. 5. Correction factor for obtaining Pe.

The eddy diffusivity E is found from

$$E = \frac{Ud_p}{\mathrm{Pe}} = \frac{UZ}{N} \tag{17}$$

where U is the characteristic fluid velocity.

Fig. 6 was prepared as a test of the validity of the model. The experimental points were obtained from the recorder chart. The linear velocity in the term Ut/Z was found from the start pip on the chart, the known Z, and the time required to reach the concentration which corresponded to the point for $(T/N) = 1$ from equation (3). This is a trial and error procedure; however (C/C_∞) for $(T/N) = 1$ is very close to $1/2$, so only one trial was necessary for sufficient accuracy ($\pm$ 1 per cent). The agreement between experiment and theory is well within experimental error.

In reducing the data as outlined above, the question of characteristic velocity arises. Previous investigators [2, 7, 15, 16, 17] have used the interstitial velocity as calculated from flow rates and fraction voids $U = U_0/\epsilon$. This is only satisfactory when the assumption of a flat velocity profile is valid [11, 18]. This assumption is very seldom justified, as may be seen from results on velocity profiles in packed beds [18, 19] and from a discussion which follows in the next section.

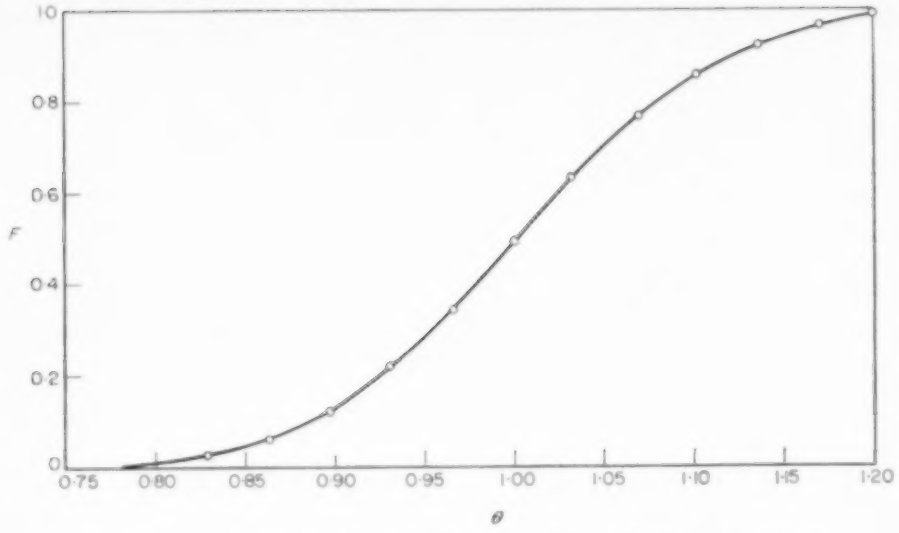

FIG. 6. Comparison of experiment to theory. $Pe' = 1{\cdot}2317$ $N = 235{\cdot}26$

Curve: $$F = \frac{1}{2}\left[1 + \operatorname{erf}\left(\sqrt{T} - \sqrt{N} - \frac{1}{8\sqrt{T}} - \frac{1}{8\sqrt{N}}\right)\right]$$

Data points: run 5, set 3, cell 13. $Re = 128$ $Z = 24{\cdot}0$ in. $U_l = 4{\cdot}125$ in/sec

The characteristic velocity which is thought to be the most valid here is that obtained from the rate of motion of the tracer through the column as characterized by the time interval between the start pip and the $T/N = 1$ point, which very closely corresponds to the $F = 1/2$ point in the range of variables studied here. This velocity is called the line velocity and is defined as:

$$U_l = \frac{1}{Z}\int_0^Z U_p \, dZ$$

where Z = the longitudinal distance from the injector to the point of observation.

U_p = the point velocity.

The nature of this definition is such that the velocity is averaged along a longitudinal element of the tube, but not radially, so that radial velocity variations have little or no influence on the line velocity as measured experimentally. This definition is also advantageous since a point velocity is not used. The velocity is averaged over essentially the same path as that corresponding to the longitudinal mixing process, and hence the mixing is characterized more closely by this velocity than by any other.

Results

In order to summarize the results it is necessary to know how the variables affect the eddy diffusion parameter. Previous investigators [2, 5, 7, 15] have plotted the Peclet group

$$Pe = \frac{U_0 \, d_p}{\epsilon \, E}$$

versus the Reynolds number

$$Re = \frac{U_0 \, d_p}{\epsilon \, \nu}$$

where U_0 = superficial velocity.

ϵ = fraction voids.

d_p = particle diameter.

ν = kinematic viscosity.

E = eddy diffusivity as calculated from the various experimental results using U_0/ϵ as the characteristic velocity.

One investigator [2] plotted E versus Re, and another [5] plotted (E/ν) versus Re. The effect of viscosity on eddy diffusivity has been investigated in the range of from 0·95 to about 28 cp by Ebach and White [5]. There was no detectable effect. None of the models or theories which have been proposed predict any type of viscosity dependence.

The model proposed by Prausnitz [23] gives a proportionality between the longitudinal eddy diffusivity and the product of interstitial velocity and particle diameter. The Einstein statistical model proposed in this work also predicts a proportionality between the longitudinal eddy diffusivity and the product of the characteristic velocity (U_l proposed in this work) and a characteristic length term. Therefore it does not appear appropriate to plot eddy diffusivity versus Reynolds number since the eddy diffusivity is in no way dependent on the kinematic viscosity.

The hydraulic radius as extended by Wilhelm [20] is proposed here as a characteristic length term for plotting purposes because it is not limited to packed beds, whereas the particle diameter as a characteristic length term loses its significance when applied to anything except a packed bed.

For data summarizing purposes, it is proposed that E be plotted against $4mU_0/\epsilon$, where m is the hydraulic radius term given by

$$m = \frac{\text{volume of fluid (free volume)}}{\text{wetted area}}$$

In the limit of the open tube, 4 m is equal to the tube diameter. For spherical particles in a cylindrical tube, it can be shown that

$$4m = \frac{D\epsilon}{3{\cdot}2\,(D/d_p)\,(1-\epsilon)+1}$$

where D = tube diameter,
ϵ = fraction voids,
d_p = particle diameter.

For the 3·2 mm spheres in a 2 in. tube with $\epsilon = 0{\cdot}379$, $4m = 1{\cdot}217$ mm.

Fig. 7 shows the results of this work compared with the results of previous workers. The coordinates for Fig. 7 were chosen such that the

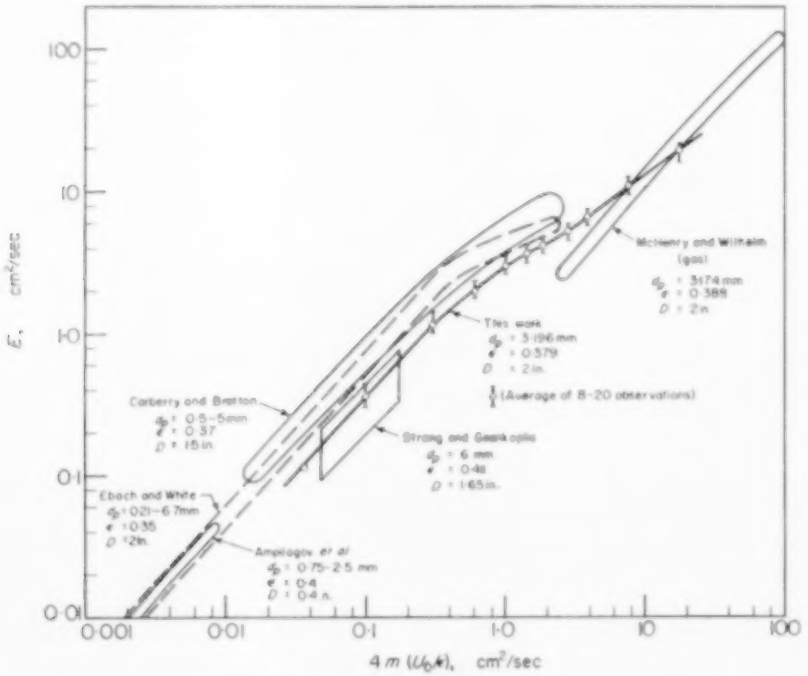

Fig. 7. Eddy diffusivity in packed beds (based on average velocity).

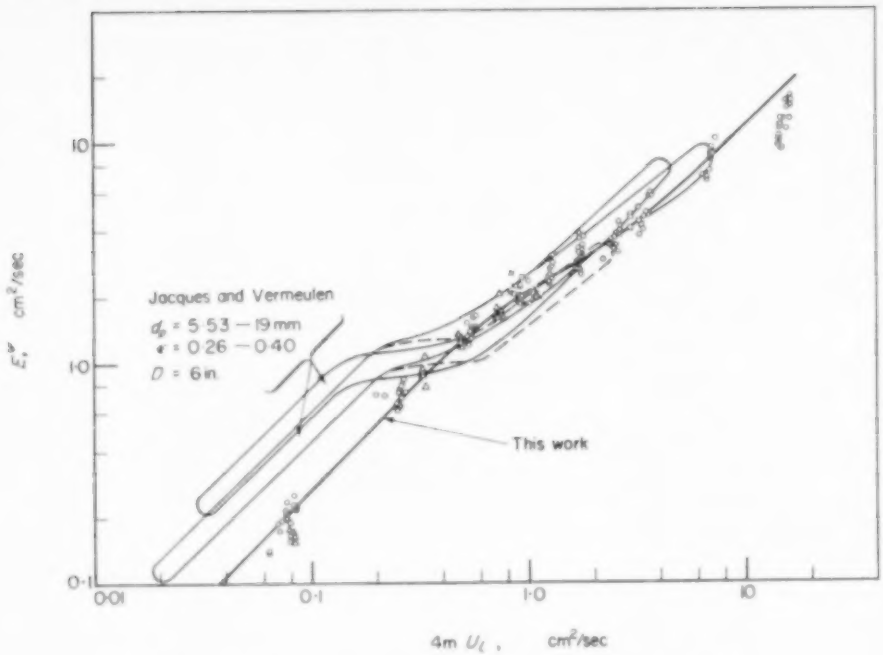

FIG. 8. Eddy diffusivity in packed beds (based on line velocity).

This work: ○ d_p = 3·196 mm ϵ = 0·0379 D = 2 in.
× d_p = 3·196 mm D = 4 in.
△ d_p = 1·311 mm D = 4 in.
□ d_p = 2·96 mm D = 4 in.

independent variables can be evaluated easily, not because they are believed to be the best for characterizing the mixing in packed beds. A knowledge of the velocity profile is not necessary in order to apply the results shown. The co-ordinates proposed as a result of the present work are E' versus $4\,mU_l$, where E' is calculated using the same equations as for E, but using U_l rather than U_0/ϵ as the characteristic velocity. The results of this work are shown on these co-ordinates in Fig. 8.

The more familiar curve using Pe as the ordinate is shown in Fig. 9. The abscissa, however, is not Re, since it has been shown that Pe does not depend on kinematic viscosity. The term $4\,mU_0/\epsilon$ has been chosen for the abscissa. Included on the plot for comparison purposes is Pe′, the prime designating the fact that U_l was used as the characteristic velocity, versus $4\,mU_l$.

Fig. 9 indicates that the present results lie above those of other workers. This general discrepancy may be explained in terms of the assumptions made by the various investigators, coupled with their experimental methods.

Some workers [2, 5, 8] used a dye tracer technique, coupled with a light transmittance technique whereby the light is transmitted across the whole tube cross section at a given Z level, which is devoid of packing. The pulse function of dye which was used in some work [2, 5] was injected into an unpacked section where flow not characteristic of the packed section prevailed. Entrance effects and non-flat velocity profile effects could be important in such an apparatus. Another pulse function method [5] was used in which the pulse was injected into the mainstream before it entered the expansion section leading to the packed test section. Here, entrance effects as well as non-flat velocity profile effects can influence the results. Even neglecting the

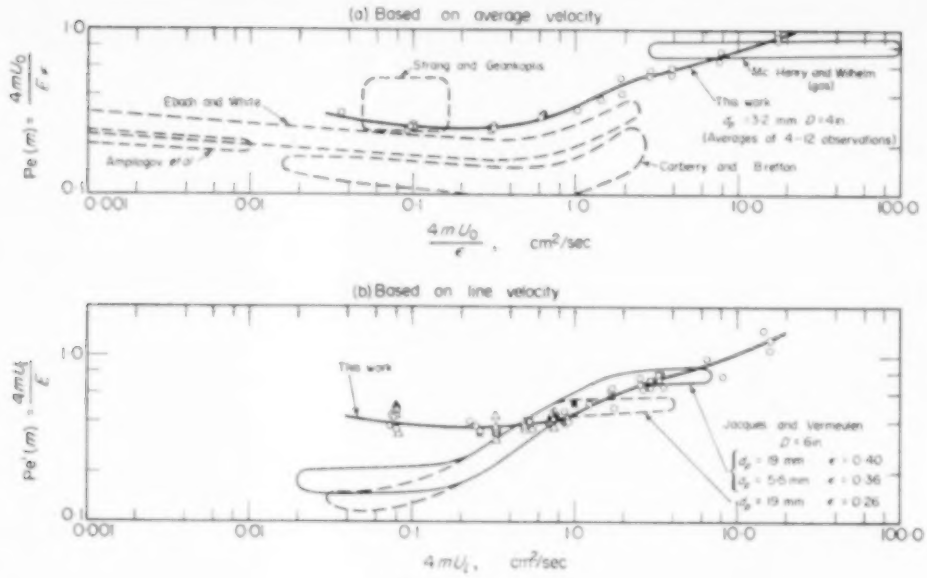

Fig. 9. Peclet number.

(b) This work: ○ $d_p = 3{\cdot}2$ $\epsilon = 0{\cdot}379$ $D = 2$ in. (averages of 4–12 observations)
× $d_p = 3{\cdot}2$ mm $D = 4$ in.
△ $d_p = 1{\cdot}3$ mm $D = 4$ in.
□ $d_p = 2{\cdot}96$ mm $D = 4$ in.

entrance effects, the non-flat velocity profile in the test sections can influence the results to a previously unsuspected extent.

An example using a step function input best serves to explain the inaccuracies encountered when the breakthrough curve is determined by averaging across the test section as is done with the light transmittance technique. For simplicity, it is assumed that half of the fluid is travelling at $U_l = 1{\cdot}1\ U_0/\epsilon$, and the other half at $U_l = 0{\cdot}9\ U_0/\epsilon$, giving an average velocity of U_0/ϵ. The fluid with the higher speed is near the wall as an annulus; the slower fluid forms a central core. Two observation points at some distance Z from the plane source are located such that one is near the centre, the other near the wall. Fig. 10 shows the two calculated breakthrough curves for a Pe of unity. Equation (3) was used for these calculations, with $N = 100$. The breakthrough curve closest to the origin corresponds to $U_l = 1{\cdot}1\ U_0/\epsilon$. The dotted curve is the average of the two curves which in essence is the method used in the light transmittance method, since the breakthrough curves are averaged across the tube before the Peclet number is calculated. Fig. 10 shows that the curve of the average of the two components has a slope at the $F = 1/2$ point which is less than the slope of either of the components. This average curve would by necessity yield a Peclet group which is misleadingly low. The Peclet group calculated from the resultant curve is 0·55, using $U_l = U_0/\epsilon$, resulting in an error of 45 per cent. The apparent mixing is "better" than the actual mixing due to the non-flat velocity profile. Even though the example given was for a step function injection the same error would hold true for the pulse function type of injection. Experiments such as the ones reported here are not sensitive to the flatness of the velocity profile.

Another set of investigators [13] assumed that a plane source was adequately approximated by seven point sources in a column which was 8 particle diameters in diameter. Calculations similar to those described for the injection system used in this work show that a distance of 5 particle

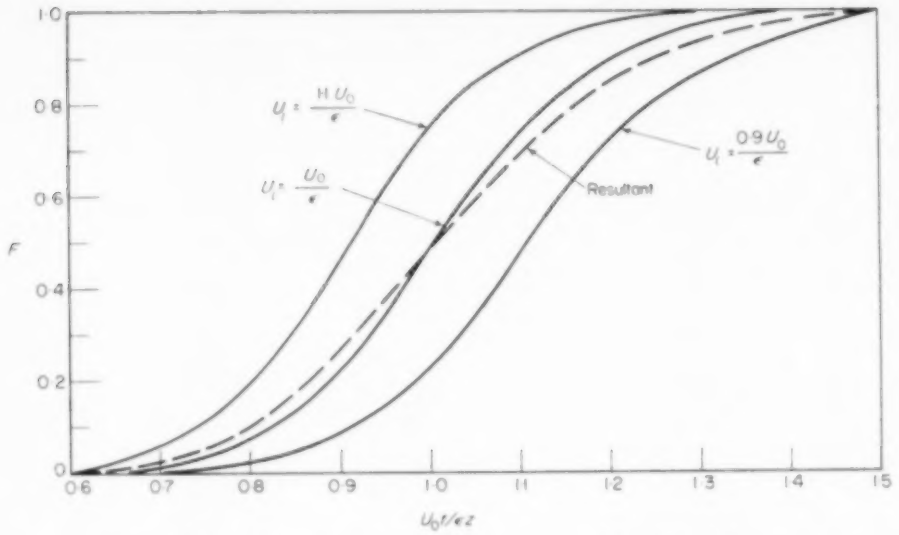

Fig. 10. Effect of non-flat velocity profile on averaged breakthrough curve.
Slope of resultant (dotted) curve = 2·09 ∴ Pe = 0·55 Actual Pe = 1·0 (45 per cent error).

diameters from the source was necessary before the "ripple" in the concentration contour map was 11 per cent taken along the diameter which contained the least ripple. The column was effectively only 25–35 particle diameters long, and hence about 20–25 per cent of the length of the column was subject to conditions which were not described by the boundary conditions assumed. Such a system would yield low results for the longitudinal Peclet number since the radial mixing from a point source creates apparent axial mixing, even in the absence of true longitudinal mixing. Hence, the observed resultant longitudinal mixing is higher than if a true plane source had been used.

From the above discussion it can be seen that the Peclet groups of all of the investigators cited would tend to be lower than the results for the Peclet group based on a true plane source and on point measurements of the break-through curve. Correspondingly, the results for the eddy diffusivity as reported by other investigators are higher than those reported here.

By reporting the eddy diffusivity as a function of the product of the hydraulic radius and the average velocity as in Fig. 7, the results of this investigation are somewhat high due to the use of the average velocity in the calculations; but they are not as high as those reported by others due to the fact that the break-through curve was not averaged across the tube as discussed above, but was observed at various points in the tube.

The presence of a non-flat velocity profile would be expected to have a negligible effect on the present results due to the fact that near the source, all of the injectant across the tube is travelling at a velocity equal to the average velocity. As the velocity of the tracer accommodates itself to the main-stream velocity profile, longitudinal diffusion is very rapidly taking place and reducing the longitudinal concentration gradient. At the same time, a radial concentration gradient which is expected to be small compared to the longitudinal gradient is being established. The radial eddy diffusivity is only 1/10th to 1/5th as large as the longitudinal eddy diffusivity, and hence mass transfer in the radial direction is much less than that in the axial direction.

Fig. 7 also shows that the results of McHenry and Wilhelm [7] for gaseous systems and the results of others for liquid systems follow one line whereas there is a wide divergence when

gas-phase and liquid-phase results are plotted against Reynolds number.

Summary and Conclusions

Liquid-phase longitudinal mixing in packed beds has been investigated by use of a salt tracer in such a manner that slightly non-flat velocity profiles have negligible effects on the results. The results have been presented in a form easy to use for routine calculations, as well as in a form considered to be more descriptive of the eddy diffusion type of mixing.

It is concluded that the longitudinal Peclet number is very sensitive to the method of investigation, and care should be exercised in the use of experimental results so that the type of "mixing" one wishes to describe is indicated by the value of the Peclet number which is selected. When radially integrated break-through curves are used non-flat velocity profiles can yield unexpectedly low results for the Peclet number.

Acknowledgements—The authors are grateful to Miss Helen Jaeger and Mr. R. L. Sani for aid in the calculations, to Mr. R. B. Waite for help in equipment design and construction, and to Mr. F. E. Vogelsberg for valuable advice and aid in the design and construction of the electronic apparatus. Thanks are due to the E. I. du Pont de Nemours Company for financial aid in the form of a research grant, and to the National Science Foundation for a pre-doctoral fellowship.

Appendix

1. *Derivative of equation* (2) *with respect to* (T/N)

$$\frac{\partial F}{\partial (T/N)} = N \frac{\exp\left[-(\sqrt{N} - \sqrt{T})^2\right]}{\exp(2\sqrt{NT})} I_0(2\sqrt{NT})$$

2. *Development of equation* (14)

From equation (13):

$$\frac{C}{C_\infty} = \left(\frac{L}{L_\infty}\right)^b$$

$$d\left(\frac{C}{C_\infty}\right) = d\left(\frac{L}{L_\infty}\right) = b\left(\frac{L}{L_\infty}\right)^{b-1} d\left(\frac{L}{L_\infty}\right) \qquad (17)$$

The slope of the recorder chart yields $\frac{d\,L/L_\infty}{dx}$, while the quantity desired is $\frac{d\,(C/C_\infty)}{dx}$. Therefore it is necessary to have $\frac{d\,(C/C_\infty)}{d\,(L/L_\infty)}$. From equation (17):

$$\frac{d\,(C/C_\infty)}{d\,(L/L_\infty)} = b\,(L/L_\infty)^{b-1} \qquad (18)$$

as given by equation (14). A plot of $b\,(1/2)^{b-1/b}$ versus temperature was used for calculational convenience.

3. *Development of equation* (16)

The slope on the recorder chart is $\frac{d\,(y/y_\infty)}{dx}$. It is necessary to find $dF/d\theta$.

Since $\theta = \frac{Ut}{Z}$,

$$d\theta = dt\left(\frac{U}{Z}\right) \qquad (19)$$

Also $dt = dx \cdot dt/dx$, (20)

But dx/dt = chart speed.

Combining equations (19) and (20):

$$\frac{dF}{d\theta} = \left(\frac{dF}{dx}\right)\left(\frac{dx}{dt}\right)\left(\frac{Z}{U}\right) \qquad (21)$$

From equations (18) and (15):

$$\frac{dF}{dx} = \frac{d\,(y/y_\infty)}{dx}\left[\frac{b}{1{\cdot}02}\left(\frac{L}{L_\infty}\right)^{b-1}\right] \qquad (22)$$

Combining equations (21) and (22):

$$\left(\frac{dF}{d\theta}\right)_{F=1/2} = \left\{\frac{d\,(y/y_\infty)}{dx}\left[\frac{b}{1{\cdot}02}\left(\frac{L}{L_\infty}\right)^{b-1}\right]\left(\frac{Z}{U}\right)\frac{dx}{dt}\right\}_{F=1/2} \qquad (23)$$

which yields equation (16) when introduced to equation (12).

4. *Determination of the point on the recorder chart which corresponds to* $F = 1/2$

Since $\frac{C}{C_\infty} = \left(\frac{L}{L_\infty}\right)^b = F$,

$$\left(\frac{1}{2}\right)^{1/b} = \left(\frac{L}{L_\infty}\right)_{F=1/2} = \left(\frac{y}{y_\infty}\right)_{F=1/2}$$

One merely measures $(1/2)^{1/b}$ of the distance between the two steady state values (before and after the step function) from the y_∞ value. This is the point at which $F = 1/2$. A plot of $(1/2)^{1/b}$ versus temperature was constructed.

5. *The general equation for* x *and* $dF/d\theta$

The asymptotic form of I_0 is: [18]

$$I_0(x) \frac{\exp(x)}{(\sqrt{2\pi x})}$$

It can be shown that

$$\frac{dF}{d\theta} = N \frac{\exp\left[-(\sqrt{N} - \sqrt{T})^2\right]}{\exp(2\sqrt{NT})} I_0(2\sqrt{NT}) \qquad (24)$$

Since $I_0(2\sqrt{NT}) \approx \dfrac{\exp(2\sqrt{NT})}{\sqrt{[4\pi\sqrt{NT}]}}$ (25)

than α is defined by

$$\alpha = \frac{I_0(2\sqrt{NT})}{\exp(2\sqrt{NT})} (2\sqrt{\pi})(\sqrt[4]{NT}) \qquad (26)$$

For large N and T, $\alpha \to 1{\cdot}0$.
Equation (24) becomes:

$$\frac{dF}{d\theta} = \left(\frac{N^3}{T}\right)^{1/4} \frac{\alpha}{2\sqrt{\pi}} \exp\left[-(\sqrt{N} - \sqrt{T})^2\right] \qquad (27)$$

Notation

a = constant in equation (13)
b = constant in equation (13)
C = concentration
d_p = packing particle diameter
E = eddy diffusivity based on average fluid velocity
E' = eddy diffusivity based on line velocity
$F = \int_0^T p(N, T)\, dT = \dfrac{C}{C_\infty}$
I_0 = Bessel function of zero order and first kind of an imaginary argument
L = conductance
m = hydraulic radius = $\dfrac{\text{volume of fluid}}{\text{wetted area}}$
N = dimensionless longitudinal position
p = probability density
Pe = Peclet group based on average fluid velocity $= U_0 d_p/\epsilon E$
Pe′ = Peclet group based on line velocity $U_l d_p/E'$
$\mathrm{Pe}_{(m)}$ = Peclet group based on hydraulic radius $= 4m\, U_0/E\epsilon$
t = time
T = dimensionless time
U = characteristic velocity
U_l = line velocity
U_0 = superficial velocity (based on empty tube area)
U_p = fluid velocity at a given point
V = voltages across Visicorder galvanometer
x = distance along time axis on the recorder chart
y = displacement of recorder trace from its no-signal position
z = dimensionless longitudinal position variable as in equation (1)
Z = longitudinal position with respect to tracer source

Greek Letters

α = correction factor for use of approximate mathematical form, defined in equation (11)
β = correction factor for determining $(\partial F/\partial\theta)_{\theta=1}$ from $(\partial F/\partial\theta)_{F=1/2}$ defined in equation (10)
$\Delta = \beta/\alpha$ = overall correction factor
ϵ = fraction voids
θ = dimensionless time $= T/N = Ut/Z$
ν = kinematic viscosity
μ = viscosity
ρ = density

References

[1] Amplogov I. E., Kharin A. N. and Kurochkina I. S. *Zh. fiz. Khim. SSSR* 1958 **32** 141.
[2] Carberry J. J. and Bretton R. H. *Amer. Inst. Chem. Engrs. J.* 1958 **4** 367.
[3] Danckwerts P. V. *Chem. Engng. Sci.* 1953 **2** 1.
[4] Deisler P. F. and Wilhelm R. H. *Industr. Engng. Chem.* 1953 **45** 1219.
[5] Erach E. A. and White R. R. *Amer. Inst. Chem. Engrs. J.* 1958 **4** 161.
[6] Kramers H. and Alberda G. *Chem. Engng. Sci.* 1953 **2** 173.
[7] McHenry K. W. and Wilhelm R. H. *Amer. Inst. Chem. Engrs. J.* 1957 **3** 83.
[8] Strang D. A. and Geankoplis C. J. *Industr. Engng. Chem.* 1958 **50** 1305.
[9] Aris R. and Amundson N. R. *Amer. Inst. Chem. Engrs. J.* 1957 **3** 280.
[10] Einstein H. A. Dissertation, Eidg. techn. Hochschule, Zürich 1937.
[11] Cairns E. J. Dissertation, University of California 1959.
[12] Klinkenberg A. R. *Industr. Engrs. Chem.* 1953 **45** 1202
[13] Marshall W. R. and Pigford R. L. *The Application of Differential Equations to Chemical Engineering Problems*, University of Delaware 1947.
[14] Cairns E. J. and Prausnitz J. M. Submitted to *Amer. Inst. Chem. Engrs. J.*

[15] Jacques G. L. and Vermeulen T. Univ. Calif. Rad. Lab. Report No. UCRL-8029 1958.
[16] Klinkenberg A. R. *Industr. Engng. Chem.* 1954 **46** 2285.
[17] Lapidus L. and Amundson N. R. *J. Phys. Chem.* 1952 **56** 984.
[18] Cairns E. J. and Prausnitz J. M. to *Industr. Engng. Chem. J.* 1959 **51** 1441.
[19] Schwartz C. E. and Smith J. M. *Industr. Engng. Chem.* 1953 **45** 1209.
[20] Wilhelm R. H. *Chem. Engng. Progr.* **49** 130.
[21] Klinkenberg A. R. and Stemitzer F. *Chem. Engng. Sci* 1956 **5** 258.
[22] Levenspiel O. and Smith W. K. *Chem. Engng. Sci.* 1957 **6** 227.
[23] Prausnitz J. M. *Amer. Inst. Chem. Engrs. J.* 1958 **4** 14M.
[24] Rifai M. E. Dissertation, University of California (Berkeley), 1956.
[25] Van der Laan E. Th. *Chem. Engng. Sci.* 1958 **7** 187.
[26] Von Rosenberg D. U. *Amer. Inst. Chem. Engrs. J.* 1956 **2** 55.
[27] Wehner J. F. and Wilhelm R. H. *Chem. Engng. Sci.* **8** 309.

Chemical Engineering Science, 1960, Vol. 12, pp. 35 to 50. Pergamon Press Ltd., London. Printed in Great Britain

Some aspects of liquid flow through fan spray nozzles

N. Dombrowski, D. Hasson* and D. E. Ward†

Department of Chemical Engineering, Imperial College, London

(*Received* 5 *August* 1959)

Abstract—The flow pattern of the liquid sheet produced from a rectangular-orifice fan spray nozzle is investigated with particular emphasis on the manner in which its thickness varies from the orifice to the point of breakdown. The trajectory of its boundaries is analysed on the basis of a simple theory.

The results of the study can be summarized as follows:

(a) The streamlines of the spray sheet are straight and unaffected by the curved boundary. The liquid velocity along a streamline is constant, everywhere in the sheet and independent of its viscosity.

(b) The thickness of the sheet is at any point inversely proportional to its distance from the orifice, and can be expressed, for a given set of operating conditions, by a thickness parameter.

(c) At relatively low injection pressures, the thickness parameter for a given nozzle and liquid of low viscosity is found by experiment to be a function of surface tension and a function of $(P\rho)^{1/2}/\eta$ where P = injection pressure, ρ = density, η = viscosity. At the high injection pressures the thickness parameter is only a function of $(P\rho)^{1/2}/\eta$.

(d) The trajectory of the sheet is a function of the injection pressure, sheet thickness and surface tension, and independent of liquid density.

Résumé—Le diagramme d'écoulement d'une nappe liquide issue d'un gicleur à orifice rectangulaire est examiné en mettant spécialement l'accent sur la variation de son épaisseur depuis l'orifice jusqu'au point de contraction. La trajectoire de ses limites est analysée sur la base d'une théorie simple.

Les résultats de cette étude peuvent être résumée ainsi:

(a) Les lignes d'écoulement de la nappe pulvérisée sont droites et ne sont pas affectées par la limite incurvée. La vitesse du liquide le long d'une ligne d'écoulement est constante partout dans la cappe et est indépendante de sa viscosité.

(b) L'épaisseur de la nappe est a un point quelconque inversement proportionnelle à sa distance de l'orifice, et peut-être exprimée, pour une série donnée de conditions de fonctionnement, par un paramètre quelconque.

(c) L'expérience a montré que pour des pression d'injection relativement basses, la paramètre d'épaisseur pour une tuyère donnée et un liquide de faible viscosite é est une fonction de la tension superficielle et une fonction de $(P\rho)^{1/2}/\eta$, ou P = Pression d'injection, ρ = densité, η = viscosité. A de hautes pressions d'injections, la paramètre d'épaisseur est seulement une fonction de $(P)^{1/2}/\eta$.

(d) La trajectoire de la nappe est une fonction de la pression d'injection, de l'épaisseur de la nappe et de la tension superficielle, elle est indépendante de la densité du liquide.

Zusammenfassung—Das Fliessverhalten der Flüssigkeitslamelle, die durch die rechtechikge Öffnung einer Gebläsesprühdüse entsteht, wird untersucht. Besonderer Wert wird auf die Feststellung der Dickenänderung von der Öffnung bis zum Auflösungspunkt gelegt. Der Bahnverlauf der Lamellengrenzen wird auf Grund einer einfachen Theorie analysiert. Die Untersuchungsergebnisse können wie folgt zusammengefasst werden:

*Now at the Technion, Haifa, Israel.

†Now at British Oxygen Engineering Co. Ltd., Edmonton, London.

(a) Die Stromlinien der Flüssigkeitslamelle sind gerade und werden durch die gekrümmte Begrenzung nicht beeinflusst. Die Strömungsgeschwindigkeit entlang einer Strömlinie ist konstant, überall in der Lamelle und unabhängig von ihrer Viskosität.

(b) Die Dicke der Lamelle ist an jedem Punkt umgekehrt proportional zur Entfernung von der Öffnung und kann für eine gegebene Zahl von Betriebsbedingungen durch einen Dicken-Parameter dargestellt werden.

(c) Bei relativ niedrigen Spritzdrucken zeigt das Experiment, dass der Dicken-Parameter für eine bestimmte Düse und eine Flüssigkeit niedriger Viskosität eine Funktion der Oberflächenspannung und eine Funktion von $(P\rho)^{1/2}/\eta$ ist ; P = Spritzdrock, ρ = Dichte, η = Viskosität. Bei hohen Spritzdrucken ist der Dicken-Parameter nur eine Funktion von $(P\rho^{1/2})\eta$.

(d) Der Bahnverlauf der Lamelle ist eine Funktion des Spritzdruckes, der Lamellendicke und der Oberflächenspannung ; er ist unabhängig von der Flüssigkeitsdichte.

Introduction

The performance of spray nozzles has received intensive study during the last decade because of their increasing use in combustion [1], chemical [2] and agricultural [3] engineering. In most applications, the function of the nozzle is to disintegrate a liquid stream in order to create a large surface per unit volume, and to distribute with control the resulting drops uniformly in space. In order to obtain a greater understanding of the processes involved, work has been directed towards analysing the hydrodynamics of flow through a wide variety of atomizers, establishing the basic mechanisms of drop formation, and determining the resulting drop-size distribution. In recent years, particular attention has been paid to the atomization of flat spray sheets [4–12] because of their simplicity and because they provide a convenient model for both experimental and theoretical study. These sheets can be produced in a number of ways by the impingement of liquid streams or by their impact on a solid stationary or rotating surface. A simple method is to use the fan nozzle, a device which enables the properties and dimensions of the sheet to be easily controlled by varying the approach passages to the nozzle orifice.

While the factors governing sheet instability and disintegration have received increasing attention, very little is known about the manner in which the sheet is formed at the orifice or about its physical dimensions.

The present paper describes the principal flow characteristics of fan spray sheets prior to the onset of instability and disintegration. Interferometry is employed to record the variation of thickness throughout the sheet, and a simple analysis, is presented to account for the trajectory of the free edges of the sheet.

The Mode of Formation of a Fan Spray Sheet

The principal methods of forming thin sheets in a wide range of atomizers have been discussed by Dombrowski and Fraser [6]. In the fan spray nozzle, two streams of liquid are made to impinge behind an orifice by specially designed approach passages and a sheet is formed in a plane perpendicular to the plane of the streams. The principal is illustrated in Fig. 1 (a) which shows liquid flowing through a rectangular orifice formed at the end of a rectangular tube. Under these conditions the flow through the orifice is constricted in only one plane and the streamlines converge to form a region of pressure behind the orifice. A flat sheet is produced as the liquid freely spreads through the orifice limited only by the side walls. The spreading angle of the sheet can further be increased by extending the opening to the sides of the orifice, (Fig. 1b). Fig. 1 (c) shows a commercial nozzle, designed on this principle, which has been used in the present work. It is made of porcelain and contains a rectangular orifice which is produced by the interpenetration of two rectangular slots.

In the absence of surface tension, the edges of the sheet would travel in straight lines from the orifice so that a sector of a circle would be formed. However, as a result of surface tension, the edges contract and a curved boundary is produced as the sheet develops beyond the orifice. A typical flash photograph of a low viscosity fan spray is illustrated in Fig. 2 (a). It shows that as the

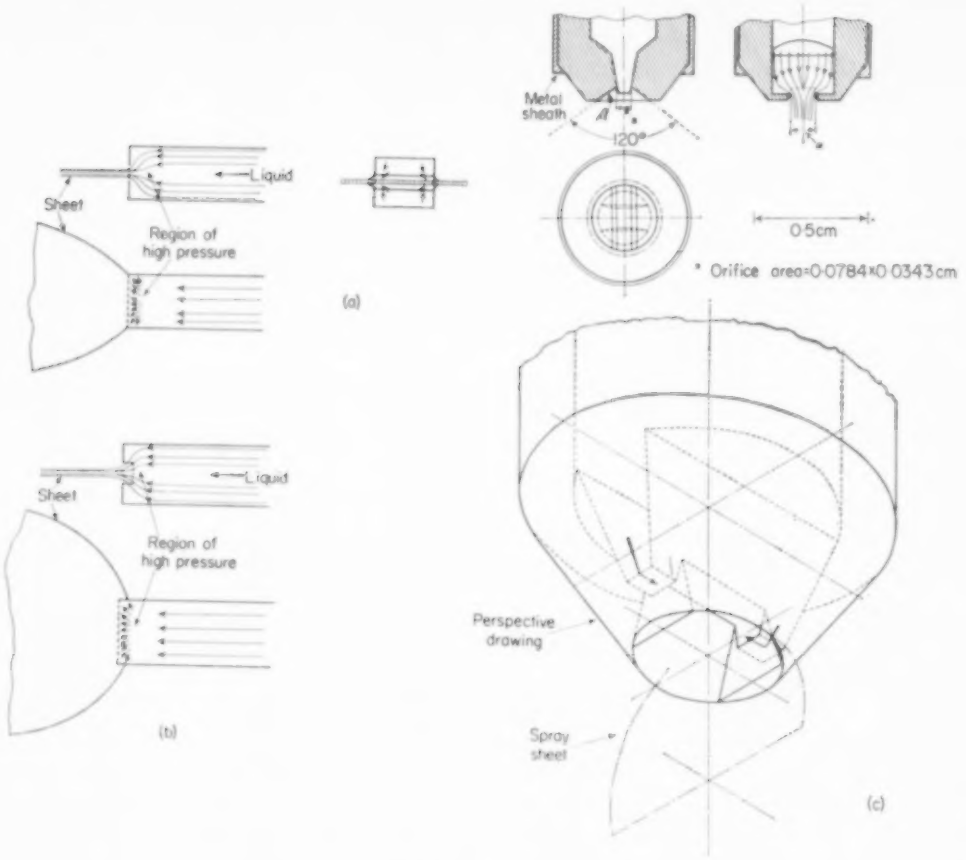

FIG. 1. Mechanism of flow through fan spray nozzles.

liquid in each edge moves along the curved boundary, the latter becomes disturbed and disintegrates in a manner somewhat analogous to a jet of liquid [17]. When this occurs, the resulting drops sustain the direction of flow of the edge at the point at which the drops are formed, and remain attached to the receding surface by thin threads which rapidly disintegrate into streams of drops. Corresponding further to the characteristics of jets, the breakdown of the edges is restrained by high viscosity. At higher injection velocities (Fig. 2b), the contraction is less pronounced, and the placid sheet eventually becomes ruffled and disintegrates before the two edges coalesce.

Analysis of flow in sheet

In order to examine the nature of the fluid streamlines, photographs have been taken of spray sheets containing suspended aluminium particles. Fig. 3 demonstrates the direction of flow of liquid within the sheet and as it passes through the edges into the ambient atmosphere. It was obtained by taking a photograph with a flash of approximately 1 msec duration so that each aluminium particle traces its own path. Three points of interest can be observed in this photograph. First, the sheet streamlines are straight and unaffected by the curved boundary. Secondly, the drops leave the edges tangentially at an angle different from that of the streak, and thirdly,

many of the drops at the base of the sheet cross over from one side to another.

The velocity distribution along each streamline has been determined by taking two microsecond-flash photographs separated by a short and known interval of time on the same plate [18]. The movement of each aluminium particle thus provides a measure of the local liquid velocity. Measurements from photographs, such as Fig. 4, of various sprays injected at atmospheric and sub-atmospheric air densities, have shown that the distance travelled on the sheet by individual particles in unit time is constant, its value being independent of either viscosity (up to 70 cP) or of the ambient atmosphere. Comparison between the velocity of the sheet as represented by the tracer particles and as measured directly by the movement of the centres of perforations appearing on a sheet sprayed *in vacuo* (Fig. 4), or when soluble oil is added to water [6], showed no measurable difference. Thus, it may be concluded from these results that the stream velocity is constant along the sheet, its absolute value depending only on the differential injection pressure.

It has been previously assumed [19, 20, 21] that when a spray sheet develops, the increase in surface energy occurs at the expense of its kinetic energy. Experimental evidence suggesting this magnitude of velocity reduction has been obtained by Weinberg [22] for the conical sheets produced from swirl spray nozzles. His findings cannot however be accepted without reservation since his results indicate that the diameter of the total head tube employed for measuring local velocities was larger than the thickness of the sheets at the leading edge and thus was not fully immersed in the liquid.

In order to clarify this point further, a high speed cine-film was made of the liquid sheet issuing from a swirl spray nozzle. Measurements made of the movement of local irregularities and waves confirm the above conclusions that contrary to previous assumptions, the stream velocity is in fact constant throughout the length of the sheet.

This finding is easily explained since no external force acts on the sheet and the flow through each liquid streamline must satisfy the equation of conservation of momentum. The application of this result to the equation of conservation of energy further predicts that the energy absorbed in producing the larger surface area is derived from the enthalpy of the liquid. However, this cannot be easily confirmed since the predicted temperature drop along the sheet, calculated on this basis is too small for accurate measurement. The general form of the energy equation of a flowing fluid may be formulated as [23].

$$dq - dW = dH + d(mgz) + d(1/2\, m V^2) \qquad (1)$$

where q = net heat absorbed from the surroundings.

W = net work done by the fluid on the surroundings.

mgz = potential energy of mass m of fluid at height z above datum level.

$1/2\, m V^2$ = kinetic energy of the fluid.

H = total enthalpy of the liquid of mass m which is here defined as including the total surface energy.

For a liquid sheet ejected from a orifice the equation may be simplified as follows. Since there is no change of velocity and assuming that no energy is transferred to the atmosphere, $d(1/2\, m V^2) = 0$ and $dW = 0$. Furthermore, it can be shown that the potential energy change is negligible compared to the surface energy change so that $d(mgz) = 0$. If it is further assumed that the flow is adiabatic, $dq = 0$.

Hence

$$dH = 0$$

Since the flow is incompressible at constant pressure

$$dH = dU = 0 \qquad (2)$$

where U is the total internal energy of the liquid mass m, defined as including the total surface energy of the liquid.

Now U may be expressed in the following form [24]

$$U = E + A\,\gamma - T\frac{d\gamma}{dT} \qquad (3)$$

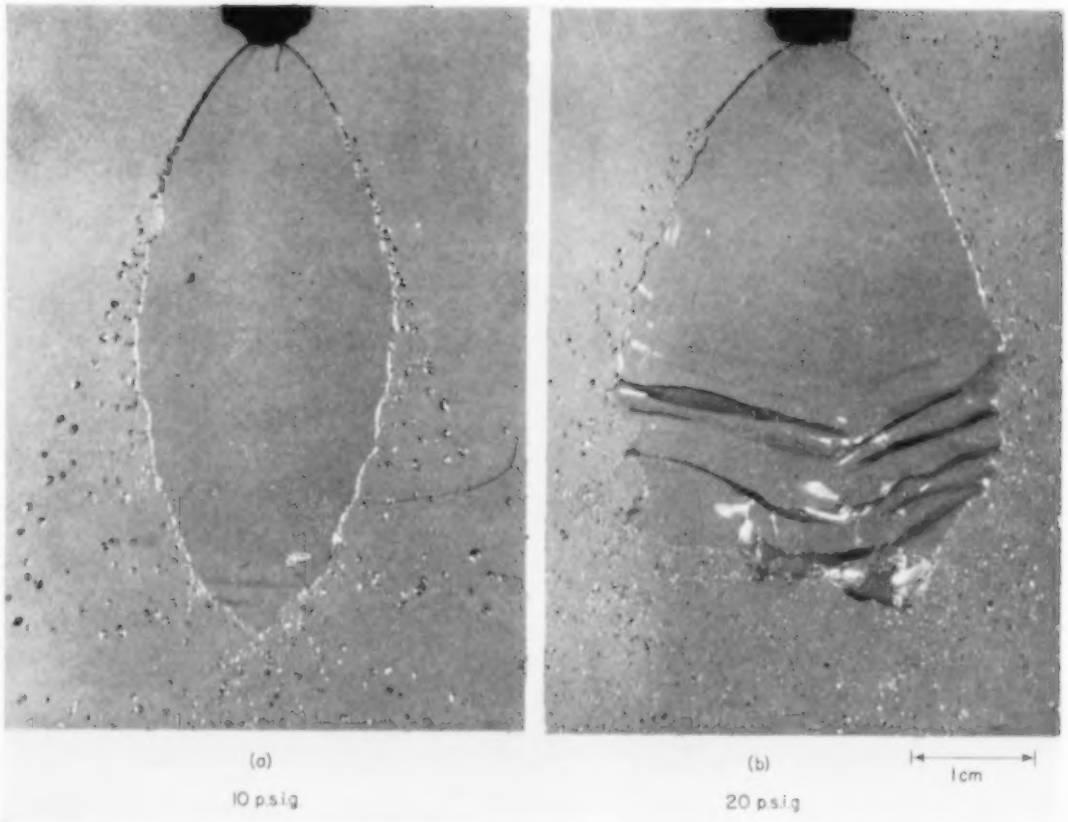

FIG. 2. Microsecond-flash photographs of spray sheets of water (55 °C) issuing from a fan spray nozzle.

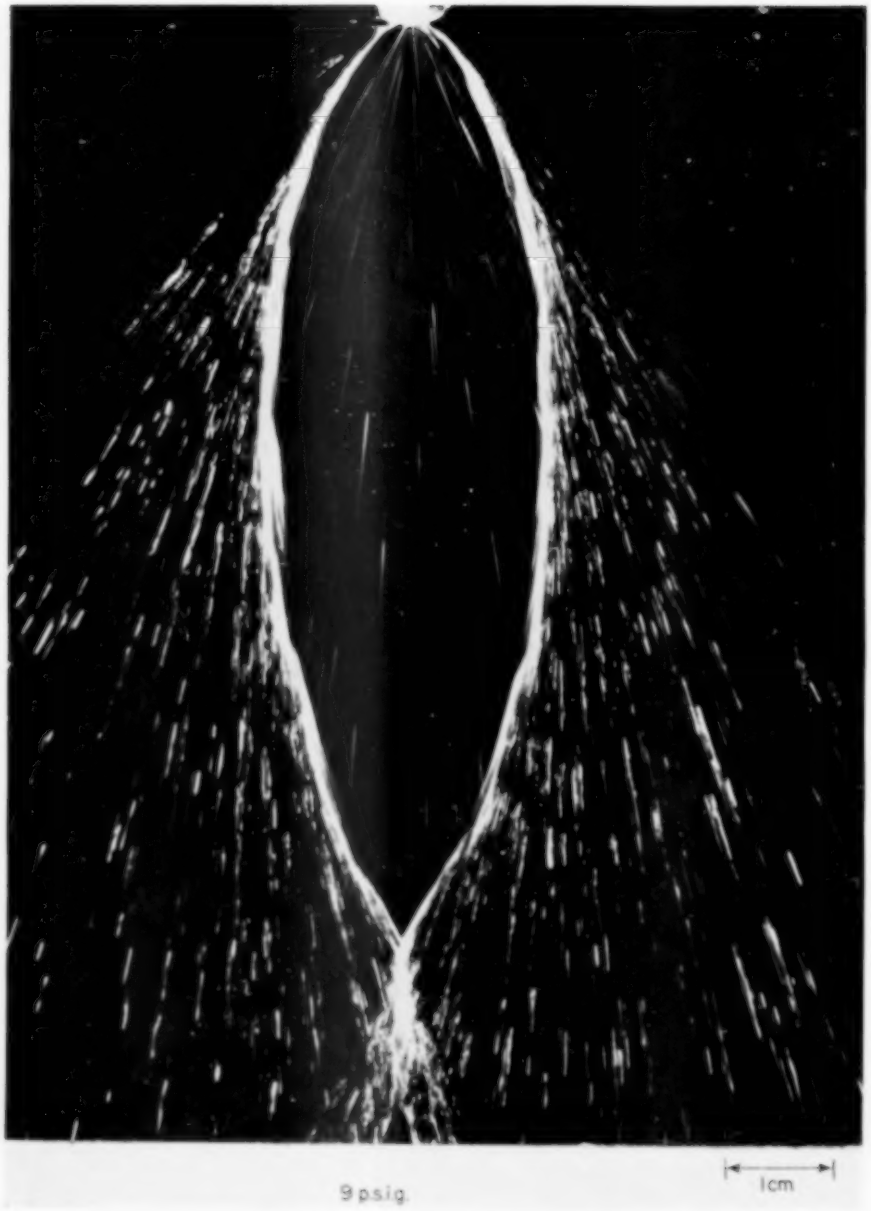

FIG. 3. Streamlines in fan spray sheet of water. (Exposure time, 1 msec).

FIG. 4. Double-flash photograph of 1 per cent aluminium particle suspension sprayed *in vacuo*.

Where E = internal energy of the liquid when its surface area $A = 0$.
γ = the free surface energy per unit area, or surface tension per unit length,
T = absolute temperature,
and the expression $\left(\gamma - T\frac{d\gamma}{dT}\right)$ is the total surface energy of the liquid per unit area.

Over moderate temperature changes, the surface tension decreases linearly with increasing temperature according to the relation

$$\gamma = a - bT$$

where a and b are constants.

Hence

$$\gamma - T\frac{d\gamma}{dT} = a = \text{constant}$$

Thus from equations (2) and (3),

$$dE = -a\,dA$$

The change in internal energy can also be expressed as

$$dE = m\,c\,dT$$

where c is the specific heat of the liquid.

Therefore

$$m\,c\,dT = -a\,dA$$

i.e. the temperature drop along the sheet is given by

$$\Delta T = \frac{a\,A}{m\,c}$$

since the liquid mass issuing from the orifice has a negligible surface area.

Now the increase of liquid surface per unit mass along any element is given by

$$\frac{A}{m} = \frac{2}{\rho S}$$

where S is the thickness of the sheet and ρ is the liquid density.

Therefore

$$\Delta T = \frac{2a}{\rho S} \qquad (4)$$

From measurements of sheet thickness made by Straus [4], a particular nozzle spraying water at 20 p.s.i.g. produces a sheet which is $5{\cdot}3 \times 10^{-4}$ cm thick at a distance of 3 cm from the orifice. At room temperature the value of the constant 'a' for water is equal to 115·38 [24]. Equation (4) predicts a reduction of sheet temperature of 0·01 °C.

Although the converging streamlines in the nozzle cause a *region* of high pressure to be formed behind the orifice, it will be assumed for the following analysis that the liquid flows from the nozzle as if there were a *line source* of high pressure perpendicular to the sheet. Furthermore, it will be assumed that the contraction of the edges by surface tension does not affect the flow pattern of the sheet, i.e. the liquid corresponding to the "vanished" part of the sheet lying between the theoretical linear and actual curved boundaries is concentrated at the curved boundary. A diagram of this simplified flow pattern is shown in Fig. 5.

Consider an element of the sheet, of length dx, subtending an angle $d\beta$ at the orifice, and at a distance x from the centre of pressure P.

If V = liquid velocity,
and S = the thickness of the sheet,

then dQ, the volume of liquid flowing through the element $d\beta$ in unit time is given by

$$dQ = x.d\beta.S.V.$$

$$\therefore S = \frac{dQ}{d\beta}\frac{1}{xV}$$

Since the liquid streamlines are straight, and the stream velocity is constant throughout the sheet, $dQ/d\beta$ and V are constant, and thus

$$S = \frac{K}{x}, \qquad (5)$$

where K is a dimensional constant which uniquely represents the variation of sheet thickness with distance from the nozzle.

Because the sheet edge is curved by surface tension, fan spray sheets cannot be characterized by a spray angle. However, $2\theta_T$, the sheet angle at the orifice, before it is affected by the exit passage or surface tension, can be derived in terms of the thickness parameter K.

The actual area of flow is represented by the

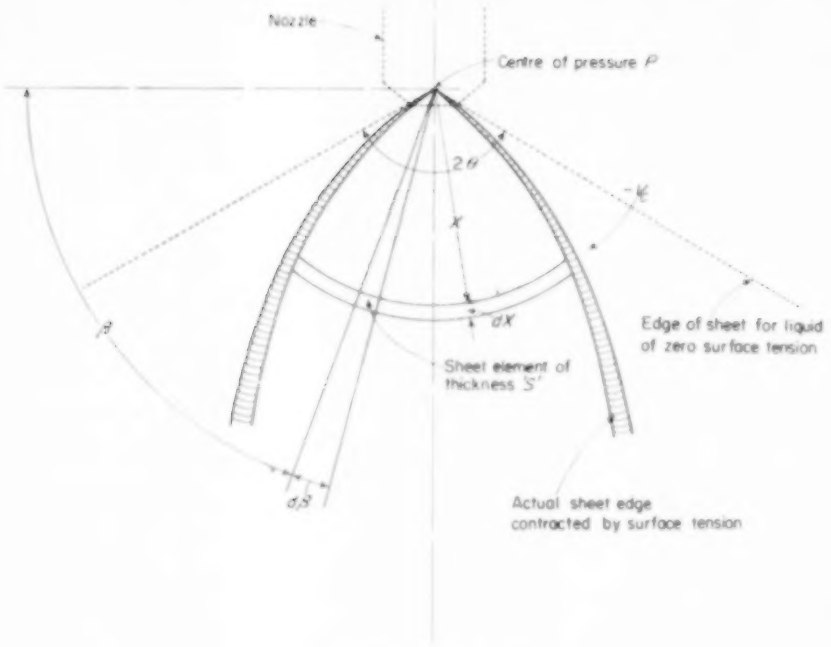

Fig. 5. Flow pattern in sheet.

curve area $ABJCDI$ of radius x_0 in Fig. 6. From equation (5)

$$K = AB.x_0 = \frac{AB.AD}{2\sin\theta_T} = \frac{\text{Orifice area}}{2\sin\theta_T}$$

$$\therefore \theta_T = \sin^{-1}\frac{[\text{orifice area}]}{2K} \qquad (6)$$

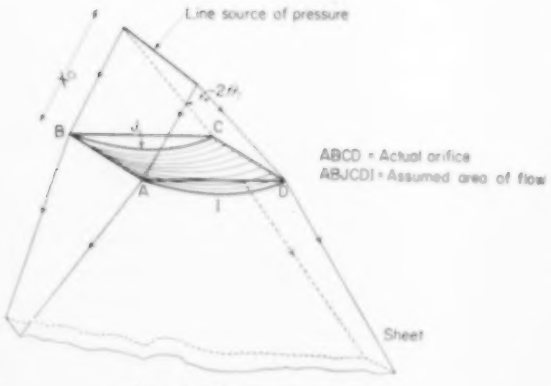

Fig. 6. Flow pattern in orifice.

Traejctory of the sheet edge

The spray pattern of a fan spray depends, among other things on two factors, the disintegration of the leading segment of the sheet (Fig. 2b), and the disintegration of the edges of the sheet (Fig. 2a). The former is predominant at most injection pressures used in practice where a high relative velocity exists between the liquid and ambient atmosphere. The latter becomes important at low relative velocities. Furthermore, it will be shown in a later section that at low injection pressures the flow of liquid in the sheet appears to be influenced by the contraction of the edges as a result of surface tension. A knowledge of the factors influencing the trajectory of the sheet edges should help towards an understanding of both the mechanism of disintegration and the flow changes to which the contraction might give rise.

An approximate expression for the trajectory can be derived for inviscid flow in the following manner.

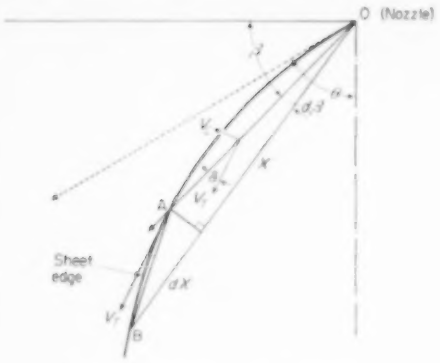

FIG. 7. Trajectory of sheet edge.

VOL. 12 1960

In Fig. 7, O is the origin of the sheet, θ is the angle at which the sheet edges first issue from the orifice, x the distance of a point A on the edge from O, and $x + dx$, its position after a small interval of time dt. The chord AB is taken as the tangent at A since dx is very small. Now let a particle of liquid move along the line OA with radial velocity V. This velocity can be resolved into two components, one V_T, tangential to the sheet edge at point A, at an angle δ to V, and the other V_c, normal to V_T.

Thus

$$V_c = V \sin \delta \tag{7}$$

When the particle reaches point A, it changes direction along the tangent. The rate of change of momentum $\rho S V_c^2 \cdot V_c$ per unit length is equal to the surface tension force at the free edge 2γ per unit length.

$$\text{i.e.} \quad 2\gamma = \rho S V_c^2$$

or since

$$S = K/x \text{ (equation 5)}$$

$$V_c = \left[\frac{2\gamma x}{\rho K}\right]^{1/2} \tag{8}$$

The radial velocity V, can be expressed as $C_v\sqrt{2gP/\rho}$ where P is the differential injection pressure and C_v is the coefficient of velocity.

Measurements made from double-flash photographs of aluminium particle suspensions show that the velocity coefficient of the orifice is approximately equal to its discharge coefficient. Thus, the area coefficient is equal to unity, and equation (8) can be rewritten as

$$\left[\frac{2\gamma x}{\rho K}\right]^{1/2} = C_Q \left[\frac{2gP}{\rho}\right]^{1/2} \sin \delta \tag{9}$$

Now $\sin \delta = \dfrac{x\, d\beta}{[(dx)^2 + x^2 (d\beta)^2]^{1/2}}$

which on substituting in equation (9) and integrating gives

$$x = \frac{g.P.K.C_Q^2}{2\gamma}\left[1 - \sin(\beta + \theta)\right] \tag{10}$$

for boundary conditions where $\beta = \pi/2 - \theta$, when $x \to 0$.

From this simple analysis of the flow it can be seen that θ_T, the sheet angle at the orifice, and the trajectory of the sheet edge may be predicted from a knowledge of the sheet thickness as expressed in terms of K.

Method of Measuring the Thickness of Thin Films of Liquid

Thicknesses of spray sheets have been measured previously by Straus [4] and Dombrowski and Fraser [6] over a limited range of conditions. They measured the volume of liquid passing through a small section of the sheet and calculated the thickness by assuming that the sheet velocity could be expressed by $C_Q[2gP/\rho]^{1/2}$. This is a simple method, but suffers from the disadvantages that the insertion of the flow measuring device disturbs the sheet, that the liquid velocity must be assumed, and that the direction of flow must be known for taking a representative sample. A number of indirect methods have also been employed.

Dixon *et al.* [12] and Straus [4] measured the variation of light absorption through dyed liquid sheets. Dukler and Bergelin [7] employed an electrical capacitance method for measuring the thickness of thin liquid films flowing down glass tubes. Berthold [14] has patented a method of measuring the thickness of thin sheets of materials using the absorption of β-rays. These methods suffer from their inability to detect the small changes of thickness which occur in a fan spray sheet, they may require complex equipment and they necessitate a large number of measurements to obtain the thickness over the entire sheet.

Since it has been shown [6] that smooth sheets can be obtained from spray nozzles of the type shown in Fig. 1 (*c*), it is also possible to use an interferometric method, and one such technique has been developed. This had the advantage that the thickness variations over the entire sheet

area could be obtained from a single photographic record. Comparisons between the volumetric and interferometric techniques have shown good agreement, if, in the former techniques the coefficient of velocity is assumed to be equal to the coefficient of discharge.

Application of light interference to the measurement of sheet thickness

When a monochromatic light beam is allowed to fall on a thin film, reflection takes place from the front and back surfaces, (Fig. 8). These reflections interfere with each other because of the difference in their light paths, and it can be shown that the optical path difference D is given by

$$D = 2S\,\mu \cos \alpha \tag{11}$$

where μ = refractive index,
and α = angle of refraction of the light beam in the film.

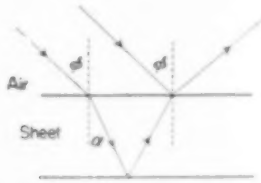

Fig. 8. Interference of light rays in a thin sheet.

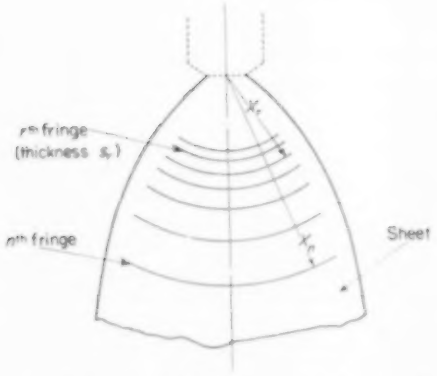

Fig. 9. Pattern of interference fringes on sheet.

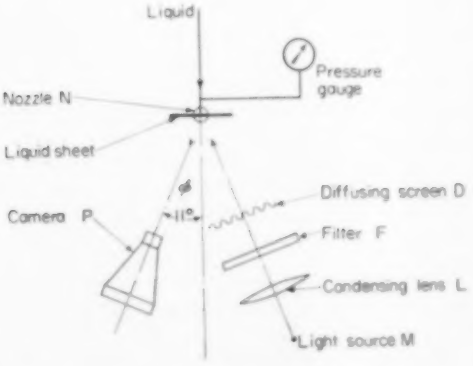

Fig. 10. Apparatus.

If D is an odd number of half wavelengths, the two reflected beams reinforce each other and a bright fringe occurs. Thus from equation (11), the change in thickness ΔS between two adjacent bright fringes is given by:

$$\Delta S = \frac{\lambda}{2\mu \cos \alpha} \tag{12}$$

where λ is the wavelength.

The variation in sheet thickness from a fan spray nozzle could thus be determined by measuring the thickness of the sheet in the orifice, i.e. the width of the orifice, and the distance of each fringe from it. However equation (5) shows tha tnear the orifice, dS/dx is very large, so that adjacent fringes will be very close to each other and difficult to resolve. This difficulty can be circumvented in the following manner.

In Fig. 9 let the thickness at the rth fringe, (the first clearly resolvable fringe) be S_r at a distance x_r from the orifice and let the subscript n denote any subsequent fringe.

Thus from equation (5)

$$S_r = K/x_r$$

and

$$S_n = K/x_n$$

and therefore $S_r - S_n = K\,(1/x_r - 1/x_r)$

From equation (12)

$$S_r - S_n = (n - r)\,\frac{\lambda}{2\,\mu \cos \alpha}$$

$$\text{Therefore } \frac{1}{x_n} = -\frac{\lambda\,(n - r)}{2K\,\mu \cos \alpha} + \frac{1}{x_r} \tag{13}$$

A linear relationship should thus exist between $(n - r)$ and $1/x_n$. If the slope of the straight line is given by m, then

$$K = -\frac{\lambda}{2m\,\mu \cos \alpha}.$$

Now $\sin \alpha = \sin \phi/\mu$ where ϕ is the angle of incidence. Thus the expression may be rewritten as

$$K = -\frac{\lambda}{2m\,\mu\,(1 - \sin^2 \phi/\mu^2)^{1/2}} \tag{14}$$

Experimental technique for measuring sheet thickness

The apparatus employed to record the fringe patterns is shown in Fig. 10. The light source, M, is a 250 W compact-source mercury vapour lamp, whose light is condensed

by lens L, and transmitted through a mercury yellow filter F and diffusing screen D, onto the liquid sheet. The reflected light is photographed by the camera P. Liquid is fed to the nozzle N (seen from above) by compressed air. Its pressure is measured by a Bourdon gauge and its temperature by a mercury thermometer. The refractive indices of the liquids have been measured by a refractometer. The light consists of the two yellow lines of wavelengths 5770 and 5790 Å, and the mean value 5783 Å has been used for calculations.

Equation (14) shows that the value of K depends on the value of $\sin^2\phi$. The error in determining ϕ can be reduced to a minimum by maintaining it at a small value. ϕ can be made zero by employing transmitted fringes but because these are produced by a double reflection, they have a very low contrast and cannot be satisfactorily photographed. Reflected light is therefore used and ϕ is kept to a minimum by placing the camera and light source as close together as possible. Under these conditions the value of ϕ is 11°. This is considered satisfactory since an error of $\pm 3°$ only causes an error of $\pm 0{\cdot}6$ per cent in value of K. The camera is aligned at the correct angle by a simple parallax method.

Because the plane of the sheet is disturbed by waves, relatively long exposures are required to ensure that light is reflected into the camera from every part of the sheet as the latter moves past the lens. On the other hand the exposure has to be kept to a minimum in order to reduce external vibrations. The best compromise is found by illuminating the sheet for 1/50 sec and employing Ilford Rapid Process Pan emulsion.

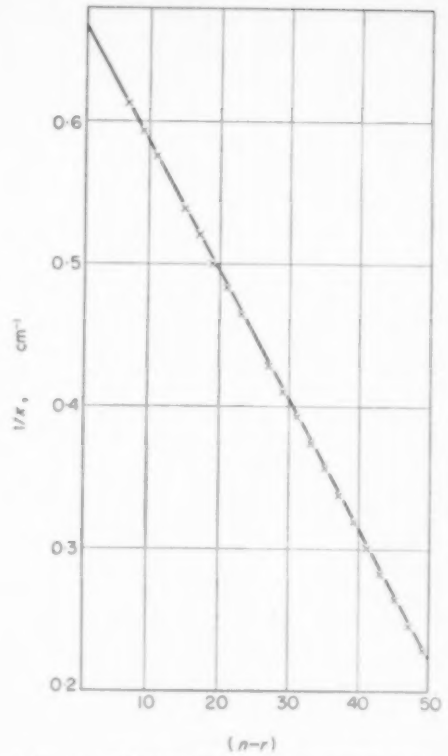

FIG. 11. Relation between $(n - r)$ and $1/x_n$.

EXPERIMENTAL RESULTS

The thickness parameter K has been measured for one nozzle (Fig. 1c) over a wide range of liquid surface tensions, viscosities, and injection pressures. Two levels of approximately constant surface tension, 30 and 73 dyn/cm were studied by using kerosene–paraffin and water–glycerol mixtures respectively. Viscosities were varied from 1 to 50 cP and injection pressures up to 50 p.s.i.g. A few determinations were also made with ethyl alcohol, benzaldehyde and ethyl acetate.

Typical interferograms are presented in Figs. 13, 22 and 23. Fig. 11 gives a typical plot of $(n - r)$ vs $1/x_n$ and shows an excellent linear correlation as predicted by equation (13).

Irregularities in the nozzle orifice caused the value of K to vary with different streamlines (see Plates 23, 24) so that a mean value has been calculated for the core of the sheet over a total angle of 45° round the nozzle axis.

This work has confirmed previous findings [7] that the coefficient of discharge of a fan spray nozzle is independent of surface tension or viscosity. In the present case it has a value of 0·91.

Effect of injection pressure on the thickness parameter K

Fig. 12 shows K as a function of injection

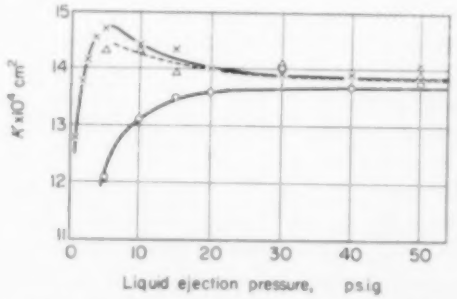

FIG. 12. The effect of pressure on the thickness parameter K.

pressure for values of viscosity below 2 cP and indicates that it tends asymptotically to a constant value of approximately 14×10^{-4} cm² with increase of liquid pressure. Thus, this nozzle produces a sheet which is less than 5 μ thick at a distance of 3 cm from the orifice.

Certain differences can be observed between water, the liquid of high surface tension, (73 dyn/cm) and kerosene and alcohol, the liquids of low surface tension (25 and 23 dyn/cm). The curve for water shows that as the injection pressure is raised, K steadily increases to an asymptotic value. However, with kerosene, K rises rapidly to a maximum of $14{\cdot}7 \times 10^{-4}$ cm² at 5 p.s.i.g. after which a steady decline takes place towards the asymptote. The behaviour of alcohol appears to be similar to that of kerosene although the lower injection pressures were not examined.

Liquids of higher viscosity were only examined between an injection pressure range of 15–50 p.s.i.g. It was found that the value of K tended to diminish slowly with increase of pressure. Fig. 13 shows a typical photograph and demonstrates that the flow disturbances apparent at low viscosities (Figs. 22 and 23) are damped out.

Effect of surface tension and viscosity on the thickness parameter K

Fig. 14 shows the effect of viscosity (1–50 cP) at two surface tension levels of 25 and 70 dyn/cm and at injection pressures of 15, 30 and 50 p.s.i.g. respectively.

Each curve is plotted for data pertaining to two levels of surface tension, and the uniform scatter of the points around their respective curves clearly shows that within the limits of experimental error there is no effect of surface tension. This result is to be expected. Surface tension should not affect the flow behind the orifice which can be considered to be the main factor influencing the sheet thickness.

However, the value of K is markedly affected by viscosity, and Fig. 14 shows that it increases with increase of viscosity. The rate of increase diminishes as the pressure rises. At 15 p.s.i.g. K increases from 14·3 to $16{\cdot}5 \times 10^{-4}$ cm² as the viscosity increases from 1–50 cP. At 30 p.s.i.g. K increases from 14·0–$15{\cdot}5 \times 10^{-4}$ cm² over the same range of viscosity. This interaction of pressure and viscosity is to be expected since they both affect the flow pattern in the orifice.

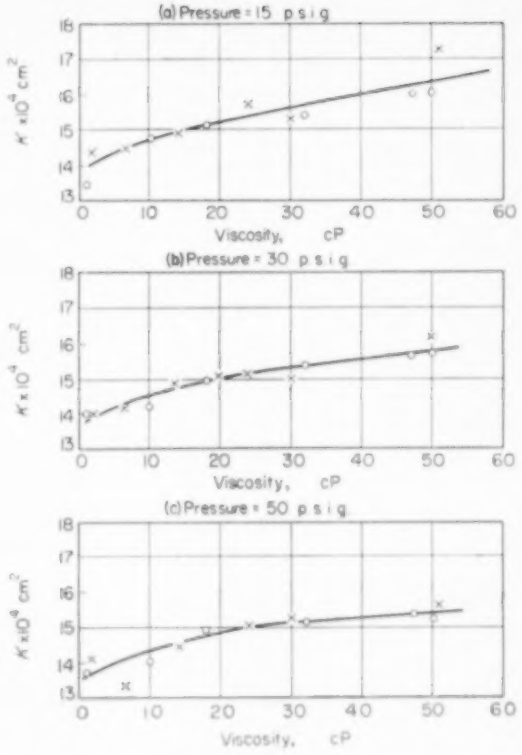

Fig. 14. The effect of viscosity and pressure on the thickness parameter K.
$x \approx 30$ dynes/cm ○ ≈ dynes/cm

Effect of liquid properties and injection pressure on the trajectory of the edge of a fan spray sheet

Equation (10) can be re-arranged to give

$$\frac{2.x.\gamma}{g.P.K.C_Q^2} = 1 - \sin(\beta + \theta)$$ whose validity

can be tested by plotting the parameters $x\gamma/P.K.$ and $\sin(\beta + \theta)$ since C_Q is constant. Since the origin of the sheet can be considered to be very close to the orifice, x has been measured from the orifice.

Fig. 15 illustrates the result for liquids of low viscosity (0·8 to 1·8 cP) and covering a wide

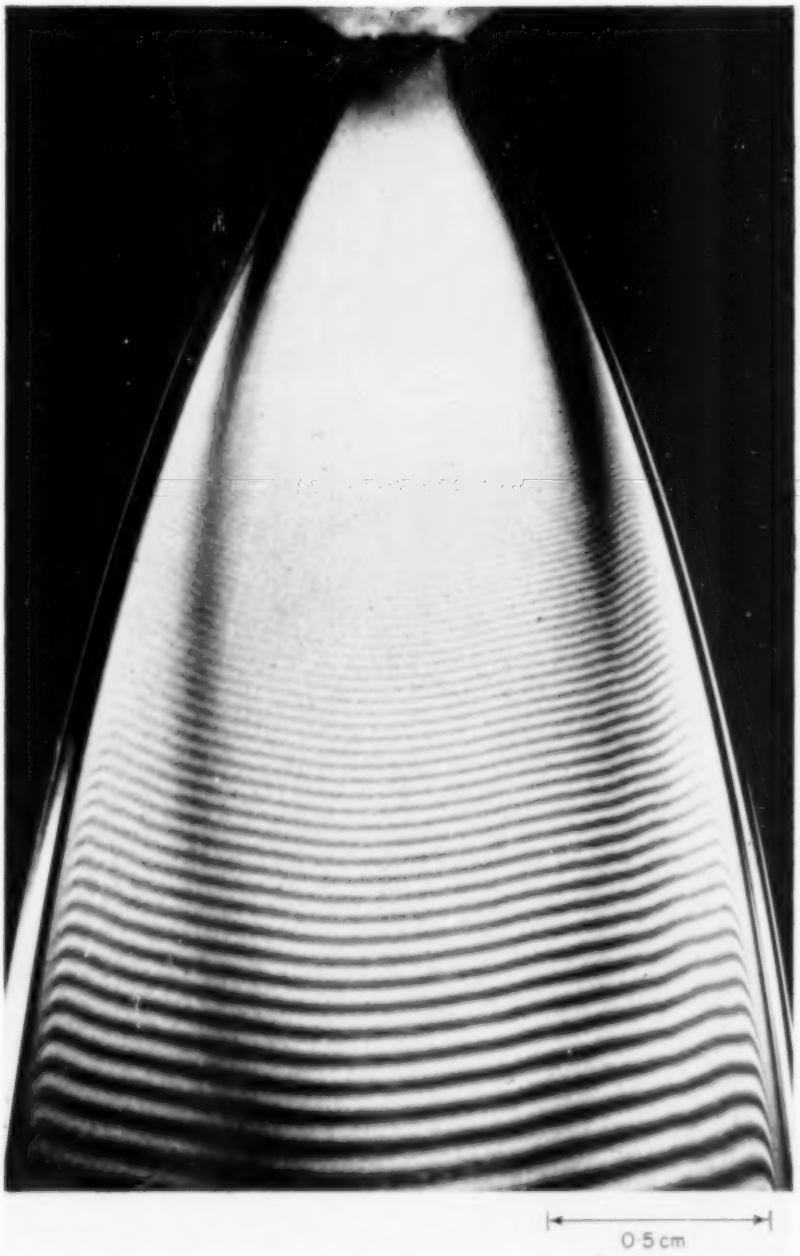

FIG. 13. Interferogram of sheet of viscous liquid (glycerol–water 50 cP at 15 p.s.i.g.).
(Exposure time 1/50 sec).

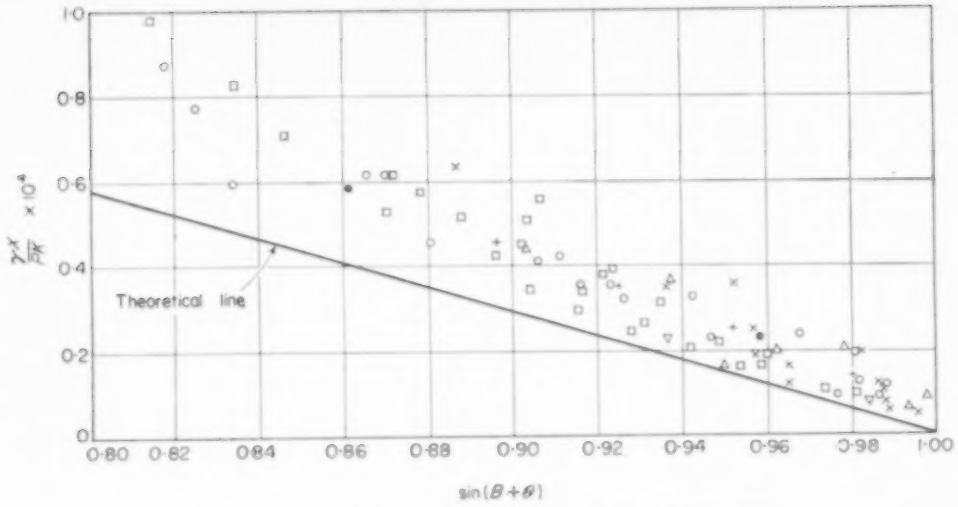

FIG. 15. The trajectory of the sheet edge at low viscosities.

	Liquid	ρ (g/cm³)	γ (d/cm)	η (cP)	pressure range (p.s.i.g.)		Liquid	ρ (g/cm³)	γ (d/cm)	η (cP)	pressure range (p.s.i.g.)
○	Water	1·0	72	1·0	10– 40	×	Kerosene	0·8	26	1·7	5– 40
⊗	17% glycerol-water	1·0	70	1·6	15– 15	△	Alcohol	0·8	20	0·9	5– 30
+	Benzaldehyde	1·0	40	1·6	15– 15	◁	Ethyl acetate	0·9	25	0·6	15– 15
						⊡	Mercury [16]	13·5	487	1·6	130–480

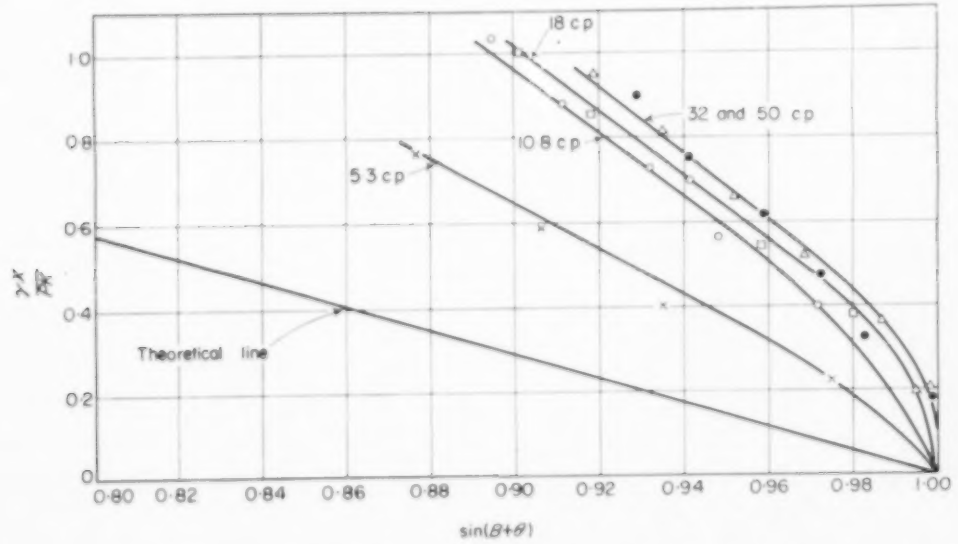

FIG. 16. The effect of viscosity on the trajectory of the sheet edge.
(Pressure 15 p.s.i.g., surface tension 70 dyn/cm). ⊗ 50 cp △ 32 cP ⊡ 18 cP ○ 10·8 cP × 5·3 cP

range of experimental conditions (injection pressure 5–480 p.s.i.g., surface tension 25–475 dyn/cm, and density 0·8 to 13·6 g/cm³. It shows that the experimental points lie within a band whose slope is somewhat greater than that of the theoretical line. i.e. the theory predicts smaller sheets than those observed in practice. This is to be expected since the derivation has not taken into account the fact that although most of the liquid amassing in the contracting rims is continuously being lost as drops are being ejected (cf. Fig. 2), the momentum remaining in them will restrain the action of the surface tension force. However, bearing in mind the complex nature of the problem, it can be seen that the basic assumptions underlying the theory are justified.

Fig. 16 illustrates the effect of a viscosity range of 1–50 cP at a constant injection pressure of 15 p.s.i.g. and mean surface tension of 70 dyn/cm. It shows the curves to deviate from the "inviscid" theoretical line by an extent depending on the liquid viscosity. This effect probably results from the reduction of the contraction velocity V_c' by viscous forces which were not taken into account in deriving the relations.

Fig. 17 illustrates the effect of liquids at one level of high viscosity and two levels of surface tension. The figure shows that liquids of higher surface tension deviate further from the theoretical line than liquids of lower surface tension. This is presumably a consequence of the greater viscous retarding forces operating at the higher contraction velocities for liquids of higher surface tension.

Fig. 18 illustrates the effect of viscosity at different levels of injection pressure and shows that the theoretical curvature is approached as the pressure is increased. This results from the fact that at high injection pressures the high radial velocities limit the extent to which the sheet can contract. Deviations from the theoretical contraction velocity will therefore only have a slight effect.

Discussion of Results

The effect of injection pressure, surface tension and viscosity on the thickness of the sheet can be attributed to two distinct causes, namely the conditions of flow inside and outside the orifice.

The flow inside a circular orifice can be characterized by the Reynolds number based on the orifice diameter [15], and therefore under conditions where the orifice flow controls the flow in the sheet, the thickness, as expressed by K, should be capable of correlation with the Reynolds number.

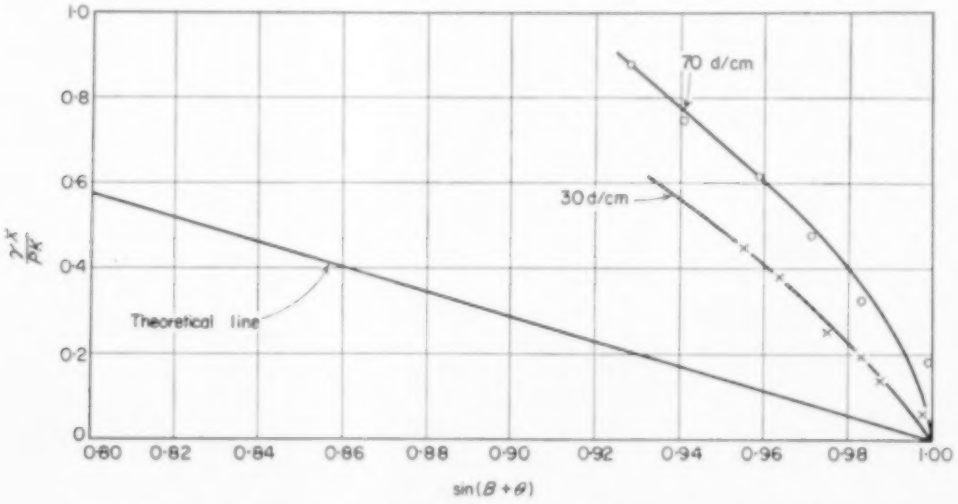

Fig. 17. The effect of surface tension on the trajectory of the sheet edge at high viscosity. (Viscosity 50 cP, pressure 15 p.s.i.g.).

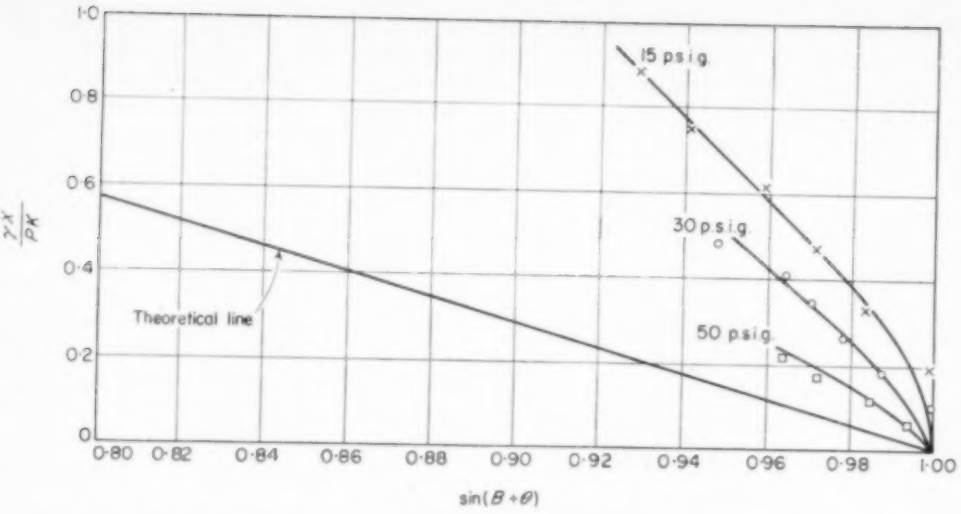

FIG. 18. The effect of ejection pressure on the trajectory of the sheet edge at high viscosity.
(Viscosity 50 cP, surface tension 70 dynes/cm)
× 15 p.s.i.g. ○ 30 p.s.i.g. ⊡ 50 p.s.i.g.

The present series of experiments were carried out with only one nozzle size so that the effect of the linear dimension in the Reynolds number cannot be verified. However, the remaining factors of viscosity, (η), density, (ρ) and velocity (V), can be grouped together in the form $V\rho/\eta = R$ $0 < n$ since the coefficient of discharge is constant the parameter R can be written as $(p\,\rho)^{1/2}/\eta$, where P is the injection pressure.

This group has been determined for all the

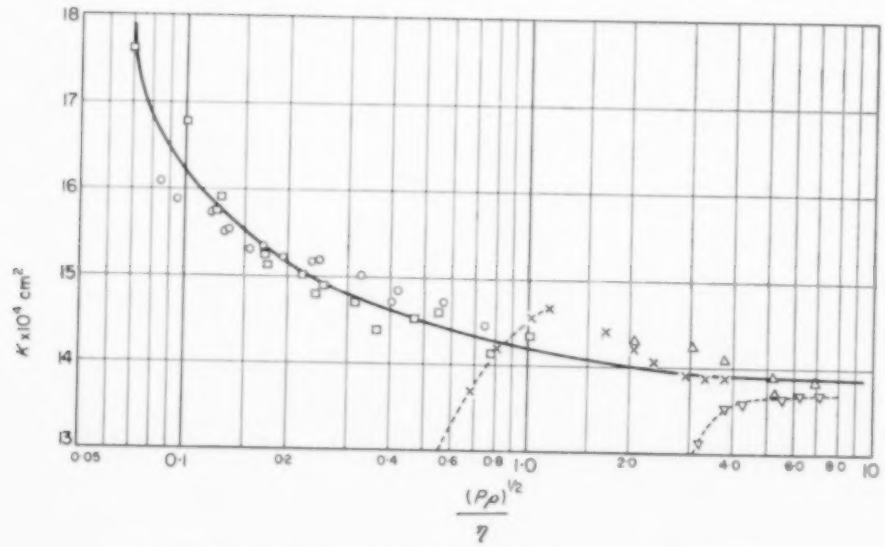

FIG. 19. Relation between $(P\rho)^{1/2}/\eta$ and the thickness parameter K.
× kerosene ▽ water ⊡ alcohol
○ water–glycerol ⊡ kerosene–paraffin

experimental conditions and is plotted on Fig. 19. The results show the points to lie satisfactorily around a smooth curve except the values for water and kerosene at low injection pressures (cf. Fig. 12). As the magnitude of R increases K tends asymptotically to a constant value of about 14×10^{-4} cm^2.

K is also related to the angle θ_T by equation (6), $2\theta_T$ being the total sheet angle if the edges were unconstrained by surface tension and the orifice exit passage. The equation predicts a linear relation between the orifice area and K. This has been confirmed from values of sheet thickness reported earlier [4] for water and a series of nozzles of the same design as that used in the present work. These data, converted to values of K, are plotted in Fig. 20. The angle, θ_T, calculated from the slope is 59°. The value of θ_T calculated by equation (6) for the nozzle used in the present work is plotted in Fig. 21 as a function of $(P\rho/\eta)^{1/2}$ and it can be seen that θ_T asymptotically approaches a maximum value of 75°. The exit half angle of the clearance passages (see Fig. 1c) is 60°, so that for the larger values of θ_T, the edges of the sheet must be constrained in order to leave at the former angle. This is confirmed by measurements of the sheet angle at the nozzle exit. The inconsistency in values of the two angles, for nozzles of nominally identical design, in the present and previous work must be due to minor differences in the flow passages. This could not be easily ascertained because of the small size of the specimens.

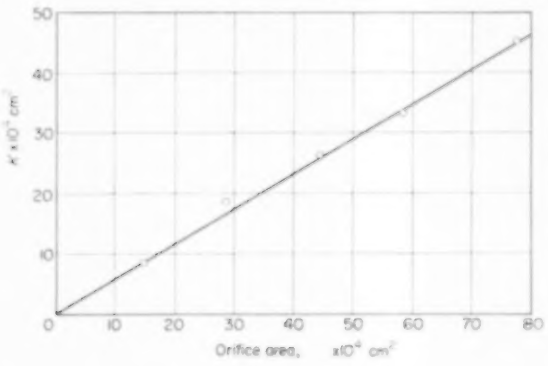

Fig. 20. Relation between orifice area and parameter K.

The observed variation of K and θ_T with flow conditions can be attributed to the movement of the centre of pressure behind the orifice. At a particular value of R, the centre of pressure is situated in such a position that the liquid flows

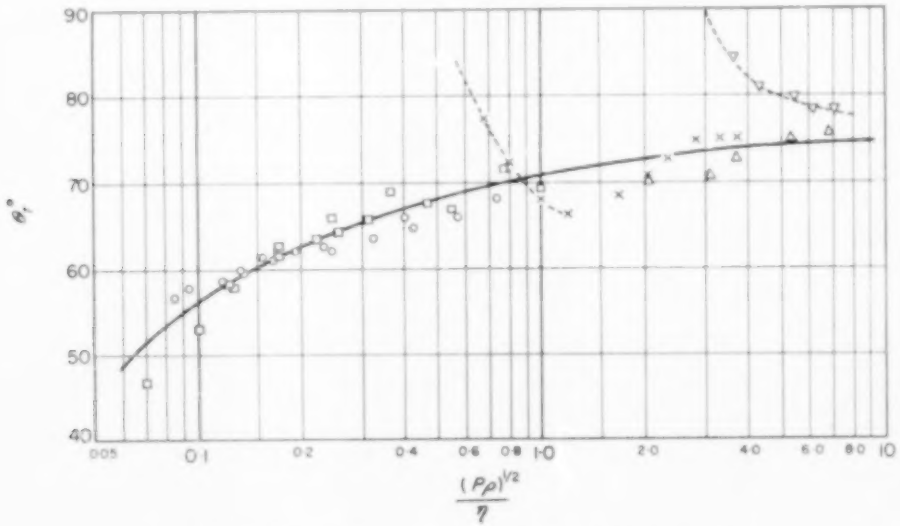

Fig. 21. Relation between $(P\rho)^{1/2}/\eta$ and the theoretical angle θ_T.

× kerosene ◁ water △ alcohol
○ water–glycerol ⊡ kerosene–paraffin

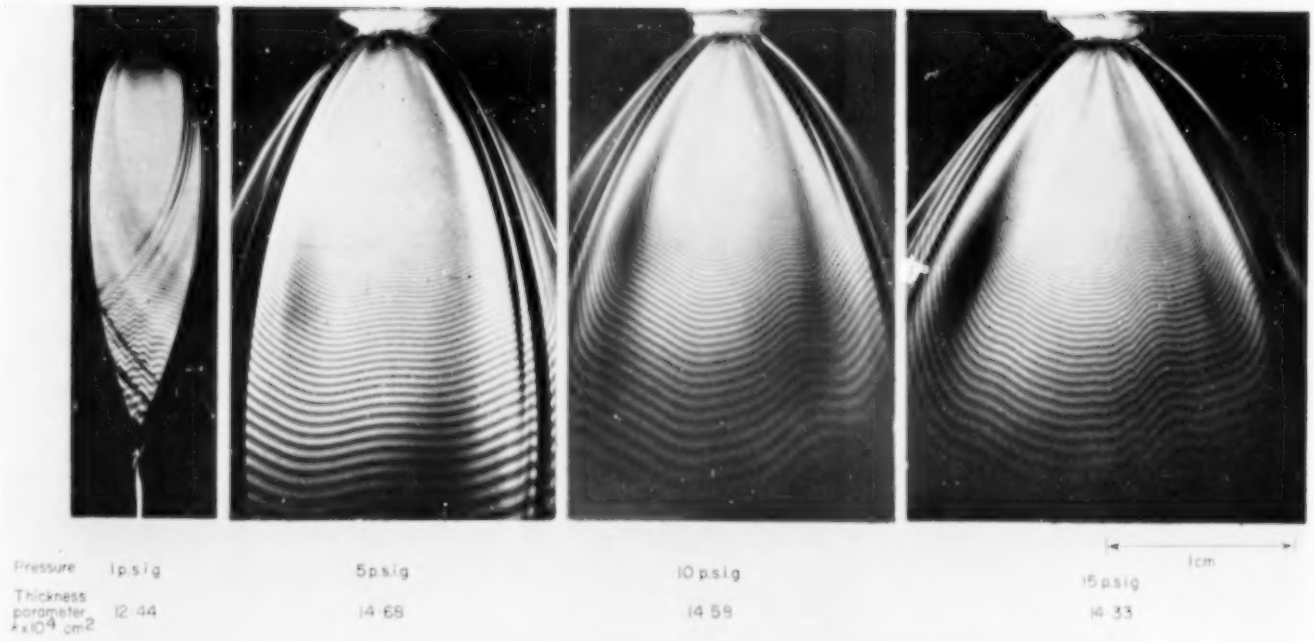

FIG. 22. Interferograms of kerosene spray sheets at increasing ejection pressures. (Exposure time 1/50 sec).

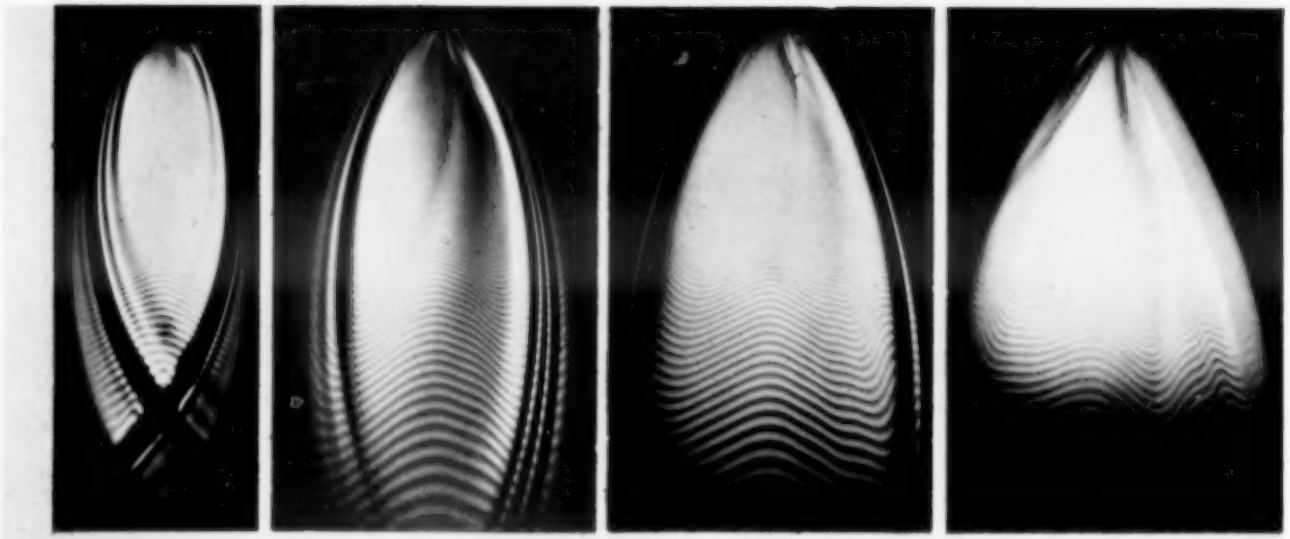

FIG. 23. Interferograms of water spray sheets at increasing ejection pressure. (Exposure time 1/50 sec).

directly along the exit walls (point A, Fig. 1). Under these conditions the value of the angle θ_T is identical with the angle θ (Fig. 5) at which the sheet leaves the orifice. At lower values of R, the centre of pressure moves upstream since viscous drag reduces the effective angle of convergence. This results in a thicker sheet (i.e. a larger value of K) diverging at a relatively small angle. An increased value of R causes the liquid streams to impinge at a larger angle so that the sheet tends to diverge to a greater extent as the centre of pressure moves towards the orifice. However, although the value of the angle θ_T is increased, the sheet edges are constrained by the exit walls so that the actual angle of the emerging sheet cannot increase further.

The results for kerosene and water at low injection pressures (Fig. 12) indicate an unusual flow pattern which cannot be explained by the conditions in the orifice and must be due to an external cause. A possible explanation lies in the fact that at least low pressures the spray sheet is completely bounded by thick rims. Under these conditions, surface tension forces are comparable to the momentum forces of the sheet and it is likely that the normal flow pattern in the sheet is affected.

This hypothesis is partly confirmed by examination of the interferograms of kerosene and water in Figs. 22 and 23 respectively. At low pressure, kerosene (surface tension 25 dyn/cm) exhibits fringe contours which are concave with respect to the orifice. As the pressure is increased to 5 p.s.i.g., the contours flatten out and then reverse to become convex. Since each fringe represents a line of equal sheet thickness, the photographs show that below 5 p.s.i.g., the central sector of the sheet is thinner than the surrounding parts and that the flow only approaches the ideal case at higher pressures. On the other hand, the fringe contours for water (surface tension 73 dyn/cm), corresponding to the asymptotic increase of K shown in Fig. 12, change their character only gradually, and remain concave at the highest pressure.

The occurrence of this flow pattern at low injection pressures probably accounts for the observation that at very low values the thick rims occasionally break away from each other to form two liquid jets. This is also a possible explanation for the fact that with liquids of low density and high surface tension such as sodium, the sheet is disrupted almost as soon as it is formed [6].

Acknowledgements—Valuable discussions with Professor D. M. Newitt, Mr. R. P. Fraser and Dr. P. Eisenklam are gratefully acknowledged. The authors also wish to thank the referee for his helpful coments, particularly with regard to the derivation of equation (8).

Notation

A = surface area of liquid
c = specific heat
C_Q = coefficient of discharge
D = orifice diameter — cm
E = internal energy of liquid when $A = 0$
g = acceleration due to gravity — ft/sec^2
H = enthalpy
K = thickness parameter $= xS$ — cm^2
m = mass flow rate
n = fringe number
P = pressure — p.s.i.g.
q = heat absorbed from surroundings
$R = v\rho/\eta$
r = fringe number of 1st resolvable fringe from orifice
S = sheet thickness — cm
S_r = the thickness of the sheet at a distance x_r from the orifice — cm
t = time
ΔT = change in temperature
Q = volume flow rate — cm^3/sec
U = internal energy of liquid
V = liquid velocity — cm/sec
V_c = velocity component normal to edge of sheet (Fig. 7)
w = work done by fluid on surroundings
x = distance from the orifice
x_r = distance of the rth fringe from the orifice
α = angle of refraction
β = angle shown on Figs. 5 and 7
γ = liquid surface tension — dyn/cm
η = viscosity cP
2θ = sheet angle at nozzle exit
$2\theta_T$ = sheet angle at orifice
λ = wavelength
μ = refractive index
ρ = density of liquid — g/cm^3
ϕ = angle of incidence

References

[1] Fraser R. P. *6th Int. Symp. Combustion.* Williams & Wilkins, Baltimore 1956.

[2] Fraser R. P., Eisenklam P. and Dombrowski N. *Brit. Chem. Engng.* 1957 **2** 414, 496, 536, 610.

[3] Fraser R. P. *Plant Protection Conference.* p. 237. Butterworths, London 1956.

[4] Straus R., Ph.D. Thesis, London University 1949.

[5] Dorman R. G. *Brit. J. Appl. Phys.* 1952 **3** 189.

[6] Dombrowski N. and Fraser R. P. *Phil. Trans.* 1954 **A247** 101.

[7] Fraser R. P. and Eisenklam P. *Trans. Inst. Chem. Engrs.* 1956 **24** 294.

[8] Squire H. B. *Brit. J. Appl. Phys.* 1953 **4** 167.

[9] Hagerty W. and Shea J. F. *J. Appl. Mech.* 1955 **22** 509.

[10] Hasson D., Ph.D. Thesis, London University 1956.

[11] Dombrowski N., Eisenklam P. and Fraser R. P. *J. Inst. Fuel.* 1957 **30** 399.

[12] Dixon B. R., Russell A. A. W. and Swallow J. E. L. *Brit. J. Appl. Phys.* 1952 **3** 115.

[13] Dukler A. E. and Bergelin O. P. *Chem. Engng. Progr.* 1952 **48** 557.

[14] Berthall T. *Brit. Pat.* 692, 609.

[15] Schweitzer P. H. *J. Appl. Phys.* 1937 **8** 513.

[16] Dombrowski N. and Eisenklam P. Agricultural Research Council Report ARC 198/52 1952.

[17] Rayleigh Lord *Proc. Lond. Math. Soc.* 1878/9 **10** 4.

[18] Dombrowski N., Fraser P. and Peck G. T. *J. Sci. Instrum.* 1955 **32** 329.

[19] Mensbrugghe M. G. Van Der *Brux. Acad. Bull.* 1881 **1** 286.

[20] Novikov I. I. *Zh. tekh. fiz., Moskva* 1948 **18** 345.

[21] Hodgkinson T. G. Unpublished M.O.S. paper (Porton Technical Note No. 174 1950).

[22] Weinberg S. *Proc. Inst. Mech. Engrs.* 1952 **1B** 240.

[23] Coulson J. M. and Richardson J. F. *Chemical Engineering.* Pergamon Press, London 1954.

[24] Harkins W. D. *The Physical Chemistry of Surface Films.* Reinhold, New York 1952.

Chemical Engineering Science, 1960, Vol. 12, pp. 51 to 55. Pergamon Press Ltd., London. Printed in Great Britain

Energy distributions in irradiated slurry chemical reactors

D. F. RUDD*
University of Minnesota

(*Received* 10 *August* 1959)

Abstract—Certain radiation promoted chemical reactions may be accelerated by the introduction of phosphorescent slurry particles into the reaction medium. These particles adsorb radiation energy in the regions of high radiation intensity and release this energy throughout the reactor. A solution for this distributed energy is obtained in terms of the properties of a stirred reactor radiation system and the results applied to a design problem.

Résumé—Les réactions chimiques activées par une radiation quelconque, peuvent être accélérées par l'introduction de particules d'une boue phosphorescente dans le milieu réactionnel. Ces particules adsorbent l'énergie de radiation dans les régions d'intensité de radiation élevée et libèrent cette énergie dans le réacteur. Une solution de cette répartition de l'energie est obtenue en fonction des propriétés du système de radiation du réacteur à agitation ; les résultats sont appliqués au calcul du réacteur.

Zusammenfassung—Einige durch Strahlung hervorgerufene chemische Reaktionen können durch Einführung phosphoroszierender Teilchen in das Reaktionsmedium beschleunigt werden. Diese Teilchen absorbieren Strahlungsenergie im Bereich hoher Intensität und strahlen diese Energie innerhalb des Reaktors aus. Die Energieverteilung wurde berechnet für den Fall eines gerührten Strahlungsreaktors und die Ergebnisse für ein Entwurfsproblem angewandt.

INTRODUCTION

RECENTLY there has been increased interest in the promotion of chemical reactions by high energy radiation. In industrial size reactors a large portion of the reaction medium is shaded from the radiation source. Slurry particles become activated in the regions of high intensity radiation and then lose this activation energy to the chemical reaction in the shadow regions. In many types of reactions the effectiveness of the radiation depends on this distributed energy.

An interesting example is the proposed scheme for the purification of space vehicle or submarine atmospheres by a photosynthesis reactor. The carbon dioxide laden atmosphere is fed into a series of chemical reactors in which light radiation promotes a photosynthesis reaction producing oxygen. Phosphorescent particles are introduced into the reactor to increase the efficiency of the light. These particles become active near the light source and then re-emit their energy in the shadow region.

This paper presents a method for the calculation of the average distributed energy in each unit of a series of continuous irradiated stirred tank reactors and extends the method to the case of a tubular reactor with axial dispersion.

THEORY

In irradiated continuous stirred tank reactors, slurry particles become active in regions of high radiation intensity and then lose that energy by decay to the chemical reaction. The complexity of this activation process suggests a probabilistic approach to the solution for the average distributed energy.

Let $g(\xi)$ be the energy associated with a particle at time ξ if it was activated at time zero. This function describes the rate at which the particle loses energy and is obtained by measurements on single isolated active particles.

The radiation is attenuated by the reaction medium: those particles nearer the radiation source have a higher probability of being activated.

*Present Address: Department of Chemical and Metallurgical Engineering, University of Michigan, Ann Arbor.

Let P denote the probability per unit time that a particle will become activated. This parameter depends on the intensity of the source, the mixing properties of the reactor and the opaqueness of the reaction medium. In the case of perfect mixing it can be estimated without difficulty.

Define $p(x)\,dx$ as the probability of a particle being at position x to $x + dx$. For the case of perfect mixing and axially symmetric geometry $p(x)\,dx = dx/H$ where H is the depth of the reactor.

$A(x)$ is the probability per unit time that a particle at position x will be activated. This probability function is proportional to the radiation intensity at position x, $I(x)$, the proportionality constant being the microscopic absorption cross section, β, of the particles.

$$A(x) = \beta I(x)$$

The probability that a particle is at position x to $x + dx$ and is activated in unit time is then

$$A(x)\,p(x)\,dx$$

The integral of this function over the entire reactor is defined as P.

$$P = \int_{x=0}^{H} \beta\, I(x)\, p(x)\, dx.$$

for perfect mixing and if the radiation is absorbed according to Beers law,

$$I(x) = I_0 \exp(-sx),$$

$$P = I_0\, \beta/s \left\{ \left[1 - \exp(-Hs) \right]/H \right\}$$

where I_0 is the radiation intensity at the source and s is the linear absorption coefficient of the reaction medium.

The age of a particle is defined as the time since its last activation. This distribution of ages can best be described by a distribution function $f(\xi)$. $f(\xi)$ is defined such that $f(\xi)\,d\xi$ is the fraction of particles of age ξ to $\xi + d\xi$. The average activity per unit mass of particles is then the weighted average

$$G = \int_0^{\infty} f(\xi)\, g(\xi)\, d\xi \qquad (1)$$

The distribution of ages in the k^{th} reactor of the series of reactors must now be determined in terms of the properties of the reactor-radiation system. This can be done by a material balance over the age group ξ to $\xi + d\xi$. The fraction of the particles activated in an increment of time $d\tau$ is $P d\tau$ and the fraction that escape activation is $1 - P d\tau$.

The total mass of particles of age ξ to $\xi + d\xi$ is $W f_k(x)\,dx$ where W is the total mass of particles in the reactor and the subscript k refers to the k^{th} reactor in the series. In the steady state the total mass of particles in the age group that appears in an increment of time $d\tau$ must equal the mass that disappears.

Particles in the age group ξ to $\xi + d\xi$ may appear by:

1. Natural ageing of younger particles in an amount $(1 - P d\tau)\, W f_k(\xi - d\tau)\, d\xi$.
2. Flow into the k^{th} reactor from the $k - 1^{\text{st}}$ reactor in an amount $w\, d\tau\, f_{k-1}(x)\, dx$ where w is the mass flow rate of particles.

The particles disappear by:

1. Activation in an amount $P d\tau W f_k(\xi)\, d\xi$.
2. Natural ageing in an amount $(1 - P d\tau)\, W f_k(\xi)\, d\xi$.
3. Flow from the reactor in an amount $w d\tau f_k(\xi)\, d\xi$.

The mathematical transliteration of the material balance is

$$(1 - P d\tau)\, W f_k(\xi - d\tau) + w\, d\tau f_{k-1}(\xi) = W f_k(\xi) + w\, d\tau f_k(\xi)$$

which becomes upon rearranging

$$\frac{f_k(\xi) - f_k(\xi - d\tau)}{d\tau} = -P f_k(\xi - d\tau) + \frac{w}{W}\left[f_{k-1}(\xi) - f_k(\xi) \right] \qquad (2)$$

Equation (2) becomes as $d\tau \to 0$

$$\frac{d f_k(\xi)}{d\xi} = -(P + Q) f_k(\xi) + Q f_{k-1}(\xi)$$

VOL 12 1960

where $Q = w/W$.

Particles of age 0 to $0 + d\xi$ appear by:

1. Activation of any particle in an amount $Pd\tau\, W$.
2. Flow into the reactor in an amount $wd\,\tau f_{k-1}(0)\, d\xi$.

They disappear by:

1. Natural ageing in an amount $(1 - Pd\,\tau)\, W f_k(0)\, d\xi$.
2. Flow out of the reactor in an amount $wd\,\tau f_k(0)\, d\xi$.

The material balance on this age group becomes as $d\tau \to 0$ and $d\xi \to 0$.

$$f_k(0) = P \tag{4}$$

Equation (4) is the boundary condition necessary for the solution of equation (3). Equation (3) is a standard linear ordinary differential equation whose solution is

$$f_k(\xi) = P \exp(-[P + Q]\,\xi) + Q \int_0^{\xi} \exp[-(P + Q)\,\eta] f_{k-1}(\xi - \eta)\, d\eta \tag{5}$$

Equation (5) shows how the age distribution function changes from reactor to reactor. This allows the calculation of the age distribution in the k^{th} reactor in terms of the properties of preceding reactors and the age distribution in the feed to the first reactor. The mean activity in the k^{th} reactor is obtained by use of equation (1).

These results can be extended to the case of an irradiated tubular reactor with axial dispersion. It has been shown [1] that a tubular reactor with axial dispersion can be approximated by a mixing cell (stirred tank) model. The length of the mixing cells must be chosen so that $u\Delta x/D = 2$ where Δx is the size of the mixing cell, u is the average velocity in the reactor and D is the axial dispersion coefficient. The average activity at position L in the reactor is approximately that given by equations (1) and (5) where k is taken as $L/\Delta x$.

An Example

The application of these theoretical developments can best be seen in a design problem. Consider the promotion of the biological reaction $A \to B$ in a series of illuminated continuous stirred tank reactors. The primary illumination activates phosphorescent particles which re-emit secondary radiation. This secondary radiation is of the proper wave length to promote the chemical reaction. How does the fractional conversion of this reaction system depend on the operating parameters?

The active particles lose their energy by exponential decay: that is, $g(\xi) = G \exp(-\alpha\xi)$ where G is the energy absorbed by the particles at the time of activation.

Experimental considerations show that the rate of reaction of specie A is of the form

$$\text{Rate} = C_A R \left(\rho \frac{G}{\bar{G}}\right)^n$$

where C_A is the concentration of A, ρ is the mass of particles per unit volume of reaction medium and both R and n are constants determined experimentally.

If the feed to the first reactor is inactive, equation (5) gives the age distribution in the k^{th} reactor as

$$f_k(\xi) = P \exp(-\xi[P + Q]) \sum_{S=1}^{k} \frac{(\xi Q^{S-1})}{(s-1)!}$$

Using equation (1) the average activity per unit mass of particles in the k^{th} reactor is

$$G_k = \frac{PG}{Q + P + \alpha}\left[\sum_{S=1}^{k}\left(\frac{Q}{Q + P + \alpha}\right)^{S-1}\right] \tag{6}$$

A material balance on the chemical specie A about the k^{th} reactor gives

$$C_A^{*} = C_A^{*-1}\left\{\frac{1}{1 + \phi R[\rho(G_k/G)]^n}\right\}$$

where ϕ is the nominal holding time of the reaction medium.

Equation (7) gives the concentration in the k^{th} reactor in terms of the feed concentration C_a^{*} and the properties of the preceding reactors.

$$C_A^k = C_A^e \prod_{s=1}^{k} \left\{ \frac{1}{1 + \phi R \left[\rho (G_S/G) \right]^n} \right\} \quad (7)$$

The fractional conversion $\psi_k = 1 - C_A^k/C_A^e$ is the fraction of the reactant A that has been converted at the k^{th} reactor. Using the relation for P as well as equations (6) and (7) the fractional conversion at the k^{th} stage is given by equations (8) and (9).

$$\psi_k = 1 - \prod_{s=1}^{k} \left\{ \frac{1}{1 + \phi R \left[\rho (G_S/G) \right]^n} \right\} \quad (8)$$

where

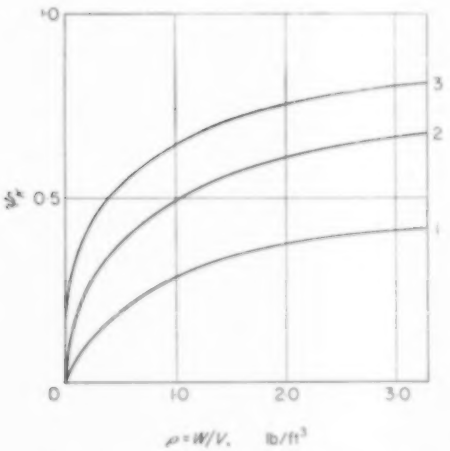

Fig. 1. The effect of the mass of particles per unit volume retained in the reactor on the fractional conversion.

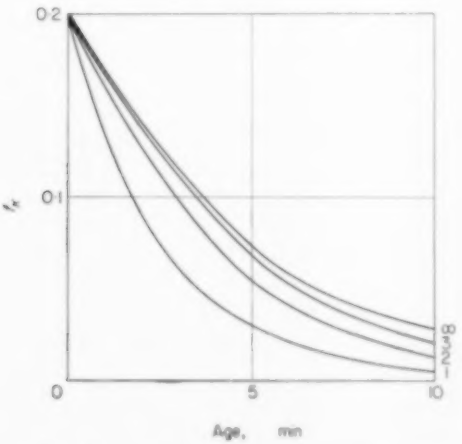

Fig. 2. The distribution of particle ages.

$$\frac{\rho G_S}{G} = \frac{(W I_0 \beta / VHs)(1 - \exp - sH)}{Q + (I_0 \beta / Hs)(1 - \exp - sH) + \alpha} \times \left(\sum_{l=1}^{S} \left[\frac{Q}{Q + (I_0 \beta / Hs)(1 - \exp - sH) + \alpha} \right]^{l-1} \right) \quad (9)$$

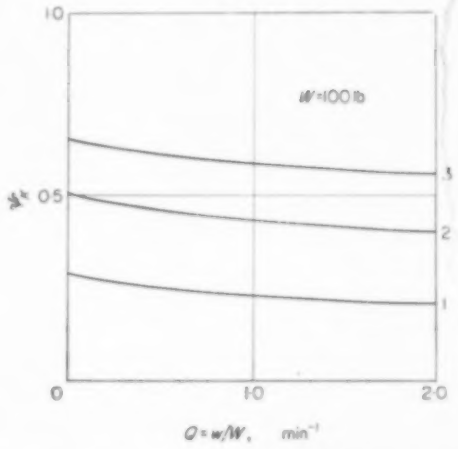

Fig. 3. The effect of the flow rate of particles on the fractional conversion.

The effects of the various operating parameters can best be shown graphically. Fig. 1 shows the effect on the fractional conversion of the mass of particles retained in each reactor. Fig. 2 shows the distribution of ages in each reactor in the series. The effect of the mass flow of inactive particles is shown in Fig. 3.

The effects of many other parameters can be studied (e.g., source intensity I_0, depth of the reactor H, etc.). These studies give insight into the performance of such a reactor system.

The physical constants used in the example are:

$$V = 100 \text{ ft}^3$$
$$R = 0{\cdot}285$$
$$n = 0{\cdot}5$$
$$I_0 \beta / s \left[1 - \exp - sH \right] / H = 0{\cdot}2 \text{ min}^{-1}$$
$$\phi = 3{\cdot}5 \text{ min}$$
$$\alpha = 1{\cdot}0 \text{ min}^{-1}$$

Conclusion

A mathematical model has been developed which isolates the effects of the important operating parameters in a series of irradiated continuous stirred tank slurry reactors. This model provides the insight for the experimental work that must follow.

Acknowledgements—I wish to thank Stephen Wilder and Rutherford Aris for their suggestions on the mathematical presentation.

Reference

[1] Coste J., Rudd D. F. and Amundson N. *Taylor Diffusion in Tubular Reactors.* In press.

Chemical Engineering Science, 1960, Vol. 12, pp. 56 to 64. Pergamon Press Ltd., London. Printed in Great Britain

On Denbigh's optimum temperature sequence

R. Aris

Department of Chemical Engineering, University of Minnesota, Minneapolis 14, Minnesota

(*Received* 9 *September* 1959)

Abstract—The example of an optimum temperature sequence in stirred tank reactors given by Denbigh is here discussed from the dynamic programming point of view. The notion of dynamic programming was developed to deal with just such optimum problems, in which a decision, in this case a choice of temperature, has to be made at each of N stages that will optimize some output of the whole process. A general presentation of the principle is given but application is made only to Denbigh's example. The solution is extended to the case where physical restrictions are imposed on temperatures and holding times.

Résumé—L'exemple donné par Denbigh d'une séquence de température optima dans des réacteurs à curve comportant une agitation est discuté ici du point de vue de l'établissement de la programmation dynamique. Cette notion est développée dans le but de traiter exactement ces problèmes où il faut décider du choix de la température à chacun des N étages ; cette température doit fournir le meilleur rendement pour l'opération globale. Une présentation générale du principe est donnée mais l'application n'est faite que sur l'exemple de Denbigh. La solution du problème est étendue au cas où des restrictions physiques sont imposées aux températures et aux temps de séjour.

Zusammenfassung—Das Beispiel einer optimalen Temperaturfolge in Rührwerksbehältern, die von Denbigh entwickelt wurde, wird vom Standpunkt der dynamischen Programmierung diskutiert. Die Kone zption der dynamischen Programmierung wurde zur Lösung von Optimierungs aufgaben entwickelt, bei denen eine Entscheidung (in diesem Falle die Wahl der Temperatur) auf jeder der N Stufen zu treffen ist, um die Ausbeute des ganzen Prozesses zu optimieren. Eine allgemeine Darlegung des Prinzips wird gegeben, die Anwendung erstrecket sich jedoch nur auf das Denbigh'sche Beispiel. Die Lösung wird für den Fall erweitert, wo physiaklische Einschränkungen für Temperaturen und Verweilzeiten getroffen werden.

1. Introduction

It has been recently shown by Denbigh [1] that remarkable improvement in yield may be made by correctly choosing the temperatures at which a sequence of stirred tank reactors should operate. The system of reactions he considered was

$$\begin{array}{ccccc} A + B & \xrightarrow{(1)} & X & \xrightarrow{(3)} & Y \\ \downarrow (2) & & \downarrow (4) & & \\ P & & Q & & \end{array}$$

in which X is an intermediate, Y the desired product and P and Q waste products. It is assumed that A is a costly raw material so that it is of importance to minimize the production of P and Q or maximize the yield of Y as a fraction of A. If the reaction (1) has a lower temperature coefficient than (2) it will be desirable to operate at a low temperature before any appreciable amount of X has formed, but if reaction (3) has a higher temperature coefficient than (4) a high temperature will be desirable in the later stages of the reaction. This suggests that two reactors, the first held at a lower temperature than the second, should give an improvement of the yield. How great an improvement this may be is shown by Denbigh's example, in which a single reactor at 360 °K gives a 25 per cent yield, whilst two reactors the first at 280 °K and the second at as high a temperature as possible give nearly 58 per cent conversion of A to Y. It was assumed that the second reactor was so large that the reactions, all of them first order and irreversible,

go virtually to completion and the holding time of the first reactor was taken to be the time at which the concentration of X in a batch reaction would be greatest. DENBIGH's method was one of direct calculation for various values of T_1 and T_2, the temperatures in the two reactors. He recognized that the holding time in the first reactor should also be varied but was able to show that the yield was not very sensitive to this. Even with two reactors, the method of direct calculation might, with less perspicacious handling or constants not so nicely chosen, founder in a morass of interminable approximation; if more than two reactors were considered, more than ordinary insight into the behaviour of the system would be required to organize such a calculation. Some interest therefore attaches to the problem of reducing these optimum calculations to a simple algorithm such as could be performed by a computer, human or mechanical, with no insight into the physical probabilities.

An organizing principle ideally suited to such problems is provided by the notion of dynamic programming. This has been developed by BELLMAN and his associates [2] and applied to a wide variety of multi-stage decision problems. This is just the kind of problem that confronts us; each reactor is a stage and at each stage a decision as to size and temperature has to be made, which will optimize the final yield. In the next paragraph we will discuss the relevant part of dynamic programming in general terms, but return to DENBIGH's example to show how it works in practice. It will be obvious that the theory provides method of solving almost all optimum problems of this type. We shall not discuss the general problem here, for much of the interest and most of the instruction in any theory lies in specific cases, and with so elegant an example to hand it would be stupid to overlook it. An extended treatment of optimum problems in reactor design will be given elsewhere.

2. The Notion of Dynamic Programming

Consider a process consisting in a finite number of discrete stages N. The state of the process stream leaving the n^{th} stage can be described by a set of m quantities $p_n = (p_{n1}, p_{n2}, \ldots p_{nm})$ and the feed to the first stage is in the state p_0. Let the operating conditions at the n^{th} stage be given by a set of r quantities $q_n = (q_{n1}, q_{n2}, \ldots q_{nr})$. Then the effect of each stage is to transform the state of the incoming stream, p_{n-1}, into the state p_n, this transformation depending on the operating variables q_n. Accordingly we may write

$$p_n = T(p_{n-1}; q_n) = T_n(p_{n-1}) \qquad (1)$$

In the present context we may think of p_n as concentrations of components, q_n as holding time and temperature and the transformation as the reaction. The sequence of states $p_1, p_2, \ldots p_n$ is generated from the initial state p_0 by a series of transformations $T_1, T_2, \ldots T_n$ which depend on the choice of operating variables $q_1, q_2, \ldots q_n$. Any choice of the operating variables is called a policy, and if the q_n satisfy certain imposed restrictions (e.g. temperatures must be with certain limits) the policy is called admissible.

We now define a profit function $\{P(p_N) - P(p_0)\}$ which is a measure of our satisfaction over the change of state resulting from the process; in the present case this might be the yield of the valuable product. The admissible operating policy which maximizes $P(p_N)$ for given initial state is said to be the optimum N stage policy with respect to the initial state p_0, and this is the summum bonum we seek. When this policy has been found the resulting maximum of P is a function only of the initial state p_0 and we may write

$$f_N(p_0) = \text{Max}\{P(p_N) - P(p_0)\} \qquad (2)$$

the maximization being over all admissible policies $q_1, \ldots q_n$. If we were to seek this maximum directly we should have to vary all the rN policy variables simultaneously and this would be a considerable task. However, if we consider the N stage process as a first stage followed by an $(N-1)$ stage process, it is clear that whatever the choice of operating variables in the first stage, the overall policy cannot possibly be optimum unless the remaining $(N-1)$ stages use the optimum $(N-1)$ stage policy with respect to the state p_1 resulting from the first stage. Moreover by varying q_1 and so p_1 we shall find the q_1 which together with the optimum $(N-1)$

stage policy constitutes an optimum N stage policy.

Since $P(p_N) - P(p_0) = \{P(p_1) - P(p_0)\} + \{P(p_N) - P(p_1)\}$ we can express this principle in an equation

$$f_N(p_0) = \text{Max}\{P(p_1) - P(p_0) + f_{N-1}(p_1)\} \quad (3)$$

where

$$p_1 = T_1(p_0) \quad (4)$$

and the maximization is now only over the admissible policies q_1. Equation (3) may be transliterated by saying that

$$\begin{pmatrix}\text{The maximum}\\ \text{profit from } N\\ \text{reactors with}\\ \text{feed } p_0\end{pmatrix} = \text{Maximum}\left[\begin{pmatrix}\text{The profit made}\\ \text{in the first re-}\\ \text{actor with feed}\\ p_0\end{pmatrix} + \begin{pmatrix}\text{The maximum profit}\\ \text{that can be made}\\ \text{by } (N-1) \text{ reactors}\\ \text{with feed } p_1\end{pmatrix}\right]$$

where p_1 is the state of the product from the first reactor with feed p_0 and operating conditions q_1 and the maximum is sought by varying q_1. The principle of optimality has reduced the number variables that have to be simultaneously varied in seeking a maximum from rN to r. Since the amount of work depends exponentially on the number of simultaneously varying quantities this is a most important saving. The sequence of equations (3) must be started by solving the single optimum

$$f_1(p_0) = \text{Max}\{P(p_1) - P(p_0)\} \quad (5)$$

In seeking an optimum policy with respect to the particular feed state p_0 we have had to imbed the problem in a rather larger one, for at any rate until the $(N-1)^{\text{th}}$ stage we have to determine $f_n(p)$ for a whole set of states p, since in general variation of q_1 will make p_1 vary over a certain domain of p-space. The problem is still far from trivial but it has been reduced to a straightforward algorithm and one well-suited to repeated application. In addition the functions and policies generated on the way are not without interest or use, for it would be a short-sighted analysis that considered only one initial state p_0. Furthermore restrictions such as upper and lower bounds on the variables q_n, which are difficult to handle analytically, actually make the problem easier from the point of view of mechanical computation, for they confine the area of search.

3. The Equations

We will denote by a, x and y the concentrations of A, X and Y and let t be the holding time of a reactor. If suffix n denotes the values at the n^{th} stage a mass balance gives the three equations

$$a_{n-1} = a_n + t_n(k_{1n} + k_{2n})a_n \quad (6)$$

$$x_{n-1} = x_n - t_n k_{1n} a_n + t_n(k_{3n} + k_{4n})x_n \quad (7)$$

$$y_{n-1} = y_n - t_n k_{3n} x_n \quad (8)$$

Here $k_{in} = k_i(T_n)$ is the rate constant of the i^{th} reaction at the temperature of the n^{th} reactor. To reduce the number of rate constants we follow Denbigh in using the ratios of the reaction rates. Let

$$r_n = k_{2n}/k_{1n}, \quad s_n = t_n k_{1n} \quad (9)$$

Since r_n is a function of T_n only and is monotonic we can let it play the role of temperature in what follows; s_n will then define the holding time when T_n is known.

Specifically, if $k_i = k_i^* \exp - E_i/RT$,

$$T_n = (E_2 - E_1)/R \ln(k_2^*/r_n k_1^*) \quad (10)$$

and

$$t_n = s_n\{r_n^{-E_1} k_1^{*-E_2} k_2^{*E_1}\}^{1/(E_2-E_1)} \quad (11)$$

The variable r is the ratio r_2 in Denbigh's notation and the other ratios $r_3 = k_3/k_1$ and $r_4 = k_4/k_2$ can be expressed in terms of r in the form $r_j = p_j r^{q_j}$, where, for example $q_3 = (E_3 - E_1)/(E_2 - E_1)$ and $(E_2 - E_1)\ln p_3 = (E_3 - E_2)k_1^* + (E_1 - E_3)k_2^* + (E_2 - E_1)k_3^*$. If we were to do a complete study of all reaction systems of this type we should have essentially four parameters p_3, q_3, p_4, p_4 to vary. This might be carried through the analysis that follows but for simplicity we will immediately adopt Denbigh's values

$$r_3 = 10^{-2} \qquad r_4 = r^{-1} \quad (12)$$

Equations (6)–(8) now become

$$a_{n-1} = \{1 + s_n (1 + r_n)\} a_n$$
$$x_{n-1} = -s_n a_n + \{1 + 10^{-2} s_n r_n^{-1} \times (1 + r_n)\} x_n$$
$$y_{n-1} = -10^{-2} s_n x_n + y_n$$

As a final simplification we notice that these equations are homogeneous of the first degree so that we can deal in the ratios of the concentrations.

Let

$$\left.\begin{aligned} a_n/a_{n-1} &= 1/(1 + \alpha_n) \\ x_n/a_n &= \xi_n \\ (y_n - y_{n-1})/a_{n-1} &= \eta_n \end{aligned}\right\} \qquad (13)$$

then the preceding equations may be solved to give

$$\alpha_n = s_n (1 + r_n) \qquad (14)$$

$$\xi_n = L_n + \xi_{n-1} M_n \qquad (15)$$

$$\eta_n = Y_n + \xi_{n-1} Z_n \qquad (16)$$

where

$$L_n = 100\, Z_n = \frac{\alpha_n}{1 + r_n} \left(1 + \frac{\alpha_n}{100\, r_n}\right)^{-1}$$
$$M_n = (1 + \alpha_n) \left(1 + \frac{\alpha_n}{100\, r_n}\right)^{-1} \qquad (17)$$
$$Y_n = 10^{-2} \frac{\alpha_n^2}{(1 + \alpha_n)(1 + r_n)^2} \left(1 + \frac{\alpha_n}{100\, r_n}\right)^{-1}$$

The variable a_n is related to the fraction of A which is used in the n^{th} stage and it simplifies the algebra slightly to use it in place of s_n. α_n is thus playing the role of the holding time t_n and this is perfectly satisfactory since the Jacobian $\partial(T_n, t_n)/\partial(r_n, \alpha_n)$ nowhere vanishes.

Before formulating the dynamic programme we will consider the optimum conditions in a single reactor. We wish to maximize η_1, i.e. the yield of Y as a fraction of A. Firstly it is easy to show by differentiating that η_1 is a monotonic increasing function of α_1 so that α_1 should be made as large as possible; in fact, the assumption that the reaction goes to completion is equivalent to $\alpha_1 \to \infty$.

Secondly by differentiation with respect to r_1 and rearrangement we find that for any given α_1, η_1 is maximum when r_1 satisfies the equation

$$\xi_0 = \frac{\alpha_1}{1 + \alpha_1} \frac{200\, r_1^2 - \alpha_1 (1 - r_1)}{(\alpha_1 - 100\, r_1^2)(1 + r_1)} \qquad (18)$$

For constant ξ_0 the solution of this equation is a curve in the α, r plane lying between the extremes for $\xi_0 = 0$ and ∞, namely

$$\xi_0 = 0, \quad \alpha_1 = 200\, r_1^2/(1 - r_1) \qquad (19)$$

and

$$\xi_0 = \infty, \quad \alpha_1 = 100\, r_1^2 \qquad (20)$$

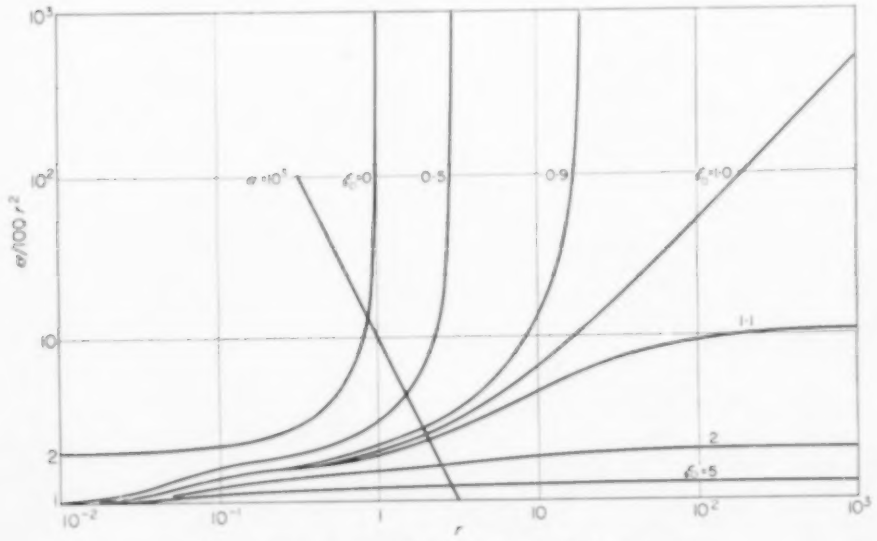

FIG. 1. Optimum conditions for a single reactor.

Unfortunately these lie in a rather narrow band even in the log x, log r plane (see Fig. 4) and to show better how they run Fig. 1 is a plot of $\log(x/100\,r^2)$ versus $\log r$. For $\xi_0 < 1$ the curves have vertical asymptotes at $r_1 = (1+\xi_0)/(1-\xi_0)$, for $\xi_0 > 1$ they have horizontal asymptotes. The optimum temperature for any x_1 and ξ_0 is given by the value of r_1 at the intersection of the curve with appropriate ξ_0 and the straight line $x_1/100\,r_1^2$; one of these lines is shown.

When the reaction goes to completion we can obtain explicit formulae, for as $\zeta_1 \to \infty$, $x \to \infty$ by (14); (16) and (17) then give

$$\eta_1 = \frac{r_1}{(1+r_1)^2} + \xi_0 \frac{r_1}{1+r_1} \tag{21}$$

whence the optimum conditions are

$$\left.\begin{aligned} &\xi_0 \leqslant 1, \quad r_1 = (1+\xi_0)/(1-\xi_0), \\ &\qquad\qquad \eta_1 = (1/4)(1+\xi_0)^2 \\ &\xi_0 > 1, \quad r_1 = \infty, \quad \eta_1 = \xi_0 \end{aligned}\right\} \tag{22}$$

Actually r_1 cannot be infinite, its limit being k_2^*/k_1^* as $T_1 \to \infty$. We shall assume however, as in Denbigh's example, that it is very large so that the simple formula (22) may be used. The necessary modifications to make (22) exact are not difficult to make.

4. Dynamic Programming Formulation

In fact r_1 cannot be infinite as the optimum policy demands, for it approaches k_2^*/k_1^* as $T \to \infty$. We shall assume, as in Denbigh's example, that this ratio is so large that $r_1/(1+r_1)$ is very close to 1 for high temperatures and $r_1/(1+r_1)^2$ is very small. Then we can retain as a very good approximation the simple formula $\eta_1 = \xi_0$ in (22); the necessary modifications to make this exact are not difficult to make.

Let

$$f_N(a_0, x_0) = \operatorname{Max}(y_N - y_0) = \operatorname{Max} \sum_{n=1}^{N} (y_n - y_{n-1}) \tag{23}$$

where the maximization is overall admissible policies (x_n, r_n), $n = 1, 2, \ldots N$. Since a_1, x_1 is the feed composition to the second stage and this is the first of the $(N-1)$ stage process as described in Section 2, the principle of optimality given there asserts that

$$f_N(a_0, x_0) = \operatorname{Max}\{y_1 - y_0 + f_{N-1}(a_1, x_1)\}. \tag{24}$$

where the maximization is now over admissible first stage policies, (x_1, r_1). In words equation (24) states that the maximum yield from N reactors is the maximum of "what can be made in the first reactor plus the maximum yield from the feed produced by the first reactor."

We can use the homogeneity of the equations to simplify this equation by writing

$$a_0 g_N(\xi_0) = f_N(a_0, x_0),$$

then dividing through (24) by a_0 gives

$$\begin{aligned} g_N(\xi_0) &= \operatorname{Max}\left\{\frac{y_1 - y_0}{a_0} + \frac{a_1}{a_0} g_{N-1}(\xi_1)\right\} \\ &= \operatorname{Max}\left\{\eta_1 + \frac{1}{1+\alpha_1} g_{N-1}(\xi_1)\right\} \end{aligned}$$

A further modification is quite valuable before setting down the final equations. Since a_n is continually decreasing the ratio ξ_n may become quite large, and this will cause difficulty in interpolating for $g_{N-1}(\xi_1)$. If we also introduce the reciprocal of ξ_0 we can use it when $\xi_0 > 1$ and so always keep the arguments of the functions in the range (0, 1).

Let
$$\zeta_n = \xi_n^{-1} = a_n/x_n \tag{25}$$

and
$$a_0 g_n(\xi_0) = x_0 h_n(\zeta_0) = f_n(a_0, x_0) \tag{26}$$

then in place of equation (24) we have four equations to be used according as ξ_0 and ξ_1 are greater or less than unity.

$$\begin{aligned} &\xi_0 \leqslant 1, \ \xi_1 \leqslant 1: \\ &\qquad g_n(\xi_0) = \operatorname{Max}\left\{\eta_1 + \frac{1}{1+\alpha_1} g_{n-1}(\xi_1)\right\} \\ &\xi_0 \leqslant 1, \ \xi_1 \geqslant 1: \\ &\qquad g_n(\xi_0) = \operatorname{Max}\left\{\eta_1 + \frac{\xi_1}{1+\alpha_1} h_{n-1}(\zeta_1)\right\} \\ &\xi_0 \geqslant 1, \ \xi_1 \leqslant 1: \\ &\qquad h_n(\zeta_0) = \operatorname{Max}\left\{\eta_1\,\zeta_0 + \frac{\zeta_0}{1+\alpha_1} g_{n-1}(\xi_1)\right\} \\ &\xi_0 \geqslant 1, \ \xi_1 \geqslant 1: \\ &\qquad h_n(\zeta_0) = \operatorname{Max}\left\{\eta_1\,\zeta_0 + \frac{\xi_1\,\zeta_0}{1+\alpha_1} h_{n-1}(\zeta_1)\right\} \end{aligned} \tag{27}$$

The terms other than g or h are calculated from calculated from equations (15) and (16) and all maximizations are over variation of x_1 and r_1.

For a single tank and complete reaction, $x_1 = \infty$, equations (22) give

$$g_1(\xi_0) = (1/4)(1 + \xi_0)^2, \quad h_1(\zeta_0) = 1 \qquad (28)$$

For $N \geqslant 2$ we cannot hope to find analytical expressions and the equations (27) must be solved by numerical computation. Figs. 2 and 3 summarize the results under DENBIGH's assumption of complete reaction in the last reactor $a_N = 0$. In Fig. 2 the functions g_1, h_1, g_2 and h_2 are shown and the single point $g_3(0)$. The values of $g_1(0) = 0{\cdot}25$ and $g_2(0) = 0{\cdot}574$ confirm the values calculated by DENBIGH and the fact that $g_3(0) = 0{\cdot}663$ shows that the three reactor system is a significant improvement on the two. The optimum policies for one, two and three reactors are compared in the following table.

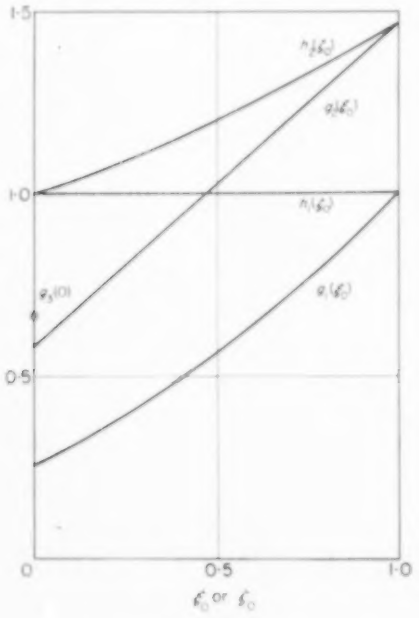

FIG. 2. Optimum yield for N = 1, 2.

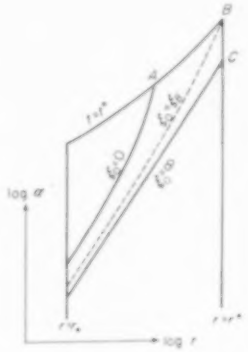

FIG. 3. Optimum policy for $N = 2$.

The values of r have been converted to temperature using the constants $(E_2 - E_1)$ and (k_2^*/k_1^*) from DENBIGH's paper. To ascribe values to t_s it is necessary to assume specific values for E_1 and k_1^* and use the optimum temperatures in equation (11).

Fig. 3 shows how the policy depends on ξ_0 or ζ_0. In the upper section r_1 is shown, this is the first reactor temperature in a sequence of two reactors. Part of the curve for $N = 1$ is shown but no attempt has been made to include much of it as it has a simple formula, (22). The middle section shows the policy with regard to s_1 with two reactors; s_2 is infinite by the assumption of complete reaction.

The lower section of Fig. 3 gives the outlet composition ratio ζ_1 from the first tank under

Table 1. *Comparison of optimum policies*

N	*Temperatures*			*"Holding times"*			*Yield* (%)
	T_1	T_2	T_3	s_1	s_2	s_3	
1	326	—	—	∞	—	—	25
2	280	∞	—	4·0	∞	—	57·4
3	270	320	∞	1·6	0·8	∞	66·3

the optimum policy. This last graph is needed to use these results in the three stage policy. For supposing (27) to have been solved for $N = 3$ and say $\xi_0 = 0$, we have the optimum values of r_1 and α_1 and hence of s_1 for the first reactor from the calculation but need to know what the policy for the other two reactors should be. The calculation has given the value of ξ_1 or ζ_1 at optimum conditions (in this case $\zeta_1 = 0{\cdot}84$) and this is the inlet to the remaining two reactors which employ optimum policy. We therefore treat 0·84 as the ζ_0 for $N = 2$ and get for the second $r_2 = 0{\cdot}51$ (point A), $s_2 = 3{\cdot}4$ (point B), i.e. the second reactor must be treated as the first of an optimum two stage reactor. The lower graph gives ζ_1 (0·84) = 0·1 (point C) and this is the outlet from the first stage of a two stage system, that is, the inlet to the third reactor. This we treat as ζ_2 the inlet to a one stage reactor which must be working under optimum conditions, or since it corresponds to $\xi_2 = 10 > 1$ the third reactor must have $r_3 = s_3 = \infty$.

5. The Optimum Problem Under Restrictions

It is of interest to see how the policy is changed and the method of getting it works out under some obvious physical restrictions. There will certainly be upper and lower bounds on the temperature, say $T_* \leqslant T_n \leqslant T^*$, and an upper bound on the holding time, $t_n \leqslant t^*$, since it is not practical to increase the holding time indefinitely by lowering the flow rate. These restrictions imply,

$$r_* \leqslant r_n \leqslant r^* \tag{29}$$

and

$$s_n \leqslant t^* k_{1n} = s^* r_n^{\,q}$$

where $q = E_1/(E_2 - E_1)$

and $s^* = t^* \{k_1^{*E_2} k_2^{*-E_1}\}^{1/(E_2-E_1)}$, and

hence $$\alpha_n \leqslant s^* r_n^{\,q}(1 + r_n). \tag{30}$$

These restrictions define an area in the α, r plane as shown in Fig. 4, since by the assumptions $q > 0$. Also shown on this Fig. are the curves $\xi_0 = 0$ and $\xi_0 = \infty$ from equation (18), between which all optimum conditions for the single tank

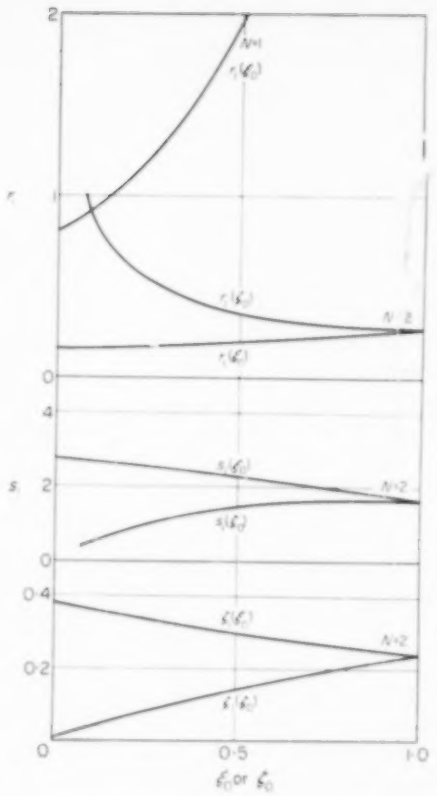

Fig. 4. Nature of the restrictions on the policy.

lie. Indeed since we know that α_1 should be made as large as possible the optimum conditions for given ξ_0 must lie at the intersection of the curve corresponding to the given ξ_0 and the upper part of the boundary, ABC. As drawn here there is a value ξ_B of ξ_0 for which the curve goes through the point B. For $\xi_0 \leqslant \xi_B$ the curves will intersect the arc AB, meaning that the restriction on holding time is the controlling one. For $\xi_0 \geqslant \xi_B$ the curves intersect on BC, where the temperature is the controlling restriction.

To show how this works out in Denbigh's example we have taken $q = 1$, $r_* = 0$, $r^* = 5$ and $s^* = 420$, for which Fig. 4 shows the nature of the restrictions; $\xi_B = 0{\cdot}914$. To calculate g_1 and h_1 it is best to work backwards from a given point of the arc ABC, calculating ξ_0 from equation (18) and η_1 from equation (16). These functions are shown in Fig. 5 and it is at once

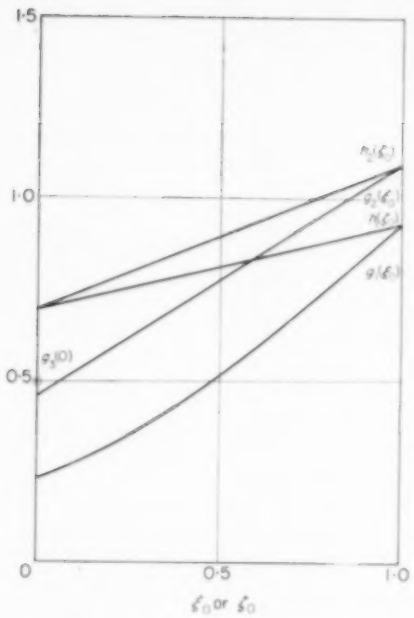

Fig. 5. Optimum yield with restricted policy.

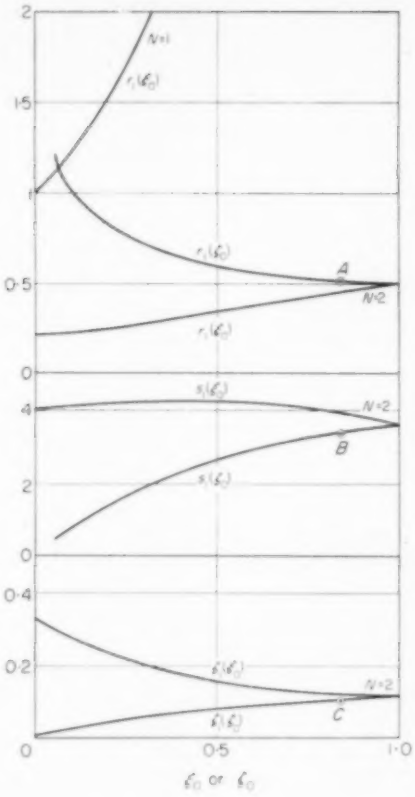

Fig. 6. Optimum policy with restrictions.

evident that the restriction on temperature ($T^* = 394$) has an appreciable effect on the yield. To calculate g_2 and h_2 equations (27) were again solved numerically, this time with the maximizations over all r_1 and α_1 satisfying the restrictions (29) and (30). Fig. 6 shows the policy for the restricted optimum problem and may be compared directly with Fig. 3. The following table summarizes the optimum policies and yields for the restricted problem with $\xi_0 = 0$, and the values of r have again been translated into temperature using Denbigh's constants. Since we have assumed $q = 1$ we can translate the values of s into the ratio of holding times of reactors, it is of course not possible to get absolute magnitudes until k_1^* is given. Thus in the three tank optimum the ratios $t_1 : t_2 : t_3 = 3{\cdot}4 : 100 : 1$.

6. Discussion

By modifying the profit function we might solve a number of similar and perhaps more realistic optimum problems. For example if we

Table 2. Comparison of restricted optimum policies

N	*Temperatures*			*"Holding times"*			*Yield* (%)
	T_1	T_2	T_3	s_1	s_2	s_3	
1	318	—	—	340	—	—	22·1
2	276	394	—	2·82	2100	—	45·1
3	260	288	394	1·4	1·3	2100	49·5

associate a cost, c, with A and a value, v, with the product Y we might seek the maximum of $P = v(y_N - y_0) - c(a_0 - a_N)$, which is literally the net profit of the reaction. Alternatively it would be possible to allow for the cost of the reactor system by taking it to be some function of the holding times t_n. In this case the formulation we have given would not be the most suitable and it would be better to work directly with the holding time and temperature. The particular form we have chosen is the simplest for hand calculation, for machine calculation it might well be better to work from equations (6)–(8) without transformation. However, it is hoped that sufficient has been said to show how valuable a tool the notion of dynamic programming is in the study of such optimum problems.

Acknowledgements—I am indebted to Mr. KUNG-YOU LEE of this university for help with the calculations in this paper.

NOTATION

a = concentration of A
E_i = activation energy of i^{th} reaction
$f_N(a_0, x_0)$ = optimum yield from N reactors
$g_N(\xi_0) = f_N(a_0, x_0)/a_0$
$h_N(\xi_0) = f_N(a_0, x_0)/x_0$
k_i = reaction rate if i^{th} reaction $= k_i^* \exp(-E_i/RT)$
L, M = functions defined by equation (17)
N = number of stages
n = number of reactor
P = profit function
p_n = state of stream leaving the n^{th} stage
q_n = operating variables at the n^{th} stage
R = gas constant
$r = k_2/k_1$
r^* = upper bound on r
r_* = lower bound on r
$s = t k_1$
T = temperature
t = holding time
t^* = upper bound on holding time
x = concentration of X
y = concentration of Y
Y, Z = functions defined by equation (17)
$\alpha = s(1 + r)$
$\zeta = a/x$
$\eta_n = (y_n - y_{n-1})/a_{n-1}$
$\xi = x/a$

REFERENCES

[1] DENBIGH K. G. *Chem. Engng. Sci.* 1958 **8** 125.
[2] BELLMAN R. *Dynamic Programming*. Princeton University Press 1957.

Vapour liquid equilibria for ethanol–water–ethylene glycol system

(*Received* 10 *May*, 1959)

Abstract—Vapour–liquid equilibrium data for the system ethanol–water were determined at one atmosphere pressure in the presence of ethylene glycol using an Othmer still in order to study the effect of glycol on the relative volatility of ethyl alcohol. The results of the investigations indicate the disappearance of the binary azeotrope between ethyl alcohol and water at the concentrations of the solvent studied in this work.

Résumé—Les données d'équilibre liquide–vapeur pour le système éthanol–eau sont déterminées à une pression de une atmosphère en présence d'éthylène glycol en utilisant l'appareil d'Othmer de façon à étudier l'effet du glycol sur la volatilité relative de l'alcool éthylique. Les résutlats des recherches montrent la disparition de l'azéotrope binaire entre alcool éthylique et eau aux concentrations de solvant étudiées dans ce travail.

Zusammenfassung—Dampf–Flüssigkeits-Gleichgewichte für das System Aethanol–Wasser bei 1 atm Druck und in Gegenwart von Aethylenglykol wurden in einer Othmer-Apparatur bestimmt, un den Einfluss des Glykols auf die relative Flüchtigkeit von Aethanol zu studieren. Die Ergebnisse zeigen das Verschwinden des binären Azeotrops zwischen Aethanol und Wasser im Bereich der verwendeten Konzentrationen des Lösemittels an.

VOL. 12 1960

Introduction

Ordinary distillation of ethyl alcohol yields a product containing nearly 10·6 mole % of water due to the formation of an azeotrope. Further dehydration of ethyl alcohol can be carried out only in the presence of an added component using the principle of azeotropic distillation or extractive distillation. Benzene and similar hydrocarbons [1], trichloroethylene [2], ether [3] etc., which form binary or ternary azeotropes with ethanol–water system have been used as entrainers. In the field of extractive distillation high boiling liquids such as glycerol, glycols etc., have been recommended by Mariller [4] as early as 1936. Cederquist [5] reports the economical working of the plants in Sweden using ethylene glycol as the extracting agent for the production of absolute alcohol. However, a systematic investigation of vapour-liquid equilibria of ethanol–water systems in the presence of ethylene glycol has not been reported in the literature. The present study was, therefore, undertaken to determine such data which are essential for the design of the extractive distillation unit.

Materials Used

Ethyl alcohol: Dehydrated alcohol supplied by the Madras Medical Store was distilled over calcium turnings and used. (Density d_4^{30} 0·7808: Refractive index n_D^{30} 1·3570).

Ethylene glycol: Pure glycol supplied by E. Merck & Co. was distilled under a vacuum of 72 cm Hg and the fraction collected at 120°C was used. (Density d_4^{30} 1·1063: Refractive index n_D^{30} 1·4283).

Water: Laboratory distilled water was redistilled and used.

Experimental Procedure

Vapour liquid equilibrium data were determined using a modified form of Othmer's still described by Othmer *et al.* [6] with slight modification to improve the accuracy of the readings as evaluated by a series of runs with an ethyl alcohol–water system. The upper portion of the boiling chamber and the vapour outlet were provided with nichrome coils embedded in a coating of asbestos magnesia to maintain the temperature of the walls slightly higher than the boiling point to avoid errors due to condensation.

The charge for the experimental runs was prepared by mixing weighed amounts of the three

components, so that, while the solvent concentration was kept a constant, the other two components were varied. A known amount of a mixture corresponding to the approximate vapour composition was added to the charge initially and the three way stopcock was adjusted to build up this much of condensate hold-up during the runs. The steady conditions were reached after about 2–3 hr as indicated by the constant volume of the hold-up and the constant boiling temperature of the liquid. The system was allowed to maintain this equilibrium state for about 1 hr, before samples were taken in stoppered iodine flasks which were immediately cooled.

The analysis of the ternary mixtures was based on the measurements of physical properties such as density and viscosity. Synthetic mixtures of the three components were prepared by accurate weighing and the physical properties were measured at 30°C in a thermostat. The readings were plotted to yield two families of curves for density and viscosity respectively and these graphs were used for analysing the equilibrium samples by interpolation. The small amounts of ethylene glycol present in the vapour samples were analysed by titration following the method described by Curme and Johnston [7].

Discussion of Results

Table 1 gives the experimental vapour liquid equilibrium data of ethanol–water on a glycol free basis at nearly constant concentrations of glycol in the liquid, along with the boiling points of the ternary mixtures. Fig. 1 shows the boiling point diagram for the ethanol–water system containing 50 per cent, 75 per cent and 90 per cent by weight of ethylene glycol in the overall mixture. It can be observed that the boiling point curve tends to become flat at the high alcohol region for 50 per cent glycol concentration, while increased solvent concentration makes the curve steeper. The differences in boiling points between the water end and the alcohol end of the boiling point curves are 17·6, 16·2 and 15·5 °C at 50 per cent, 75 per cent and 90 per cent of glycol by weight respectively, whereas it is 21·6 °C for the binary ethanol–water system. Fenske *et al.* [8] have reported that the boiling point difference

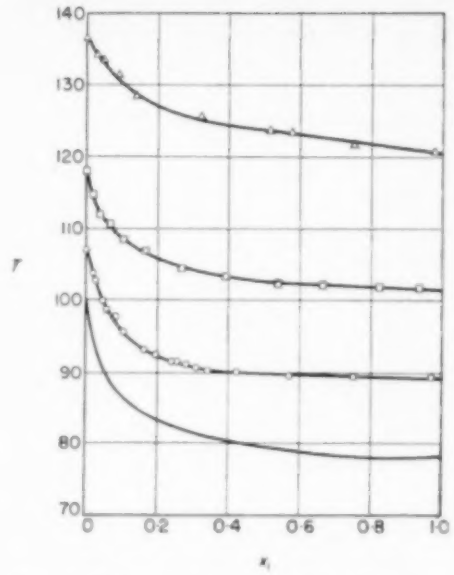

Fig. 1. Boiling point – composition diagram.
Glycol by wt. — 0% □ 75%
○ 50% △ 90%

increased with higher solvent concentration for the toluene-methyl*cyclo*hexane system with aniline as the solvent.

Fig. 2 shows the equilibrium data for the ethanol–water system plotted on glycol free basis with the concentration of glycol as a parameter.

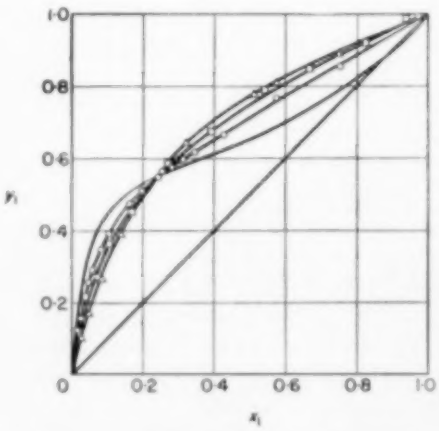

Fig. 2. Vapour liquid equilibrium diagram.
Glycol by wt. — 0% □ 75%
○ 50% △ 90%

Table 1. Vapour liquid equilibrium data of ethanol–water–ethylene glycol at atmosphere pressure

Temp. (°C)	X_s	Y_s	x_1	y_1	α
107·1	51·2	2·6	0·0	0·0	—
103·8	50·7	1·7	0·020	0·123	6·75
102·9	50·0	1·4	0·028	0·155	6·42
99·9	50·2	1·0	0·048	0·252	6·69
98·8	49·0	0·6	0·060	0·288	6·40
97·7	51·3	0·7	0·082	0·342	5·78
95·6	49·2	0·7	0·107	0·391	5·37
93·1	49·2	0·6	0·164	0·477	4·66
92·6	51·4	0·6	0·199	0·508	4·15
91·6	49·7	0·6	0·241	0·547	3·81
91·6	51·8	0·6	0·256	0·562	3·74
91·2	51·9	0·6	0·282	0·576	3·47
90·9	52·0	0·6	0·316	0·599	3·24
90·4	50·7	0·6	0·344	0·616	3·05
90·3	52·5	0·6	0·427	0·662	2·63
89·7	51·5	0·6	0·574	0·765	2·41
89·5	50·8	0·8	0·755	0·855	1·91
89·5	50·5	0·9	0·975	0·994	4·24
118·0	75·5	6·4	0·0	0·0	—
114·9	74·3	6·3	0·020	0·115	6·40
112·0	73·8	5·1	0·040	0·212	6·40
110·7	73·9	4·0	0·068	0·270	5·06
108·5	73·6	3·5	0·104	0·361	4·90
108·2	75·8	2·9	0·169	0·448	4·00
104·4	74·0	2·7	0·271	0·585	3·79
103·4	74·8	2·4	0·392	0·675	3·22
102·4	74·6	2·2	0·540	0·784	3·10
102·2	74·7	2·2	0·667	0·845	2·72
101·9	73·8	2·1	0·823	0·919	2·44
101·8	73·7	2·0	0·939	0·991	7·15
136·3	89·5	20·0	0·0	0·0	—
134·0	89·0	17·6	0·027	0·102	4·10
133·4	88·2	14·8	0·047	0·166	4·06
131·3	87·8	12·0	0·089	0·273	3·83
128·4	88·3	10·7	0·139	0·388	3·93
125·7	88·1	8·2	0·321	0·640	3·77
123·7	88·7	6·3	0·513	0·778	3·32
123·5	87·1	7·0	0·575	0·804	3·04
121·7	88·4	5·7	0·750	0·889	2·67
120·8	87·7	6·3	0·975	0·990	2·54

It can be observed that the effect of solvent is to make the system behave more ideally. The azeotrope of alcohol and water is broken even by the presence of 50 per cent glycol in the solution.

The relative volatility values of alcohol based on a solvent free basis as defined by the following equation

$$\alpha = \frac{y_1/(1-y_1)}{x_1/(1-x_1)}$$

were determined. Fig. 3 shows the relative volatility of alcohol with respect to water plotted against the concentration of ethyl alcohol in the liquid for different solvent concentrations as parameter. It may be observed that the relative volatility is enhanced by glycol above a critical concentration of ethanol viz. about 24 mole % on a glycol free basis, which is common for all the three concentrations of glycol studied and is depressed below this critical value of alcohol.

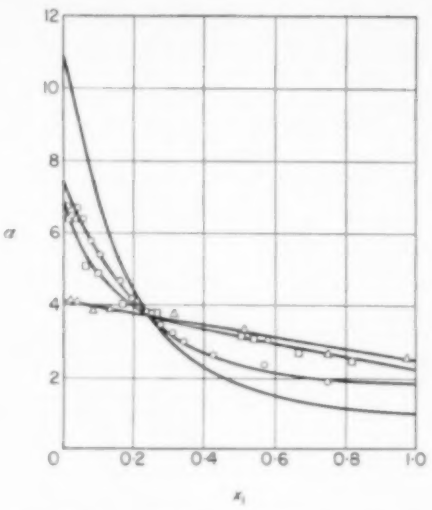

Fig. 3. Relative volatility – composition diagram. Glycol by wt. — 0% □ 75% ○ 50% △ 90%

Notation

α = relative volatility of alcohol to water based on mole fraction on glycol free basis

x_1 = mole fraction of alcohol in the liquid on a glycol free basis

X_s = weight per cent of glycol in the liquid

y_1 = mole fraction of alcohol in the vapour on a glycol free basis

Y_s = weight per cent of glycol in the vapour

T = boiling point °C

References

[1] Young S. *Distillation Principles and Processes*. p. 194. Macmillan, London 1922.

[2] Fritzweiler and Dietrich *Angew. Chem.* 1932 **45** 605.

[3] Wentworth T.O., Othmer D. F. and Pohler G. M. Trans. *Amer. Inst. Chem. Engrs.* 1943 **39** 565.

[4] Mariller C. *Bull. Assoc. Chim.* 1936 **53** 356–9.

[5] Cederquist K. N. *The Production and Use of Power Alcohol in Asia and Far East*. p. 206. U.N.O. 1952.

[6] Othmer D. F., Ten Eyck and Stolin S. *Industr. Engng. Chem.* (*Industr.*) 1951 **43** 1607.

[7] Curme G. O. and Johnston F. *Glycols*. Reinhold, New York 1952.

[8] Fenske M. R., Carlson C. S. and Quiggle D. *Industr. Engng. Chem.* (*Industr.*) 1947 **39** 1322.

Alagappa Chettiar College of Technology,
University of Madras,
India.

M. Ramanujam
G. S. Laddha

Notes on the diffusion-type model for longitudinal mixing in flow

(Concerning papers by O. Levenspiel, W. K. Smith, E. Van der Laan and R. Aris)

Aris has recently written a letter [1] increasing the value of Van der Laan's extension [2] of the methods used by Levenspiel and Smith [3] to determine dispersion coefficients for longitudinal mixing. In it, he showed that the impossible experimental task of injecting a perfect delta function of tracer into the flowing system is unnecessary if the tracer concentration is measured at two points in the system. As Aris mentions, the differential equations to be solved are:

$$\left(\frac{\partial}{\partial \theta} + \frac{\partial}{\partial z} - \frac{1}{\mathrm{Pe}}\frac{\partial^2}{\partial z^2}\right) R = 0 \qquad 0 \leqslant z \leqslant z_1 \tag{1b}$$

$$\left(\frac{\partial}{\partial \theta} + \frac{\partial}{\partial z} - \frac{1}{\mathrm{Pe}_b}\frac{\partial^2}{\partial z^2}\right) R_b = 0 \qquad z \geqslant z_1 \tag{1c}$$

$$R_b(+\infty) = \text{finite} \tag{3b}$$

$$R(z_1^-) = R_b(z_1^+) \tag{3f}$$

$$R(z_1^-) - \frac{1}{\mathrm{Pe}}\frac{dR(z_1^-)}{dz} = R_b(z_1^+) - \frac{1}{\mathrm{Pe}_b}\frac{dR_b(z_1^+)}{dz^-} \tag{3d}$$

$$R(z_0) = R_0 = \text{concentration measured at } z = z_0 \tag{3'}$$

Van der Laan's nomenclature and equation numbers are used except for (3').

The last boundary condition is due to the fact that measurements are now being taken at z_0 as well as at z_m, and the injection is at $z < z_0$. Upon checking the solution of these equations as given in Aris' letter, it was found that two errors existed: (a) a misprint of the first terms in the numerator and denominator which should have exponents $+(q - \frac{1}{2})\,\mathrm{Pe}\,\zeta$ and $+(q - \frac{1}{2})\,\mathrm{Pe}\,(\zeta + 1)$ respectively, and (b) a more serious error in the constant coefficients of the exponential terms ($(1 + q - q_b)$ and, $-(1 - q - q_b)$). The given solution is not consistent with the boundary conditions equations (3f) and (3d), as may be readily shown by differentiating $\bar{R}$ and $\bar{R}_b$ and substituting into (3f) and (3d).

The correct solutions are obtained by solving equation (1b), (1c), (3b), (3f), (3d) and (3') by the Laplace transformation, giving:

$$\bar{R} = \bar{R}_0 \left\{ \frac{(q - q_b)\exp[-(q + \frac{1}{2})\,\mathrm{Pe}\,(z_1 - z)] + (q + q_b)\exp[(q - \frac{1}{2})\,\mathrm{Pe}\,(z_1 - z)]}{(q - q_b)\exp[-(q + \frac{1}{2})\,\mathrm{Pe}\,(z_1 - z_0)] + (q + q_b)\exp[(q - \frac{1}{2})\,\mathrm{Pe}\,(z_1 - z_0)]} \right\} \qquad z_0 \leqslant z \leqslant z_1 \tag{a}$$

$$\bar{R}_b = \frac{2q\,\bar{R}_0 \exp[-(q_b - \frac{1}{2})\,\mathrm{Pe}_b\,(z - z_1)]}{(q - q_b)\exp[-(q + \frac{1}{2})\,\mathrm{Pe}\,(z_1 - z_0)] + (q + q_b)\exp[(q - \frac{1}{2})\,\mathrm{Pe}\,(z_1 - z_0)]} \qquad z \geqslant z_1 \tag{b}$$

These equations may be compared with those of Aris in order to see the differences. At the second measuring point z_m ($z_0 < z_m \leqslant z_1$), the solution is found by substituting $z = z_m$ into $\bar{R}$ (equation a).

$$\bar{R}_m = \bar{R}_0 \left\{ \frac{(q - q_b)\exp[-(q + \frac{1}{2})\,\mathrm{Pe}\,\zeta] + (q + q_b)\exp[(q - \frac{1}{2})\,\mathrm{Pe}\,\zeta]}{(q - q_b)\exp[-(q + \frac{1}{2})\,\mathrm{Pe}\,(\zeta + 1) + (q + q_b)\exp[(q - \frac{1}{2})\,\mathrm{Pe}\,(\zeta + 1)]} \right\} \tag{c}$$

where

$$\zeta = z_1 - z_m \qquad (\zeta + 1) = z_1 - z_0$$

The following procedure will be used to find the first and second moments of $\bar{R}_m$. As noted by Aris, if the above expression is expanded in a Maclaurin series, the coefficients of p^n in the expansion are

$$\frac{(-1)^n}{n!} \times (n\text{th moment about the origin}).$$

If σ^2 is defined as the second moment about the mean, μ, then the second moment about the origin is $(\sigma^2 + \mu^2)$ [4]. Therefore, the following expansions can be made:

$$\bar{R}_0 = 1 - \mu_0\,p + \tfrac{1}{2}(\sigma_0^2 + \mu_0^2)\,p^2 + \ldots \tag{d}$$

$$\bar{R}_m = 1 - \mu_m\,p + \tfrac{1}{2}(\sigma_m^2 + \mu_m^2)\,p^2 + \ldots \tag{e}$$

The expression in the braces in the formula for $\bar{R}_m$ may be written as:

$$1 - \mu\,p + \tfrac{1}{2}(\sigma^2 + \mu^2)\,p^2 + \ldots \tag{f}$$

$$\mu = 1 - \mathrm{Pe}^{-1}(1 - \beta)[1 - \exp(-\mathrm{Pe})]\exp -\mathrm{Pe}\,\zeta \tag{g}$$

$$\sigma^2 = \frac{2}{\mathrm{Pe}} + \frac{1 - \beta}{\mathrm{Pe}^2}\{(1 - \beta)\exp(-2\,\mathrm{Pe}\,\zeta)[\exp(-2\,\mathrm{Pe}) - 1] + 4(1 + \beta)\exp(-\mathrm{Pe}\,\zeta)[\exp(-\mathrm{Pe}) - 1] + 4\,\mathrm{Pe}\exp(-\mathrm{Pe}\,\zeta)[(\zeta + 1)\exp(-\mathrm{Pe}) - \zeta]\} \tag{h}$$

Therefore the values of μ and σ^2 are different than those of ARIS due to the error in the constants as mentioned above. Then, as shown by ARIS:

$$\bar{R}_m = [1 - \mu_0 p + \tfrac{1}{2}(\sigma_0^2 + \mu_0^2) p^2 + \dots] \\ [1 - \mu p + \tfrac{1}{2}(\sigma^2 + \mu^2) p^2 + \dots]$$

$$= 1 - (\mu_0 + \mu) p + \tfrac{1}{2}(\sigma_0^2 + \sigma^2 + \overline{\mu_0 + \mu^2}) p^2 + \dots \quad \text{(i)}$$

$$\mu = \mu_m - \mu_0 \quad \text{(j)}$$

$$\sigma^2 = \sigma_m^2 - \sigma_0^2 \quad \text{(k)}$$

where μ and σ^2 are given by (g) and (h).

These values of μ and σ^2 should check with those of VAN DER LAAN for the special case of a perfect delta function input. To show that this is true for my solution, the following nomenclature will be used:

at $x = x_i < x_0$, a perfect delta function is injected;
at $x = x_0 < x_m$, the concentration is measured and has mean μ_0 and variance σ^2;
at $x = x_m$, the concentration is measured and has mean μ_m and variance σ_m^2,
where x = distance from entrance of finite tube (VAN DER LAAN).

Since the various dimensionless variables in VAN DER LAAN's nomenclature involve the distance between injection and measurement, comparing the solutions for two different measurement points involves reverting to absolute (dimensional) variables.

For variables based on a length

$$l_j \text{ i.e. } \mathrm{Pe}_j = u\, l_j/D,\ z_j = x/l_j,\ \vartheta_j = u\theta/l_j,$$

the absolute mean and variance are related to the dimensionless ones by

$$\mu_a = \left(\frac{l_j}{u}\right) \mu_j \qquad \sigma_a^2 = \left(\frac{l_j}{u}\right)^2 \sigma_j^2 \quad \text{(l)}$$

Treating the means first:

$$\mu_a = \left(\frac{x_m - x_0}{u}\right) \mu \qquad \mu_{0a} = \left(\frac{x_0 - x_i}{u}\right) \mu_0 \times$$

$$\mu_{ma} = \left(\frac{x_m - x_i}{u}\right) \mu_m \quad \text{(m)}$$

$$\therefore \mu_a = \frac{x_m - x_0}{u} - \frac{D}{u^2}(1 - \beta)\{\exp[(u/D)(x_1 - x_m)] - \exp[-(u/D)(x_1 - x_0)]\} \quad \text{(n)}$$

From VAN DER LAAN's Table I:

$$\mu_{0a} = \frac{x_0 - x_i}{u} + \frac{D}{u^2}\{2 - (1 - \alpha)\{\exp[-(u/D)(x_1 - x_m)] - \exp[(u/D)(x_1 - x_0)]\} \quad \text{(o)}$$

$$\mu_{ma} = \frac{x_m - x_i}{u} + \frac{D}{u^2}\{2 - (1 - \alpha)\exp[-(u/D)x_i] - (1 - \beta)\exp[-(u/D)(x_1 - x_m)]\} \quad \text{(p)}$$

Therefore, $\mu_a = \mu_{ma} - \mu_{0a}$, as predicted by equation (j). Similarly, the variance, equation (k), may be proven to be correct.

Further extensions of these methods are forthcoming.

K. B. BISCHOFF

Illinois Institute of Technology,
Chicago, Illinois.

REFERENCES

[1] ARIS R. *Chem. Engng. Sci.* 1959 **9** 266.

[2] VAN DER LAAN E. T. *Chem. Engng. Sci.* 1958 **7** 187.

[3] LEVENSPIEL O. and SMITH, W. K. *Chem. Engng. Sci.* 1957 **6** 227.

[4] HOEL P. *Introduction to Mathematical Statistics* (2nd Ed.) p. 61. John Wiley, New York 1954.

Book Reviews

The Structure and Properties of Porous Materials. Edited by D. H. Everett and F. S. Stone. Butterworths, London 1958 and Academic Press, New York 1958. xiv + 389 pp. 60s., $12.00.

The present state of knowledge on surface area of porous masses forms one of the main groups of subjects discussed at the 10th Meeting of the Colston Research Society of Bristol, England, and the book under review contains the proceedings of this symposium. This was a gathering of 80 surface chemists and thermodynamicists from eleven countries who deliberated on eighteen papers, the discussion taking up almost half the book and containing much original research work apart from the contents of the papers. The structure and particularly the surface characteristics of crystals, gels and carbons, and the relevant properties of models of porous systems figure very largely as substance or background to most of the papers even when the swelling properties of wool and nylon or the weathering properties of building stone are discussed. Only few papers contain direct application to reaction kinetics of flow systems or to drying; one entitled *Porous structure of paper* deals with filtration, and another entitled *The influence of surface charges* deals with ion exchange. The major contributions both in substance of the papers and in the discussion came from Professor R. M. Barrer, Imperial College, London; Professor J. H. de Boer, Technical University, Delft; Professor J. R. Dacey, Royal Military College, Kingston, Ontario; Professor D. H. Everett, University of Bristol; Dr. B. Imelik, Sorbonne, Paris; Professor A. V. Kiselev, University of Moscow and Professor W. F. K. Wynne-Jones, King's College, Newcastle upon Tyne.

Relief from the bewildering abstractions of hopping, sliding and sorbed molecules, of ink bottle pores and molecular sieves is provided by a most fitting and inspiring final paper by Professor Preston, Leeds University, on some properties of living matter, viz. the movement of sap and carbohydrates in large trees.

P. Eisenklam

J. S. Rowlinson: **Liquids and Liquid Mixtures.** Butterworths, London 1959. 360 pp. 75s.

The title of this book is somewhat misleading as it deals only with equilibrium properties. The systems considered are generally simple condensed gases and organic liquids. Metals, electrolytes and polymers are not discussed. The subject matter can be roughly divided into three main themes, thermodynamics, statistical mechanics and experimental methods and results.

The first main section deals with thermodynamic properties and the critical state of pure liquids. Together with relevant thermodynamics, vapour pressure, thermal expansion, isothermal compressibility, thermal pressure, adiabatic properties, heat capacity and residual and configurational properties are discussed. Throughout, close contact with experiment is maintained, not in the form of detailed descriptions of apparatus, but rather in the mention of important points for the experimentalist. Useful tables of the thermodynamic properties of a number of the simpler liquids are given.

In the following two chapters on the properties of simple and complex liquids at low pressures the basic thermodynamics of ideal, non-ideal and partially miscible liquids is treated. The experimental data for approximately one hundred binary systems are discussed ranging from mixtures of simple condensed gases to aqueous mixtures. The thermodynamic treatment of consolute temperatures which is based on a Taylor expansion of the free energy about its value at the critical point is similar to that used for discussing critical phenomena in pure liquids. Testing of thermodynamic data for consistency is stressed.

The properties of liquid mixtures at high pressures is treated under azeotropy, latent heats of binary mixtures and critical phenomena in mixtures of simple and complex liquids. Much of the older work in this field is usefully summarized here.

The last main section dealing with intermolecular forces and the statistical mechanics of fluids and their mixtures can be read independently of the previous chapters. It provides an up-to-date account of the various attempts which are being made to calculate the equilibrium properties of liquids. A not unwelcome note of realism can be detected by the reviewer in this section when the author, facing realities, holds out that the modified cell theories provide more immediate hope for progress than the distribution function approach which is still anchored to the superposition approximation. The book is well produced, liberally illustrated and has an extensive bibliography. However the use of lower case letters, inconsistently applied to the titles of journals listed in the references, is in opposition to the currently accepted format and has nothing to recommend it. The number of printing errors is a minimum.

As a source of information on the experimental equilibrium properties of liquids and liquid mixtures and an up-to-date account of the associated thermodynamic and molecular aspects of the subject, this book can be confidently recommended to engineers. The price is unfortunately rather on the high side.

E. McLaughlin

Isotopentechnik in Amerika. Herausgegeben vom Rationalisierungs-Kuratorium der Deutschen Wirtschaft. Auslandsdienst, Helft 84. Carl Hanser Verlag, München 1959. 131 S. 17 DM.

Dem Bericht liegt eine Reise von Vertretern der Wissenschaft und Wirtschaft, der Behörden und Gewerkschaften Berlins zu Grunde, in deren Verlauf Ende 1956 in den USA mehr als 20 Unternehmen und Institute besucht wurden, die sich mit Isotopen- und Kernenergietechnik befassen.

An allgemeinen Problemen werden die Herstellung radioaktiver Isotope, Fragen der Laboreinrichtung, Sicherheitsvorschriften und Massnahmen, der Transport und die Abfallbeseitigung besprochen. Anschliessend werden – unterstützt von Abbildungen und Literaturhinweisen – Anwendungen von Isotopen in den verschiedenen Zweigen der Industrie und Strahlungsmessgeräte beschrieben und in aller Kürze einige Einblicke in die Reaktortechnik gegeben. Ein besonderer Abschnitt ist der wirtschaftlichen Bedeutung der Kerntechnik gewidmet.

Ohne sich in technische oder physikalische Einzelheiten zu verlieren, gibt das leicht lesbare Heft einen Eindruck von dem Stand der Entwicklung und ermöglicht einen Überlick über die Bedeutung, die Probleme und die Anwendungsmöglichkeiten der Isotopen- und Kernenergietechnik.

G. Heyl

Grundlagen der Chemischen Technik (Herausgeber, H. Mohler und O. Fuchs) Band II.—O. Fuchs: **Physikalische Chemie als Einführung in die chemische Technik.** Verlag Sauerländer, Aarau und Frankfurt (Main) 1959. 496S. 37 DM.

Der zweite Band der Buchreihe *Grundlagen der Chemischen Technik* mit einem der Herausgeber als Autor behandelt diejenigen Kapitel der physikalischen Chemie, welche häufig als Grundlagen in der chemischen Technik gebraucht werden. Er tut dies in der richtigen Erkenntnis, dass insbesondere der Verfahrenstechniker in den physikalischen Grundvorgängen heimisch sein muss. Das Buch erhebt nicht den Anspruch, ein Lehrbuck oder Nachschlagewerk für physikalische Chemie zu sein, zeigt aber im Gegensatz zu diesen klassischen Werken in einer Reihe von praktischen Beispielen, in welcher Weise die Kenntnis der physikalisch-chemischen Grundbegriffe unentbehrlich ist und wie die diesbezüglichen Daten praktisch mithelfen, technische Werte zu bestimmen und damit tiefer in die Vorgänge, wie sie sich in industriellen Prozessen volziehen, einzudringen.

Bei der Fülle des zu behandelnden Stoffes war es ohne Zweifel schwierig, die Grenzen für das Wesentliche zu ziehen, und einige Unterkapitel wie z.B. Explosionsgrenzen oder gewisse technische Abschnitte im Kapitel Phasengrenzflächen mussten reichlich kurz gefasst werden.

Das Buch enthält erstaunlich viel Material sowohl für Studierende in Verfahrenstechnik und chemischer Technologie wie auch für Chemiker und Ingenieure, welche in der Praxis stehen und in nicht zu langer Zeit ihr theoretisches Wissen wieder auffrischen und ergänzen wollen. Das Werk enthält viele persönliche Erfahrungen des Autors; die Art der Darstellung und der gewählte Stil machen das Studium des Buches recht leicht.

Dem Verlag Sauerländer gebührt Anerkennung für die gute Ausführung des Buches bei mässigem Preis.

A. Guyer

Clyde Orr Jr. and J. M. Dallavalle: **Fine Particle Measurement.** Macmillan, New York, 1959. xiv + 353 pp. £3 13s. 6d.

The late Professor Dallavalle has been a pioneer in a field which has now come to be known as Powder Technology and his well-known book *Micromeritics* remained a guide on the behaviour and characteristics of small particles since its first edition appeared sixteen years ago. He and his co-worker at the Georgia Institute of Technology in Atlanta have now enlarged the section on particle measurement and deal with Size, Surface and Pore Volume.

The book consists of a collection of numerous methods which have been used or suggested, ranging from microscopy and sieving to techniques making use of radiation scattering and transmission. No definition of "fine particles" is given apart from the statement that half the universe consists of them, and the electron microscope (lower limit 0·001 μ) and adsorption methods are treated together with sieving methods so that the size ratio under consideration is of the order of $1 : 10^7$. No wonder that within 300 odd pages only a catalogue of methods could be given with little attention to the relative importance or merits of each. Thus we find that elutriation is dismissed in 500 words, capillary pressure methods of surface determination in half this amount, statistical methods are not mentioned at all, and some methods are treated only in the from of cursory summaries.

The great virtue of the presentation lies in the bringing together of a mass of information and treating it up to a level which is fully adequate for a general understanding of the principles and an appreciation of the use of each method. Some 700 references are provided as sources of detailed information. Although, in general, these are adequate, one misses some people well known on this side of the Atlantic, foremost being Dr. H. Heywood, an authority on size measurement of small particles since the early thirties. There is evidently great uncertainty regarding the accuracy of interpretations of measurements particularly of surface area because of the lack of precise definitions, and hence the collection of typical results and comparison measurements in the appendix to the book is valuable.

P. Eisenklam

Trockungstechnik (Herausgeber O. Krischer und K. Kröll). Band II.—**Trockner und Trockuungsverfahren** (K. Kröll). Springer-Verlag, Berlin 1959. 588p. 69.00 DM.

Der zweite Band der *Trocknungstechnik* behandelt die technischen Verfahren und Apparate zur Trocknung bestimmter Güter unter Berücksichtigung der im ersten Band beschriebenen wissenschaftlichen Grundlagen des Trocknungsvorganges.

Der umfangreiche Stoff, nach dem Gesichtspunkt gleicher physikalischer Gesetzmässigkeit gegliedert, wird dem Leser in übersichtlicher Weise geboten. Dabei wird jede Trocknerbauart sowohl aus der mechanischen, thermischen und aerodynamischen Wirkungsweise des Trockners als auch aus den technologischen Eigenschaften des darin behandelten Gutes heraus verständlich gemacht.

Das Buch zeigt am Anfang, wie man Trockner planen und entwerfen kann, und gibt Hinweise für die Umrechnung von Versuchsergebnissen auf andere Temperaturen, relative Feuchten, Schichtdicken usw. Ein weiteres Kapitel ist dem Wärmebedarf des Trockners und der Frage der Wärmerückgewinnung gewidmet. Im Abschnitt "Fördern und Führen der Luft" wird durch zahlreiche, anschauliche Strömungsaufnahmen am Wasserkanal-Modell die strömungsgerechte Gestaltung von Trocknern gezeigt. Ein umfangreiches Kapitel über Konvektionstrockner behandelt die verschiedenen Möglichkeiten der Um – bzw. Durchströmung des Gutes und beschreibt neben einer Vielzahl spezieller Bauformen auch die Trocknung bestimmter Güter, so z.B. die Holz-, Leder-, Lack-, Textil-, Getreide-, Lebensmittel- und Futtermitteltrocknung. Die Verfahren der Strahlungstrocknung und der Trocknung im elektrischen Wechselfeld werden ausführlich nach physikalischer Wirkungsweise und technischer Ausführungsform diskutiert. Das Buch befasst sich ferner mit der Technik der Kontakttrocknung und der Vakuumtrocknung einschliesslich der Gefriertrocknung. Ein besonderes Kapitel zeigt Möglichkeiten zur Luftentfeuchtung und zur Wiedergewinnung von Lösungsmitteln, die beim Trocknungsvorgang aus dem Gut verdunsten.

Das Werk gibt, zusammen mit dem ersten Band, einen umfassenden Überblick über alle mit der Trocknung zusammenhängenden Fragen und bietet sowohl dem Hersteller als auch dem Anwender von Trocknungsanlagen wertvolle Arbeitsunterlagen.

Das ausführliche Inhalts- und Sachverzeichnis und die Schrifttumsangaben am Schluss jeden Kapitels tragen zur Übersichtlichkeit des Buches wesentlich bei, das wegen der leicht verständlichen Fassung auch dem Studierenden sehr empfohlen werden kann.

H. Kunze

SELECTION OF CURRENT PAPERS OF INTEREST TO CHEMICAL ENGINEERS

W. M. Jones and P. J. Isaac : The flow of carbon dioxide and nitrogen at high pressures through porous plugs of lampblack. *Trans. Faraday Soc.* 1959 **55** 1947–1958.

G. I. Taylor : The dynamics of thin sheets of fluids—I. Water bells (shape produced by obstruction in a jet). II. Waves on fluid sheets. III. Disintegration of fluid sheets. *Proc. Roy. Soc.* 1959 A**253** 289–321.

G. A. Gilbert and R. C. Ll. Jenkins : Sedimentation and electrophoresis of interacting substances—II. Asymptotic boundary shape for two substances reacting irreversibly. *Proc. Roy. Soc.* 1959 A**253** 420–437 (See also G. A. Gilbert : *Proc. Roy. Soc.* 1959 A**250** 377–388.

Lu Ting : On the mixing of two parallel streams. *J. Math. Phys.* 1959 **38** 153–165.

S. W. Yuan : Turbulent flow in channels with porous walls. *J. Math. Phys.* 1959 **38** 166–171.

G. D. Gordon : Mechanism of speed and break-up of drops (in an air stream). *J. Appl. Phys.* 1959 **30** 1759–1761.

I. S. Bjorklund and W. M. Kays : Heat transfer between concentric rotating cylinders. *J. Heat Transfer* (*Trans. Amer. Soc. Mech. Engrs.* Series C) 1959 **81** 175–186.

J. E. Lay : An experimental and analytical study of vortex flow temperature separation by superposition of spiral and axial flows (Parts 1 and 2). *J. Heat Transfer* (*Trans. Amer. Soc. Mech. Engrs.* Series C) 1959 **81** 202–222.

E. M. Sparrow and J. L. Gregg : Heat transfer from a rotating disk to fluids of any Prandtl number. *J. Heat Transfer* (*Trans. Amer. Soc. Mech. Engrs.* Series C) 1959 **81** 249–251.

V. S. Arpaci and J. A. Clark : Dynamic response of heat exchangers having internal heat sources—III. *J. Heat Transfer* (*Trans. Amer. Soc. Mech. Engrs.* Series C) 1959 **81** 253–266 (See also *Trans. Amer. Soc. Mech. Engrs.* 1958 **80** 612–624, *Ibid.* 1958 **80** 625–634).

H. Wolf : Heating and cooling air and carbon dioxide in the thermal entrance region of a circular duct with large gas to wall temperature differences. *J. Heat Transfer* (*Trans. Amer. Soc. Mech. Engrs.* Series C) 1959 **81** 267–279.

R. Siegel and E. M. Sparrow : Turbulent flow in a circular tube with arbitrary internal heat sources and wall heat transfer. *J. Heat Transfer* (*Trans. Amer. Soc. Mech. Engrs.* Series C) 1959 **81** 280–290.

E. M. Sparrow and J. L. Gregg : Laminar condensation heat transfer on a horizontal cylinder. *J. Heat Transfer* (*Trans. Amer. Soc. Mech. Engrs.* Series C) 1959 **81** 291–296.

E. L. Lustenader, R. Richter and F. J. Neugebauer : The use of thin films for increasing evaporation and condensation rates in process equipment. *J. Heat Transfer* (*Trans. Amer. Soc. Mech. Engrs.* Series C) 1959 **81** 297–307.

R. L. Chambers and E. V. Somers : Radiation fin efficiency for one-dimensional heat flow in a circular fin. *J. Heat Transfer* (*Trans. Amer. Soc. Mech. Engrs.* Series C) 1959 **81** 327–329.

SELECTION OF CURRENT SOVIET PAPERS OF INTEREST TO CHEMICAL ENGINEERS*

E. K. Sirde and P. G. Romankov: Investigation into the process of steam distillation. *Zh. prikl. Khim.* 1959 **32** 2197–2207.

S. N. Ganz, S. B. Leibovich, N. A. Malishevich and M. A. Lokshin: Investigation of the rate of absorption of carbon dioxide by monoethanolamine in a horizontal mechanical absorber. *Zh. prikl. Khim.* 1959 **32** 2207–2210.

A. A. Noskov, G. V. Burova and P. Feldesh: Plate efficiency of a single sieve plate in rectification. *Zh. prikl. Khim.* 1959 **32** 2211–2218.

V. B. Sarkits, D. T. Traber and I. P. Mukhlenov: Heat transfer from a suspended catalyst bed to a heat transfer surface. *Zh. prikl. Khim.* 1959 **32** 2218–2225.

B. M. Bogoslavski, B. M. Yavorski and A. D. Virnik: On application of thermal diffusion to purification of dyestuffs. *Z. prikl. Khim.* 1959 **32** 2225–2229.

M. V. Poltakov, V. V. Shalya and Z. Z. Visotski: Investigation of catalytic conversion of methanol into formaldehyde in a fluidized catalyst bed. *Zh. prikl. Khim.* 1959 **32** 2275–2283.

D. P. Dobichin: Diffusion of water vapour and flow of air in porous glass. *Zh. prikl. Khim.* 1959 **32** 2336–2339.

P. A. Rebinder: Surface-active substances and their application. *Khim. Nauka i Prom.* 1959 **4** 554–565.

A. B. Taubman: Physico-chemical principles of wetting and of detergent action of surface-active substances. *Khim. Nauka i Prom.* 1959 **4** 566–573.

A. D. Petrov and G. I. Nikishin: Methods of synthesis of surface-active substances. *Khim. Nauka i Prom.* 1959 **4** 573–585.

F. V. Nevolin: Synthetic detergents and their compositions. *Khim. Nauka i Prom.* 1959 **4** 586–592.

R. A. Palina: Surface-active substances on ethylene-oxide basis. *Khim. Nauka i Prom.* 1959 **4** 592–598.

A. K. Livshits: Flotation reagents in current use, their production and application. *Khim. Nauka i Prom.* 1959 **4** 622–628.

M. M. Egorov, V. F. Kiselev and K. G. Krasilnikov: Adsorption capacity of unit surface of quartz. *Zh. fiz. Khim.* 1959 **33** 2141–2144.

M. G. Kaganer: New method of determination of specific surface area of adsorbents and other finely-dispersed substances. *Zh. fiz. Khim.* 1959 **33** 2202–2210.

B. V. Deryaguin, S. S. Dukhin and V. A. Lisichenko: Kinetics of attachment of bubbles to mineral particles during flotation. *Zh. fiz. Khim.* 1959 **33** 2280–2287.

G. A. Akselrod: Theory of diffusional extraction of substances from porous bodies—I. Equations of extraction kinetics. *Zh. fiz. Khim.* 1959 **33** 2316–2324.

M. M. Dubinin and E. G. Zhukovskaya: On adsorption properties of carbon adsorbents. Study of adsorption properties of active charcoals with developed transitional porosity. *Izv. Akad. Nauk SSSR, Otd. khim. Nauk* 1959 (10) 1705–1715.

E. I. Yantovski: Estimation of influence of free convection on turbulent flow. *Zh. tekh. Fiz.* 1959 **29** 1390–1392.

G. D. Rosenberg: Experimental investigation of unsteady flow of viscoplastic fluids. *Dokl Akad. Nauk SSSR* 1959 **129** 56–58.

*To assist readers, translations of any article appearing in the above list can be obtained at a reasonable charge. All orders should be addressed to the Administrative Secretary of the Pergamon Institute at either Headington Hill Hall, Oxford or 122 East 55th Street, New York 22 whichever is more convenient.

V. F. Kazantsev: Motion of air bubbles in water under the action of Bjerknes forces in acoustic fields. *Dokl. Akad. Nauk SSSR* 1959 **129** 64–67.

V. Yu Orlov and N. M. Zhavoronkov: Effect of ultrasound on the absorption of carbon dioxide by water. *Dokl. Akad. Nauk SSSR* 1959 **129** 161–164.

D. P. Timofeev and I. T. Erashko: Investigation of the structure of sorbents by kinetic methods. *Dokl. Akad. Nauk SSSR* 1959 **129** 384–386.

B. L. Kutman: Effect of speed of rotation and of shape of armour on performance of a drum-type ball mill. *Teploenergetika* 1959 **6** (11) 24–28.

U. F. Dityakin and L. N. Britneva: Generalization of measurements of drop sizes with the aid of dimensionless criteria in the case of atomization of liquids by a centrifugal atomizer. *Teploenergetika* 1959 **6** (11) 33–36.

N. V. Sokolov and V. P. Osokin: Abrasivity of coal and the resistance of metals to wear in milling. *Teploenergetika* 1959 **6** (11) 37–41.

M. P. Vukolovich and V. V. Altunin: Experimental investigation into the P–V–T relationship of carbon dioxide. *Teploenergetika* 1959 **6** (11) 58–65.

ERRATA

Selection of Current Soviet Papers of Interest to Chemical Engineers. *Chem. Engng. Sci.* 1959 **11** 222.

The last reference on p. 223 should read: S. S. Kutateladze and V. N. Moskvicheva: On the relation between the hydrodynamics of a two-component layer and the theory of crisis in the mechanism of boiling. *Zh. tekh. Fiz.* 1959 **29** 1135–1139.

The first two references on p. 224 should read: P. N. Kubanski: On the coagulation of aerosols by free streams of gas. *Zh. tekh. Fiz.* 1959 **29** 1140–1141. V. V. Rachinskaya: On the problem of hydrodynamic properties of ion-exchange resins. *Zh. tekh. Fiz.* 1959 **29** 1159–1161.